EUSKAL HERRIKO UNIBERTSITATEA – UNIVERSIDAD DEL PAIS VASCO

POLIMERO ETA MATERIAL AURRERATUAKEN SAILA: FISIKA, KIMIKA ETA TEKNOLOGIA –

DEPARTAMENTO DE POLÍMEROS Y MATERIALES AVANZADOS: FÍSICA, QUÍMICA Y TECNOLOGÍA

Substrate-enhanced and subsurface infrared near-field spectroscopy of organic layers

Lars Mester

- PhD Thesis -

Thesis supervisor

Prof. Rainer Hillenbrand

2020

This PhD thesis has been carried out

by

Lars Mester

at

CIC nanoGUNE, San Sebastián, Spain

under the supervision of

Prof. Rainer Hillenbrand

Contents

1 Summary

Infrared spectroscopy is a powerful tool for materials characterization that is used in many fields of science and technology. However, the analysis of nanoscale structures using conventional infrared techniques is severely limited, as the spatial resolution is limited by diffraction to a few micrometers. One solution that combines infrared spectroscopy with nanoscale spatial resolution is scattering-type scanning near-field optical microscopy (s-SNOM)[1–3]. In s-SNOM, monochromatic electromagnetic radiation of the visible[4–6], infrared[5–7] or terahertz[6,8,9] spectral range is focused onto the tip of a standard, metallized atomic force microscopy (AFM) probe as illustrated in Figure 1.1a. The tip – acting as an optical antenna – concentrates the radiation into highly confined and enhanced near fields at the very tip apex[2,10,11] (Figure 1.1b). The near fields interact with the sample, which modifies the tip-scattered field in amplitude and phase, depending on the local optical sample properties. By recording the tip-scattered light as a function of tip position, nanoscale resolved images of the sample's optical properties are obtained.[1] The spatial resolution is determined by the extension of the near fields, which is independent of the illumination wavelength λ and in the order of the tip apex radius R, which is typically around R = 25 nm.[1,2,5] In order to suppress unwanted background signals, the AFM is operated in tapping mode, where the tip is oscillating normal to the sample surface at a frequency Ω. Due to the near-field interaction being strongly nonlinearly dependent on the tip-sample distance, this operation mode yields higher harmonic modulation of the tip-scattered field, but not of the background scattering. Recording the detector signal at higher harmonic frequencies $n\Omega$ (typically $n > 2$) thus yields the pure near-field signal.[12,13]

At infrared (IR) frequencies, s-SNOM offers the possibility for highly sensitive compositional mapping based on probing vibrational excitations such as the ones of molecules or phonons, analogously to infrared microscopy.[14] Utilizing a broadband infrared source and Fourier transform infrared spectroscopy (FTIR) of the light scattered by the s-SNOM tip even allows for recording nanoscale-resolved infrared spectra.[15] The technique – named nano-FTIR spectroscopy – yields near-field phase spectra that match well the absorptive properties of organic samples,[15–17] and thus allows for nanoscale chemical identification based on standard FTIR references.[18]

Importantly, the IR light that is nano-focussed below the tip does not only probe a nanometric (two-dimensional) area below the tip, but in fact probes a nanometric (three-dimensional) volume below the tip (Figure 1.1c)[19–22] – despite near-field microscopy being a surface-scanning technique. Although the capability of s-SNOM for probing subsurface materials is well-known,[19,23–27] only few systematic studies on the subject exist[20,21,28]. Particularly the potential capability for subsurface material analysis using nano-FTIR spectroscopy is largely unexplored terrain. In this thesis, infrared near-field spectroscopy (nano-FTIR) based on s-SNOM is used to analyse nanostructured samples, which consist of several thin layers within the nano-FTIR probing volume (analogous to Figure 1.1c).

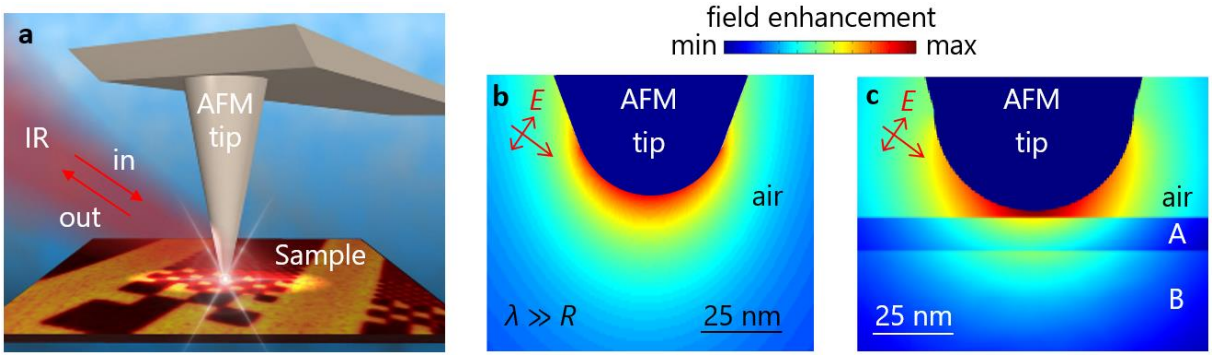

Figure 1.1: Working principle of s-SNOM and nano-FTIR. (a) A focused IR laser beam illuminates a metallized AFM tip which is near the surface of a sample. The tip-scattered light depends on the sample region which is located directly below the tip apex. (b) Simulated electric field distribution around an AFM tip with apex radius R = 25 nm under external illumination with the incident electric field E and illumination wavelength $\lambda \gg R$, showing that the tip acts as optical antenna that concentrates the incident electric field into a nanoscale-sized electromagnetic hotspot directly below the tip apex. Image taken from [29]. (c) Simulated electric field distribution around an AFM tip with apex radius R = 30 nm located above a 10 nm-thick layer "A" on a substrate "B", showing that the near fields of the hotspot penetrate into the sample, thus probing a three-dimensional volume of the sample. Image taken from [22].

This thesis is structured as follows:

In **chapter 2**, this summary is provided in Spanish language.

In **chapter 3**, s-SNOM and nano-FTIR are explained. First, an introduction to nanoscale-resolved infrared spectroscopy is given, followed by a description of the working principle of scattering-type SNOM and suppression of background-scattered light using tip height modulation and higher harmonic signal demodulation. An emphasis is put onto several mathematical models that describe the near-field interaction between the probing tip and the sample, and that allow for a description of spectral contrasts observed in s-SNOM and nano-FTIR experiments. Importantly, it is briefly discussed that the near-field interaction between tip and multilayer samples must be described using the *momentum-dependent* Fresnel reflection coefficient of the sample. Finally, a typical implementation of an experimental nano-FTIR setup based on AFM is explained by first introducing the working principle of a FTIR spectrometer, tapping-mode operation of an AFM and finally describing the employed nano-FTIR setup that allows for the detection of amplitude- and phase-resolved infrared spectra with nanoscale spatial resolution.

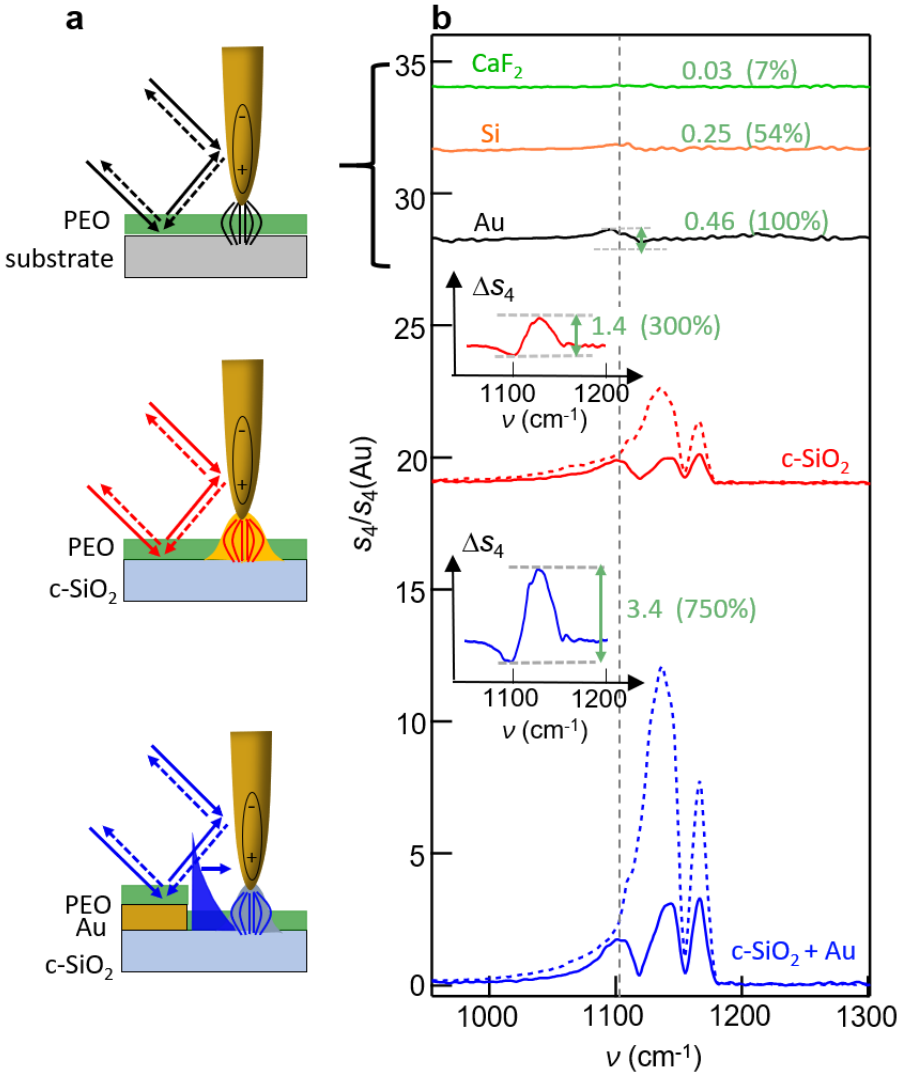

Figure 1.2: Comparison of different substrates for nano-FTIR spectroscopy of PEO. (a) Sketches of the different mechanisms contributing to the tip illumination in the performed experiments. From top to bottom: indirect illumination of the tip via the substrate (top), additional resonant tip-substrate coupling due to tip-induced phonon polariton excitation in the substrate (middle), and additional tip illumination via propagating surface phonon polaritons launched by the edge of a gold film (bottom). (b) From top to bottom: nano-FTIR amplitude spectra of PEO on CaF_2, Si, Au and quartz (c-SiO_2) substrates (solid curves). The very bottom spectrum was obtained in 1 µm distance to the edge of an extended Au film launching surface phonon polaritons. Dotted lines show spectra without PEO. For better visibility of the vibrational features, the spectra on the different substrates are offset. Insets: The red and blue curves show the calculated spectral contrast Δs_4 of PEO, i.e. the signal of the quartz substrate has been subtracted. Note that the scale of the vertical axes Δs_4 and s_4/s_4(Au) are the same. Figure taken from [30].

Chapter 4 addresses the challenge of detecting a molecular layer (here poly-ethylene oxide, PEO) that is thinner than the probing volume and that is placed on standard IR substrates such as CaF_2. As shown in Figure 1.2b (green curve), the nano-FTIR amplitude s_4 signal of such sample is rather weak. To improve the sensitivity of nano-FTIR to thin molecular layers, it is demonstrated that a significant signal enhancement is achieved by placing the molecular layer

on highly reflective substrates such as silicon or gold substrates (orange and black curves respectively). An even further signal enhancement is demonstrated by exploiting polariton-resonant tip-substrate coupling and surface polariton illumination of the probing tip. When the molecular vibration matches the tip-substrate resonance, a signal enhancement of up to nearly one order of magnitude is achieved on a phonon-polaritonic quartz (c-SiO_2) substrate (red and blue curves), as compared to nano-FTIR spectra obtained on metal (Au, black curve) substrates, and up to two orders of magnitude when compared to the standard infrared spectroscopy substrate CaF_2 (green curve). Insets in Figure 1.2b show the spectral contrast that is assigned to the PEO vibrational mode, i.e. after the signal from the quartz substrate has been subtracted. The signal enhancement is caused on the one hand by an increased near-field interaction between tip and sample (illustrated by curved lines and shaded area below the tip apex in Figure 1.2a), and on the other hand by efficient illumination of the probing tip and efficient detection of the tip-scattered light via reflection at the sample surface (solid and dashed arrows respectively). Furthermore, the tip is illuminated via propagating surface phonon-polaritons that are launched at the edge of a gold film (indicated by blue area in bottom illustration). The results will be of critical importance for boosting nano-FTIR spectroscopy toward the routine detection of monolayers and single molecules.

In **chapter 5**, nano-FTIR spectroscopy of subsurface organic layers is demonstrated (Figure 1.3a,b), revealing that nano-FTIR spectra from thin surface layers differ from that of subsurface layers of the same organic material. Particularly it is found that the peaks in nano-FTIR phase spectra of subsurface organic layers are spectrally red-shifted compared with nano-FTIR spectra of the corresponding bulk material, and that the red-shift is stronger than the one observed for surface layers when their thickness is reduced (Figure 1.3c). The experimental findings are confirmed and explained by a semi-analytical model for calculating nano-FTIR spectra of multi-layered organic samples, which also reveals that peak-shifts in nano-FTIR spectra of multilayer samples can be traced back to the sample's momentum-dependent quasi-electrostatic Fresnel reflection coefficient $\beta(\nu,q)$, provided that chemically induced peak-shifts can be excluded. Further, the correlation of various nano-FTIR peak characteristics is studied, in order to establish a simple and robust method for distinguishing surface from subsurface layers without the need of theoretical modelling or simulations (again, provided that chemically induced spectral modifications are not present). It is demonstrated that surface and subsurface layers can be differentiated by analysing the ratio of peak heights obtained at different higher harmonic demodulation orders n (Figure 1.3d, according to the developed peak height ratio criterium, data points in gray areas correspond to subsurface material). The results are critically important for the interpretation of nano-FTIR spectra of multilayer samples, particularly to avoid that geometry-induced spectral peak shifts are explained by chemical effects.

In summary, in this thesis the crucial role of highly reflecting substrates for enhancing the infrared nanospectroscopy signals of thin molecular layers is demonstrated. An even further enhancement could be achieved by implementing additional tip illumination, which includes indirect illumination of the tip via a highly reflecting metal surface and via propagating surface

polaritons, altogether boosting the nano-FTIR spectroscopy signal of molecular vibrations by nearly one order of magnitude compared to nano-FTIR employing Au substrates. Furthermore, this work reveals a direct relation between nano-FTIR spectra and the momentum-dependent quasi-electrostatic Fresnel reflection coefficient of multilayer samples, which facilitates the interpretation of nano-FTIR spectra of such samples, i.e. to distinguish peak-shifts caused by chemical effects from peak-shifts caused by geometrical effects. Finally, it is noted that the observed sample- and momentum determined peak-shifts are not an exotic feature of near-field spectroscopy, but also occur in far-field spectroscopy, where the probing momentum is determined by the angle of incidence. The results presented in chapters 4 and 5 were previously published in Refs. 30 and 22 respectively.

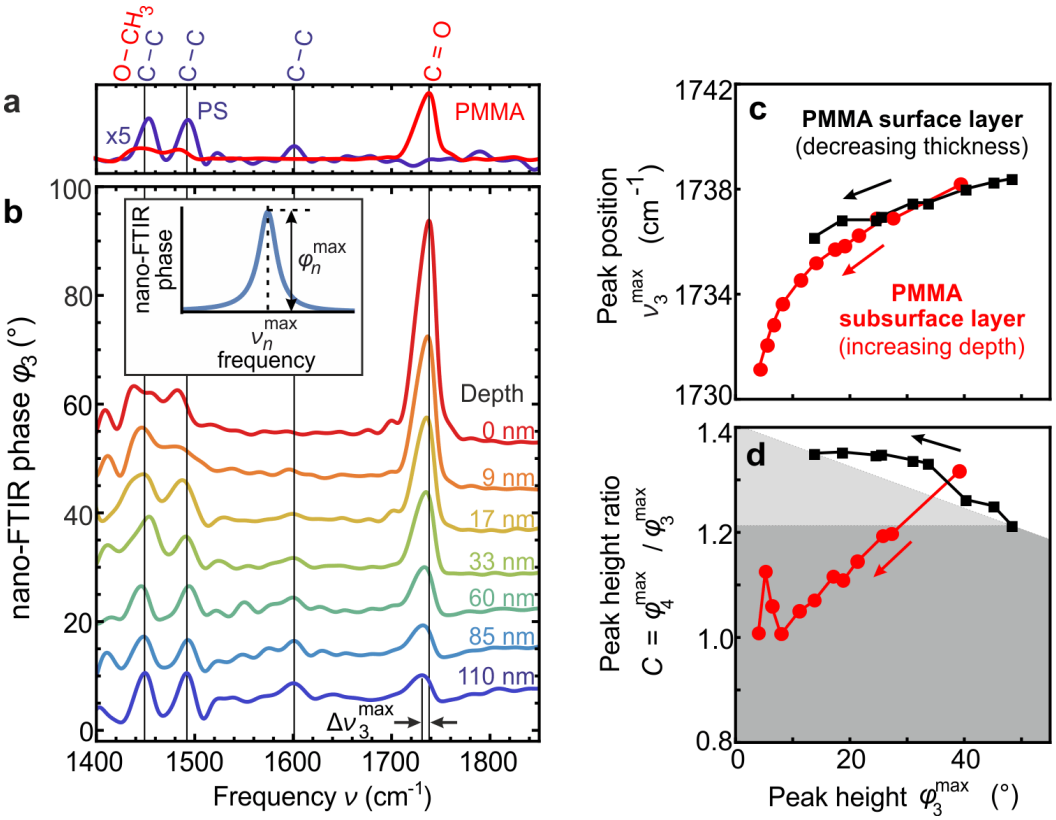

Figure 1.3: Subsurface nano-FTIR spectroscopy experiments on well-defined multilayer samples. (a) Reference nano-FTIR phase φ_3 spectra recorded on thick layers of polymethyl-methacrylate (PMMA) and polystyrene (PS). (b) Subsurface nano-FTIR phase spectra of PMMA at different depths below PS. Black arrows indicate a spectral shift $\Delta\nu_3^{max}$ of the peak corresponding to the C=O vibrational mode of PMMA. Inset: Definition of the spectral peak position ν_n^{max} and peak height φ_n^{max} for each demodulation order n. (c) Spectral peak positions ν_3^{max} and (d) peak height ratios $C = \varphi_4^{max}/\varphi_3^{max}$ of PMMA surface layers (black symbols) and PMMA subsurface layers (red symbols) are plotted versus the corresponding peak height φ_3^{max} (experimental data). Arrows indicate decreasing PMMA surface layer thickness (black) and increasing PMMA subsurface layer depth (red). Subsurface PMMA layer thickness is 59 nm. (d) Gray areas indicate the data spaces that correspond to subsurface materials. Figure adapted from [22].

2 Resumen

La espectroscopia en el infrarrojo es una potente herramienta que sirve para caracterizar materiales y es frecuentemente utilizada en diferentes campos de la ciencia y la tecnología. Sin embargo, debido a las limitaciones impuestas por la difracción, el análisis de estructuras a la nanoescala utilizando técnicas convencionales en el infrarrojo se encuentra limitada a unos cuantos micrómetros en la resolución espacial. Una solución para batir el límite de difracción, que combina tanto espectroscopia en el infrarrojo como resolución espacial a la nanoescala, la ofrece la técnica de microscopía óptica de barrido por dispersión de campo cercano[1–3] (s-SNOM por sus siglas en inglés). En s-SNOM, radiación electromagnética monocromada en el rango espectral del visible[4–6], infrarrojo[5–7] o los terahercios[6,8,9] es enfocada en una punta metálica típicamente utilizada en microscopía de fuerza atómica (AFM por sus siglas en inglés). La punta – que actúa como antena óptica – concentra la radiación en campos cercanos altamente confinados y aumentados en el ápice de la punta[2,10,11]. Asimismo, estos campos cercanos interactúan con la muestra y modifican la amplitud y la fase del campo dispersado por la punta en función de las propiedades locales ópticas de la muestra. Al recolectar la luz dispersada por la punta, en función de la posición de ésta, se pueden obtener imágenes de las propiedades ópticas de la muestra con resolución a la nanoescala[1]. Es importante mencionar que la resolución espacial de la técnica s-SNOM se encuentra determinada por la extensión de los campos cercanos (que es independiente de la longitud de onda λ de la iluminación) y del orden del radio R del ápice de la punta, siendo este último típicamente R = 25 nm.[1,2,5] Con la finalidad de suprimir las señales de fondo no deseadas, el AFM se opera en modo dinámico donde la punta oscila normal a la superficie de la muestra a frecuencia Ω. Debido a que las interacciones del campo cercano dependen en gran medida, de forma no lineal, de la distancia entre la punta y la muestra, este modo de operación (el modo dinámico) produce modulaciones armónicas de orden alto en el campo dispersado por la punta, pero no en el campo de fondo dispersado. Así, recolectando la señal del detector a las frecuencias de órdenes de armónicos altos $n\Omega$ (típicamente $n > 2$), se puede recuperar la pura señal del campo cercano.[12,13]

A las frecuencias del infrarrojo (IR), la técnica s-SNOM ofrece la posibilidad de obtener mapeos composicionales altamente sensibles basados en el sondeo de excitaciones vibracionales, como las de moléculas y fonones, de forma análoga a la microscopía infrarroja.[14] Inclusive, se pueden registrar espectros infrarrojos resueltos a la nanoescala mediante el uso de fuentes infrarrojas de banda ancha y aplicando espectroscopia infrarroja de transformada de Fourier (FTIR por sus siglas en inglés) a la luz esparcida por la punta del s-SNOM.[15] Esta última técnica – conocida como espectroscopia nano-FTIR – produce espectros de fase del campo cercano que coinciden en buena medida con las propiedades absorbentes de muestras orgánicas[15–17] y, por lo tanto, permite la identificación química a la nanoescala basada en referencias estándar de FTIR.[18]

Cabe mencionar que la luz IR que es nanoenfocada por debajo de la punta, no solo sondea el área nanométrica (bidimensional) por debajo de la punta, sino que de hecho sondea el volumen (tridimensional) nanométrico por debajo de ésta[19–22] – a pesar de que la microscopía

del campo cercano es una técnica de escaneo de superficie. También es importante señalar que, aunque se conocen bien las capacidades de la técnica s-SNOM para sondear materiales subsuperficiales[19,23–27], sólo existen algunos estudios sistemáticos en la materia.[20,21,28] Particularmente, la potencialidad de la técnica y su capacidad para analizar materiales subsuperficiales mediante el uso de espectroscopia nano-FTIR es un terreno que ha sido muy poco explorado. En esta tesis, se utiliza la espectroscopia infrarroja de campo cercano (nano-FTIR) basada en s-SNOM para analizar muestras nanoestructuradas que consisten en una variedad de capas delgadas de tamaño nanometrico.

La tesis se encuentra estructurada de la siguiente forma:

En el **capítulo 3** se explican las técnicas s-SNOM y nano-FTIR. Primero se introduce la espectroscopia infrarroja con resolución espacial nanométrica, seguido de una descripción del principio del funcionamiento del SNOM por dispersión; así como la supresión de la luz de fondo dispersada mediante la modulación de la altura de la punta, y una demodulación en señales armónicas de orden alto. Se pone especial énfasis en los diferentes modelos matemáticos que describen la interacción entre el campo cercano de la punta y la muestra. Estos modelos permiten una descripción de los contrastes espectrales observados en los experimentos de s-SNOM y nano-FTIR. Asimismo, se discute brevemente como la interacción del campo cercano, entre la punta y las muestras multicapa, debe de ser descrita considerando los coeficientes de reflexión de Fresnel de la muestra que a su vez dependen del momento del campo cercano. Finalmente, se presenta una implementación típica de una configuración nano-FTIR experimental basada en AFM. Primero, introduciendo el principio del funcionamiento del espectrómetro FTIR, el modo dinámico del AFM y finalmente describiendo la configuración empleada en la técnica nano-FTIR. Lo anterior permite la detección de espectros de amplitud – y fase – en el infrarrojo con resolución espacial nanométrica.

El **capítulo 4** aborda el desafío de detectar una capa molecular (en este caso óxido de polietileno o PEO) que es más delgada que el volumen de sondeo y que se coloca sobre sustratos IR estándar, como CaF_2. Como se muestra en la Figura 2.1b (la curva verde), la señal de amplitud s_4 del nano-FTIR de dicha muestra es considerablemente débil. Por lo tanto, para mejorar la sensibilidad del nano-FTIR en capas delgadas moleculares, se demuestra que hay un aumento significativo en la señal al colocar la capa molecular sobre sustratos altamente reflectantes como lo son el silicio u oro (líneas naranja y negra, respectivamente). Más aún, se observa que hay un aumento en la señal al explotar el mecanismo de acoplamiento entre la punta y los polaritones de la muestra, o por iluminar la punta con polaritones de superficie. Cuando las vibraciones moleculares coinciden con la resonancia de la punta y el sustrato, se observa un aumento en la señal cercano a un orden de magnitud sobre un sustrato de cuarzo (c-SiO_2) fonón-polaritónico (curvas roja y azul), en comparación a los espectros nano-FTIR obtenidos sobre sustratos metálicos (Au, véase la curva negra), y hasta dos órdenes de magnitud en comparación a los espectros obtenidos sobre el sustrato estándar de la

espectroscopia infrarrojo CaF_2 (curva verde). En el recuadro de la Figura 2.1b se muestra el contraste espectral que se asigna al modo vibracional del PEO, es decir, después de restar la señal del cuarzo. El aumento en la señal se debe, por un lado, a una mayor interacción del campo cercano entre la punta y la muestra (ilustrada en la Figura 2.1a por las líneas curvas y el área sombreada debajo del ápice de la punta) y, por otro lado, a la eficiente iluminación en la punta de sondeo y la eficiente detección

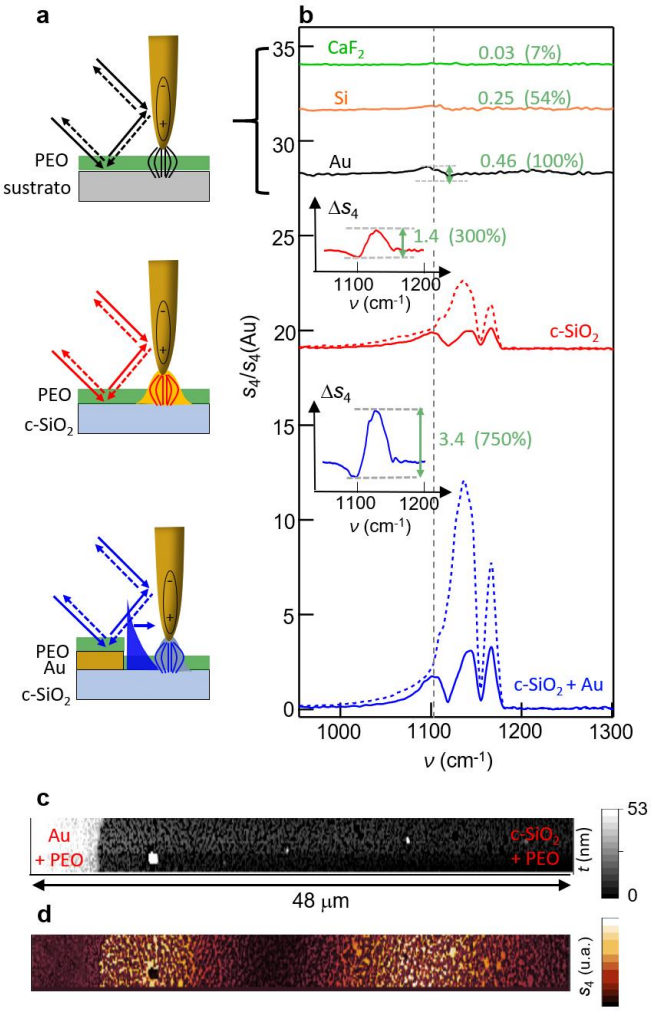

Figura 2.1: Comparción de diferentes sustratos de la espectroscopia nano-FTIR del PEO. (a) Esquemas de los diferentes mecanismos que contribuyen a la iluminación de la punta en los experimentos realizados. De arriba a abajo: iluminación indirecta de la punta a través del sustrato (esquema superior), más un acoplamiento resonante de la punta y el sustrato debido a la excitación del fonón-polaritón en el sustrato (esquema en el medio), más iluminación de la punta a través de la propagación de fonones-polaritones de superficie expulsados por el borde de una superficie de oro (esquema inferior). (b) De arriba a abajo: espectros de amplitude nano-FTIR del PEO en sustratos de CaF_2, Si, Au y cuarzo (c-SiO_2) (curvas sólidas). El espectro inferior se obtuvo a una distancia de 1 μm del borde de una película de oro extendida donde se excitan fonones-polaritones de superficie. Las líneas punteadas muestran los espectros en ausencia del PEO. Los espectros están desplazados verticalmente para enfatizar las características vibracionales del PEO. Recuadros: Las curvas roja y azul muestran el contraste espectral Δs_4 del PEO, es decir, se ha restado la señal del sustrato de cuarzo. Nótese que la escala de los ejes verticales Δs_4 and s_4/s_4(Au) es la misma. La figura se recuperó de la referencia [30].

de la luz dispersada por la punta mediante la reflexión en la superficie de la muestra (flechas sólidas y discontinuas, respectivamente). Además, la punta se ilumina mediante la propagación de fonones-polaritones de superficie que se excitan en el borde de una película de oro (indicado por el área azul en el esquema inferior). Es importante señalar que los resultados obtenidos en este capítulo son fundamentalmente importantes para impulsar la espectroscopia nano-FTIR hacia la detección rutinaria de monocapas y moléculas individuales.

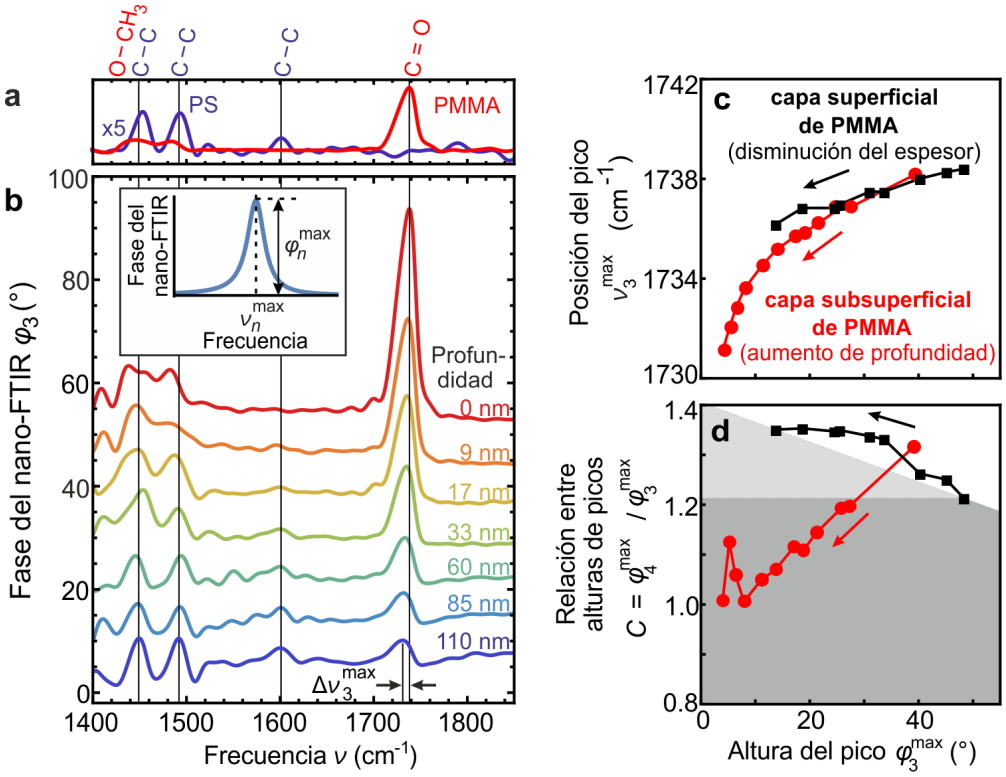

Figura 2.2: Experimentos de la espectroscopia nano-FTIR en muestras multicapa bien definidas. (a) Espectros de referencia de la fase φ_3 (obtenidos con nano-FTIR) de capas gruesas de polimetilmetacrilato (PMMA) y poliestireno (PS). (b) Espectros de la fase, obtenidos por nano-FTIR, de capas subsuperficiales de PMMA a diferentes profundidades por debajo del PS. Las flechas negras indican un desplazamiento spectral, $\Delta\nu_3^{max}$, del pico correspondiente al modo vibracional C=O del PMMA. Recuadro: Definición de la posición del pico espectral ν_n^{max} y la altura del pico φ_n^{max} para cada orden n de la demodulación. (c) Posiciones espectrales de los picos ν_3^{max} y (d) relación $C = \varphi_4^{max}/\varphi_3^{max}$ entre las alturas de los picos, de capas superficiales de PMMA (símbolos negros) y de capas subsuperficiales de PMMA (símbolos rojos). Las gráficas (c,d) se muestran en función de la altura φ_3^{max} del pico correspondiente (datos experimentales). Las flechas negras indican disminución del espesor de la capa superficial de PMMA y las flechas rojas aumento de la profundidad de la capa subsuperficial de PMMA. El espesor de la capa subsuperficial de PMMA es de 59 nm. (d) Las áreas grises indican los espacios que corresponden a los materiales subsuperficiales. Figura adaptada de acuerdo a la referencia [22].

En el **capítulo 5** se presenta la espectroscopia nano-FTIR de capas orgánicas *sub*superficiales (véase la figura Figura 2.2a,b). De la espectroscopia se observa que los espectros nano-FTIR de capas superficiales delgadas difieren de los espectros de las capas subsuperficiales del mismo material orgánico. En particular, se encuentra que los picos en los espectros de fase del nano-FTIR de capas orgánicas subsuperficiales se desplazan al rojo en comparación con los espectros nano-FTIR del correspondiente bulto del material y que, el desplazamiento al rojo es mayor al que se observa al reducir el ancho en las capas superficiales (véase la figura Figura 2.2c). Estas observaciones experimentales se confirman y se explican utilizando un modelo semianalítico para el cálculo de los espectros nano-FTIR de muestras orgánicas multicapa. El modelo también muestra que los desplazamientos del los picos en los espectros nano-FTIR de muestras multicapa pueden recuperarse de los coeficientes de reflexión de Fresnel cuasi-electrostáticos dependientes del momento $\beta(\nu,q)$, siempre que puedan desconsiderarse los desplazamientos en los picos inducidos químicamente. Asimismo, en este capítulo se estudia la correlación de las diferentes características de los picos obtenidos por nano-FTIR, y se establece una metodología simple y robusta capaz de distinguir capas superficiales de capas subsuperficiales sin la necesidad de implementar modelos teóricos o simulaciones (nuevamente, siempre y cuando no haya modificaciones espectrales inducidas químicamente). Se demuestra que las capas superficiales y subsuperficiales se pueden diferenciar analizando la relación entre las alturas de los picos obtenidos a diferentes órdenes n de demodulación de armónicos altos (véase la figura Figura 2.2d, según el criterio de la relación entre las alturas de los picos, los puntos en las áreas grises corresponden al material subsuperficial). Los resultados son fundamentalmente importantes para la interpretación de los espectros nano-FTIR de muestras multicapa, en particular para evitar que los cambios en los picos espectrales inducidos por la geometría se expliquen mediante efectos químicos.

En resumen, en esta tesis se demuestra el papel tan crucial que juegan los sustratos altamente reflectantes para aumentar las señales de nanoespectroscopia infrarroja de capas moleculares delgadas. Se muestra que hay una mejora aún mayor en la señal implementando iluminaciones adicionales a la punta, que incluyan (i) la iluminación indirecta a la punta mediante superficies metálicas altamente reflectantes o (ii) mediante la excitación de polaritones de superficie. Lo anterior, produce un aumento en casi un orden de magnitud en la señal espectroscópica del nano-FTIR de vibraciones moleculares, en comparación a la señal obtenida en nano-FTIR empleando sustratos de oro. Asimismo, este trabajo exhibe la relación directa que hay entre los espectros de nano-FTIR y los coeficientes de reflexión de Fresnel cuasi-electrostáticos dependientes del momento para muestras multicapa. Esta relación facilita la interpretación de los espectros nano-FTIR de dichas muestras, por ejemplo, para distinguir desplazamientos en los picos ocasionados por efectos químicos, de aquellos desplazamientos en los picos ocasionados por efectos geométricos. Finalmente, se observa que los desplazamientos de los picos determinados por la muestra y el momento, no son propiedades exóticas de la espectroscopia de campo cercano, sino que también ocurren en la espectroscopia de campo lejano donde el momento sondeado está determinado por el ángulo de incidencia. Cabe señalar que los resultados que se presentan en los capítulos 4 y 5 fueron previamente publicados en las referencias [30] y [22], respectivamente.

3 Nanoscale-resolved infrared spectroscopy

Near-field microscopy enables nanoscale-resolved imaging and spectroscopy beyond the diffraction limit of electromagnetic waves, independent of the illumination wavelength. In this thesis, scattering-type scanning near-field microscopy (s-SNOM) is used for imaging and nano-FTIR spectroscopy is used for recording infrared spectra. In both techniques, infrared radiation of a laser source is focused onto an AFM tip near the sample and the tip-scattered light is recorded in an interferometer setup. This chapter first gives a brief overview about infrared s-SNOM and nano-FTIR, followed by a description of their working principle and an overview over several mathematical models that describe the near-field interaction between tip and sample and which are used to describe s-SNOM and nano-FTIR contrasts between materials with different optical properties. The working principles of Fourier-transform infrared spectroscopy and tapping-mode AFM are explained in the context of the experimental setup that is used for nano-FTIR spectroscopy.

3.1 Introduction

Microscopy and Spectroscopy techniques based on the interaction between electromagnetic waves and matter are powerful tools for the analysis of materials and objects.[31,32] The application potential of such light-based techniques is seeming endless and goes far beyond that of visible light microscopy, which is used for example to investigate the inner structure of biological materials. To give a few examples, consider for example that (i) medical doctors use X-ray light to monitor fractured bones, (ii) a sunburn (caused by long exposure of human skin to ultra-violet light coming from the sun) can be identified by a red skin colour and (iii), a more recent example, the entrances of many cafés, airports or even nanoGUNE are equipped with infrared cameras that measure the body temperature of every visitor, in order to detect a fever which is among the most common symptoms of the rapidly spreading coronavirus disease COVID-19. All the previous examples have in common, that light is used to gain information about the same "matter" (in this case the human body). The difference between the given examples is that light of different photon-energies is used – i.e. a different part of the electromagnetic spectrum (Figure 3.1) is used. A strong interaction between light and matter is observed when the photon energy matches the excitation energy of a fundamental excitation in the material, which ultimately leads to the different information that is obtained.

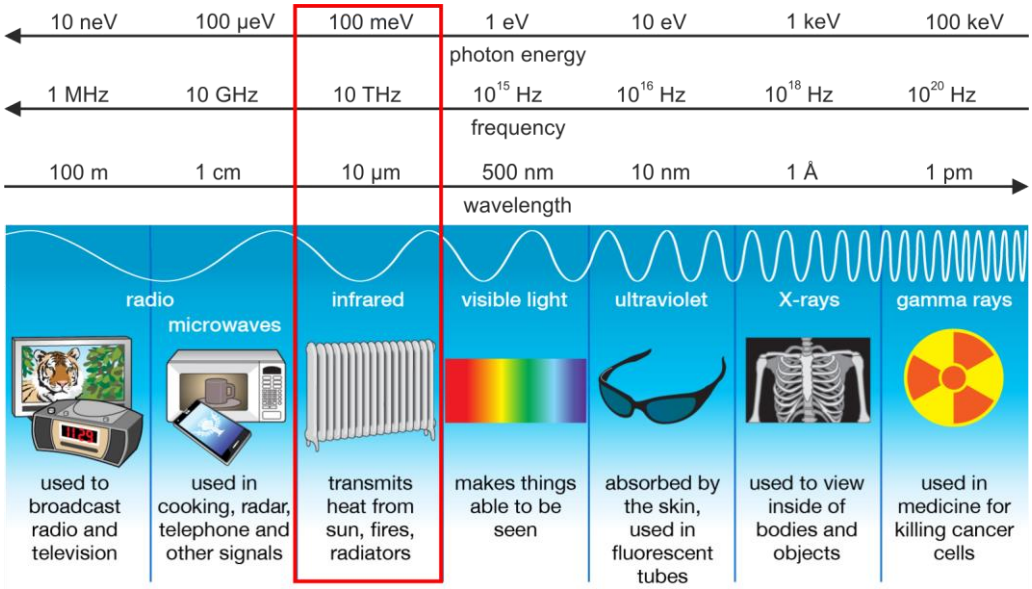

Figure 3.1: Electromagnetic spectrum. Different types of electromagnetic radiation are characterized by their photon energy, frequency and wavelength and are sensitive to various material properties (as illustrated). Importantly, the infrared spectral range is also highly sensitive to molecular vibrations which allows for chemical identification of materials. Figure adapted from [33].

In this work, light of the infrared (IR) spectral range with wavenumbers 400 to 4000 cm^{-1} is used (corresponding to the wavelength range 25 to 2.5 μm and photon-energy range 50 to 500 meV). Most importantly, the photon energy of IR light matches the excitation energy of many molecular vibrations in organic materials such as polymers and proteins, and vibrations in the crystal lattice of inorganic materials such as quartz or silicon carbide.[14,34,35] In IR spectroscopy (most commonly Fourier-transform IR spectroscopy[14], FTIR), the light transmitted through a sample or reflected at a sample surface is recorded for a wide range of IR frequencies, yielding an infrared spectrum that typically contains a plethora of peaks caused by different excitations. The number of peaks, spectral peak positions and relative intensities of peaks can be compared with an IR spectral database, which allows for an unambiguous chemical identification of materials in a sample. The IR spectral range is therefore often referred to as "fingerprint" spectral range. However, in classical (far-field) IR spectroscopy the spatial resolution is limited by diffraction, which means for IR light with a typical wavelength of $\lambda \approx 10$ μm a spatial resolution of $\Delta x \approx \lambda/2 \approx 5$ μm.[10,32,36] On the other hand, samples with nanoscale phase-separated properties become increasingly important,[37,38] and thus classical (far-field) IR spectroscopy is reaching its limits, as illustrated in Figure 3.2a-c.

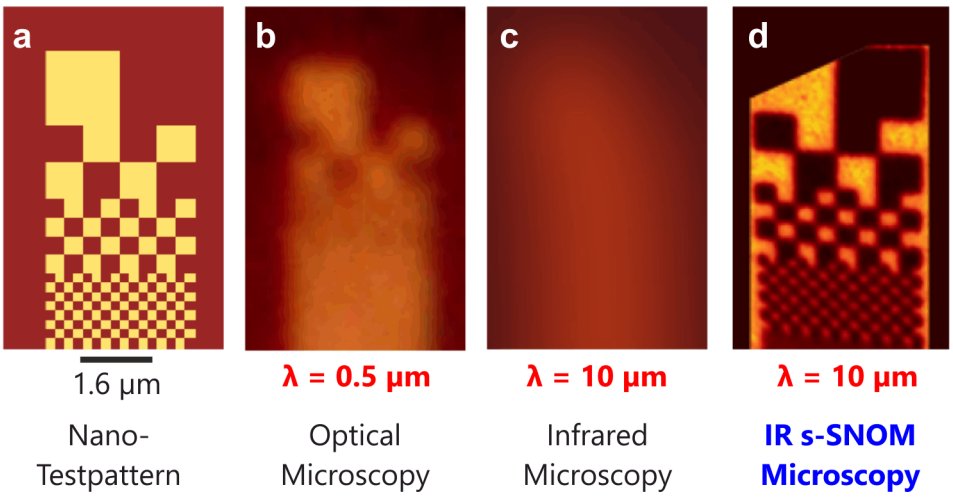

Figure 3.2: Diffraction-limited imaging in comparison with s-SNOM imaging. (a) Chequerboard test pattern comprised of 1.6 µm to 200 nm small structures, fabricated by implanting Ga+ ions (bright areas) using focused ion beam into a silicon carbine crystal (dark areas). (b-c) Diffraction-limited images recorded using (b) visible light, wavelength λ = 0.5 µm, and (c) infrared light, λ = 10 µm. (d) s-SNOM image recorded at λ = 10 µm. Images taken from [13,39,40].

A spatial resolution beyond the diffraction limit is achieved (Figure 3.2d) using near-field microscopy and near-field spectroscopy techniques such as scattering-type scanning near-field optical microscopy[1–3] (s-SNOM), photothermal expansion microscopy[41,42] (PTE) and photo-induced force microscopy[43,44] (PiFM). The diffraction limit is circumvented in all these techniques by focussing light (diffraction limited) onto a sharp metallized AFM tip, which acts as an optical antenna and creates an electromagnetic hotspot at the tip apex – thus nano-focusing the light (Figure 3.3).[2,10,11] The nano-focussed light strongly interacts with the sample region located directly below the tip (i.e. located within the near fields produced by the tip), enabling nanoscale-resolved imaging with a spatial resolution that is determined by the tip apex radius.[2,45] In s-SNOM, the sample is scanned below the tip and the tip-scattered light is recorded as a function of sample position, yielding optical images with a wavelength-independent spatial resolution in the order of the metallized tip radius,[5,6] typically $R \approx 30$ nm. In combination with IR light, a spatial resolution of $\Delta x \approx \lambda/400$ is routinely achieved. By analysing the tip-scattered light with a Michelson interferometer setup[46] (analogously to FTIR spectroscopy), chemical analysis on the nanoscale and beyond the diffraction limit is possible – the technique is therefore often called nano-FTIR.[15]

To prevent any confusion, I emphasize that throughout this thesis the illumination frequency $\nu = 1/\lambda$ is given in spectroscopic wavenumbers [cm^{-1}] and the angular frequency $\omega = 2\pi c\nu$ in radian per second [rad/s^{-1}], where λ is the illumination wavelength and c is the velocity of light. A different convention for ω is used in the published articles related to the results chapters 4 and 5.

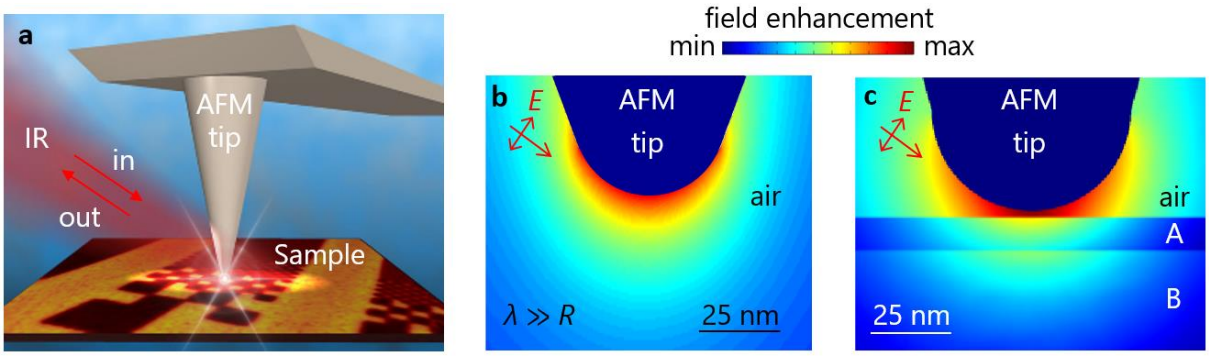

Figure 3.3: Working principle of s-SNOM and nano-FTIR. (a) A focused infrared (IR) laser beam illuminates a metallized AFM tip which is in contact with a sample. The tip-scattered light depends on the sample region which is located directly below the tip apex. (b) Simulated electric field distribution showing that the tip acts as optical antenna and concentrates the incident electric field *E* into a nanoscale-sized electromagnetic hotspot directly below the tip apex, in which the field enhancement is large. Tip radius $R \approx 30$ nm and illumination wavelength $\lambda \approx 10$ µm. Calculation by J. Aizpurua, San Sebastian. (c) The (near) fields of the hotspot penetrate into the sample, thus probing a three-dimensional volume of the sample. Image taken from [22].

Most importantly for the results presented in this thesis, the IR light that is nano-focussed below the tip does not only probe a nanometric area below the tip, but in fact probes a nanometric (three-dimensional) volume below the tip (Figure 3.3c)[19–22] – despite near-field microscopy being a surface-scanning technique. Although the capability of s-SNOM for probing subsurface materials is well-known,[19,23–27] only few systematic studies on the subject exist[20,21,28]. However, particularly the potential capability for subsurface material analysis using nano-FTIR spectroscopy is largely unexplored terrain. In this thesis, infrared near-field spectroscopy (nano-FTIR) based on s-SNOM is used to analyse nanostructured samples, which consist of several thin layers within the nano-FTIR probing volume (analogous to Figure 3.3c).

In this chapter 3, the working principle and experimental setup of nano-FTIR (based on s-SNOM) are explained step by step: First, the working principle of s-SNOM is explained in chapter 3.2. Next, it is explained in chapter 3.3 how pure near-field signals - free of background-contributions - are obtained by employing a modulation of the tip height and demodulation of the tip-scattered light at higher harmonics of the tip tapping frequency. A special emphasis is put in chapter 3.4 onto analytical models describing the near-field interaction between tip and sample, thus allowing for the description of material contrasts observed in s-SNOM and nano-FTIR and allowing for detailed insights into the underlying mechanisms that are relevant for subsurface probing and signal enhancement. In chapter 3.5 the working principle of FTIR spectroscopy is explained, as it sets the foundation for nano-FTIR spectroscopy Finally, the experimental realization of amplitude- and phase-resolved nano-FTIR spectroscopy is briefly discussed in chapter 3.6, introducing also the concepts of tapping-mode AFM.

3.2 Working principle of s-SNOM and nano-FTIR

s-SNOM is based on illumination of an AFM tip in proximity to a sample, and detection of the tip-scattered light - the latter being modified by the near-field interaction between the tip and sample. The s-SNOM probing process is sketched in Figure 3.4. The metallized AFM tip in close vicinity to a sample is illuminated directly by an electric field $\boldsymbol{E_0}$ and indirectly by an electric field $r\boldsymbol{E_0}$, yielding a total illuminating field $\boldsymbol{E_{in}} = (1+r)\boldsymbol{E_0}$, where r is the sample's Fresnel reflection coefficient for an angle of incidence Θ (measured from the normal to the sample surface).

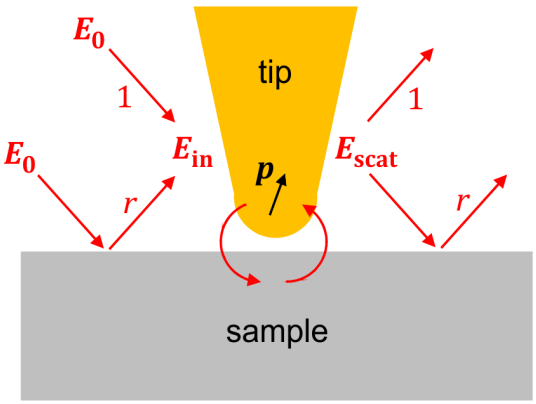

Figure 3.4: s-SNOM and nano-FTIR probing process. An AFM tip in close vicinity to a sample is illuminated by the incident electric field $\boldsymbol{E_{in}}$, which consists of a direct beam (left arrow labelled as "1") and an indirect beam (left arrow labelled as "r") that is reflected from the sample surface with reflection coefficient r. The illumination induces an effective electric dipole $\boldsymbol{p}$ in the tip, that depends on the tip polarizability and the near-field interaction between the tip and sample (illustrated by curved arrows). The intensity of the tip-scattered electric field $\boldsymbol{E_{scat}}$ is detected directly (right arrow labelled as "1") and indirectly (right arrow labelled as "r") after reflection from the sample surface, yielding the nano-FTIR amplitude s and phase φ.

The coupled tip-sample system has an effective polarizability $\boldsymbol{\alpha_{eff}}$ and thus an electric dipole $\boldsymbol{p} = \boldsymbol{\alpha_{eff}} \cdot \boldsymbol{E_{in}}$ is induced in the tip. The dipole $\boldsymbol{p}$ scatters light directly and via reflection at the sample surface into the far field, yielding the total scattered field $\boldsymbol{E_{scat}} \propto (1+r)\boldsymbol{p}$. Finally, the ratio E_{scat}/E_{in} between scattered and incident field is determined using an interferometric detection scheme (explained below), yielding the complex-valued scattering coefficient, $\sigma \propto E_{scat}/E_{in}$, which relates to the s-SNOM and nano-FTIR amplitude s and phase φ according to[4,47,48]

$$\sigma = s e^{i\varphi} \propto (1+r)^2 \, \alpha_{eff}. \tag{3.1}$$

Specifically,

$$s = \mathrm{Abs}\left[(1+r)^2 \, \alpha_{eff} \right], \tag{3.2}$$

$$\varphi = \mathrm{Arg}\left[(1+r)^2 \, \alpha_{eff} \right]. \tag{3.3}$$

It is interesting to note that Equations (3.2) and (3.3) can be separated into a near-field contribution α_{eff} and a far-field contribution $(1+r)^2$, and thus nano-FTIR signals contain a far-field contribution coming from a diffraction limited area of the sample. The far-field contribution can lead to undesired effects such as peak shifts in nano-FTIR spectra (chapter 5) but on the other hand can also be exploited e.g. to enhance the sensitivity in nano-FTIR experiments (chapter 4). It is often overlooked that the far-field contribution is always present in experimental nano-FTIR spectra, even if all background-scattering is perfectly suppressed (as explained in the following).

3.3 Separation of near-field and background-scattering

In nano-FTIR experiments based on s-SNOM, the scattered light that is detected contains a tip-scattered near-field contribution, σ_{NF}, and a background contribution, σ_{BG}, the latter originating for example from the tip shaft or a diffraction-limited area of the sample. In order to suppress the unwanted background-scattering, and thus to obtain the pure near-field response of a sample, nano-FTIR experiments employ tip modulation and higher harmonic signal demodulation.[12,13] The procedure is briefly explained in Figure 3.5. The probing tip is oscillating vertically at a frequency Ω with typical oscillation amplitudes A of a few 10 nm (Figure 3.5a,c), yielding the tip-sample separation distance

$$H(t) = H_0 + A(1+\cos\Omega t). \tag{3.4}$$

Due to the exponential decay of near-fields, the tip experiences strong near-fields at the sample surface and almost no near-fields at large tip-sample distances (red curve in Figure 3.5b).[10] On the other hand, the intensity of background light varies on the scale of the wavelength λ (in the mid-IR spectral range $\lambda_{\text{IR}} \approx 5$ - 10 µm), yielding an almost linear intensity variation on the scale of the tip tapping amplitude (blue curve in Figure 3.5b).[12] As a result of such linearity, the background scattering σ_{BG} follows the harmonic sinusoidal motion of the tip in time (blue curve in Figure 3.5d). In contrast, the near-field scattering σ_{NF} is modulated anharmonically (red curve in Figure 3.5d). This is more clearly seen by expressing the total scattering coefficient σ as a Fourier series,

$$\sigma = \sigma_{\text{NF}} + \sigma_{\text{BG}} = \sum_{n=-\infty}^{\infty} \left[\sigma_{\text{NF},n} + \sigma_{\text{BG},n}\right] e^{in\Omega t}, \tag{3.5}$$

and plotting the n-th order Fourier components $\sigma_{\text{NF},n}$ and $\sigma_{\text{BG},n}$ of the near-field and background contributions to the tip-scattered light (Figure 3.5e, showing absolute values). Evidently, the background scattering $\sigma_{\text{BG},n}$ (blue) is strongly suppressed at frequencies $n\Omega$ with $n > 1$. In contrast, the near-field scattering $\sigma_{\text{NF},n}$ (red) still contributes to frequencies $n\Omega$ with $n \geq 2$.[2,12,13]

Thus, background-free near-field signals are obtained by measuring the tip-scattered light σ at higher harmonic frequencies $n\Omega$ of the tip-oscillation frequency Ω, yielding the demodulated scattering coefficient σ_n. Experimentally, the intensity of the tip-scattered light is measured

interferometrically as a function of time, and a digital lock-in amplifier isolates the signals at frequencies $n\Omega$, directly yielding the demodulated nano-FTIR signal σ_n. The demodulation order n is chosen as a trade-off between sufficient background suppression and signal-to-noise ratio (as seen in Figure 3.5e, the near-field scattering is suppressed for very large n, but the overall signal strength decreases).

Mathematically, the n-th order demodulated signal σ_n is obtained by calculating the tip-scattered light σ (e.g. using the models described in the following chapter 3.4) as a function of time t for one oscillation cycle of the tip-sample separation distance, Equation (3.4), and taking the n-th Fourier coefficient $\hat{F}_n$ with respect to time,

$$\sigma_n = \hat{F}_n[\sigma(H(t))] \propto \int_0^{2\pi/\Omega} \sigma(H(t)) e^{in\Omega t}\, dt. \tag{3.6}$$

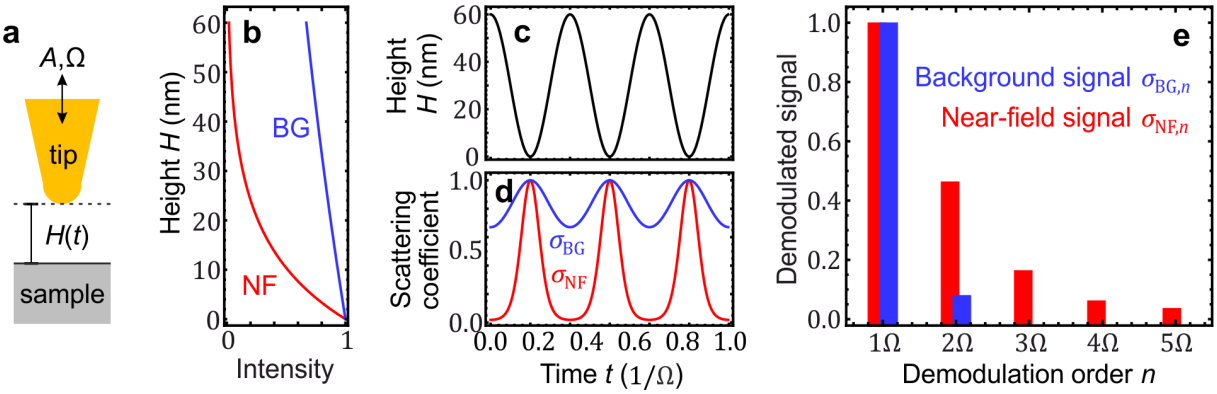

Figure 3.5: Background-suppression by tip modulation and signal demodulation. (a) Illustration of the tip oscillating vertically with tapping amplitude A and tapping frequency Ω, yielding the modulated tip height $H(t)$. (b) Intensity profiles of near fields (red, labelled NF) and of background light (blue, labelled BG) sketched as a function of tip-sample separation distance H. (c) Time-trace of $H(t)$ showing three oscillation cycles with A = 30 nm. (d) Time-trace of the scattering coefficient obtained by assuming that the tip-scattered light is proportional to the intensity at the tip. (e) Fourier series of the scattering coefficient in panel c, showing that at higher harmonic frequencies $n\Omega$ with $n \geq 2$ the background scattering (blue) is suppressed and the pure near-field scattering (red) is obtained. The figure shows only absolute values of scattering coefficients.

3.4 Near-field interaction between tip and sample

This theory chapter introduces several analytical models which employ different strategies to describe the near-field interaction between the probing tip and the sample - thus allowing for the calculation of material contrasts observed in s-SNOM and nano-FTIR spectroscopy. For a quantitative agreement between calculated and experimental contrasts, the tip modulation and higher harmonic signal demodulation

described in chapter 3.3 has to be accounted for. For simplicity, the far-field contribution $(1+r)^2$ to the tip-scattered light is neglected throughout this chapter.

The point dipole model (PDM, chapter 3.4.1) is the simplest nano-FTIR model that yields a qualitative agreement between calculated and experimental nano-FTIR spectra. Despite its simplicity, the PDM has successfully been used to describe the near-field response of for example polymers[49], metals[49] and semiconductors[2]. Importantly and most relevant for this thesis, the PDM has also been used to predict resonant coupling between the nano-FTIR tip and polar substrates (such as SiC or SiO_2).[39,50] The phenomenon – named localized surface phonon-polariton resonance – yields greatly enhanced near fields at the tip apex, which theoretically can be exploited to enhance sensing of thin molecular layers[51] and which is experimentally demonstrated for the first time in chapter 4.

The finite dipole model[13,48] (FDM, chapter 3.4.3) better describes the near-field distribution around the tip apex, which results in a greater quantitative agreement between calculated and experimental nano-FTIR spectra. For instance, the FDM has successfully been used to quantitatively determine the local infrared absorption[52], dielectric function[52] or carrier concentration[27,53] from nano-FTIR spectra. The extension of the FDM to layered samples[54] (chapter 3.4.4) is used in chapter 4 to verify the substrate-enhanced sensing of a thin organic layer on a phonon polariton-resonant substrate.

The PDM and FDM for layered samples both introduce a so-called coupling weight function (CWF), that describes the distribution of in-plane momenta $q = \sqrt{k_x^2 + k_y^2}$ of the reflected near fields that are provided and probed by the nano-FTIR tip. The concept of momentum-dependent probing (described by the momentum-dependent Fresnel reflection coefficient) is highly important for the correct interpretation of nano-FTIR spectra, particularly for layered samples, as discussed in chapter 3.4.5 and investigated in chapter 5.

Note that the presented models describe nano-FTIR contrasts caused by different material properties (such as changes in the sample permittivity) and that the models are not suitable to describe contrasts caused by additional electric fields at the sample surface (such as the ones produced by propagating surface polaritons). For the latter, the reader is referred to corresponding literature[55,56].

3.4.1 Point dipole model for bulk samples

The point dipole model (PDM) is illustrated in Figure 3.6a. The nano-FTIR tip is modelled as a spherical particle in air, with radius R, permittivity ϵ_t and polarizability

$$\alpha_t = 4\pi\epsilon_0 R^3(\epsilon_t\text{-}1)/(\epsilon_t\text{+}2), \tag{3.7}$$

located at a height H above the sample surface. The incident field $\boldsymbol{E_{in}}$ induces the total electric point dipole $\boldsymbol{p} = \boldsymbol{p_0} + \boldsymbol{p_1}$ in the tip, where $\boldsymbol{p_0} = \alpha_t \boldsymbol{E_{in}}$ is the primary dipole that is induced by the illuminating field and $\boldsymbol{p_1} = \alpha_t \boldsymbol{G}\cdot\boldsymbol{p}$ is induced by the near-field interaction between tip and sample. $\boldsymbol{G}$ needs to be determined, such that the product $\boldsymbol{G}\cdot\boldsymbol{p}$ describes the electric field that is produced by the dipole $\boldsymbol{p}$, reflected at the sample surface and then acts back onto the dipole $\boldsymbol{p}$ itself. The self-consistent solution

$$\boldsymbol{p} = \frac{\alpha_t}{1\text{-}\alpha_t \boldsymbol{G}} \cdot \boldsymbol{E_{in}} \equiv \boldsymbol{\alpha_{eff}} \cdot \boldsymbol{E_{in}} \tag{3.8}$$

defines the effective polarizability $\boldsymbol{\alpha_{eff}}$ of the coupled tip-sample system, which relates to nano-FTIR amplitude s and phase φ signals via $se^{i\varphi} \propto \alpha_{eff}$, Equations (3.1) - (3.3).

To determine the effective polarizability $\boldsymbol{\alpha_{eff}}$ which describes the near-field interaction between tip and sample, an expression for $\boldsymbol{G}$ in Equation (3.8) needs to be found. In the PDM, $\boldsymbol{G}$ is obtained from a simple electrostatic dipole-dipole interaction. By using the method of image charges[57], the near field distribution that is produced by the dipole $\boldsymbol{p}$ and reflected at the sample surface is given at the position $\boldsymbol{r} = (x,y,z)$ by [57]

$$\boldsymbol{E_{refl}}(\boldsymbol{r}) = \frac{1}{4\pi\epsilon_0} \frac{3\boldsymbol{n}(\boldsymbol{p}'\cdot\boldsymbol{n}') - \boldsymbol{p}'}{|\boldsymbol{r} - \boldsymbol{r}'|^3}, \tag{3.9}$$

where $\boldsymbol{r}' = (0,0,\text{-}H\text{-}R)$ is the position of the image dipole $\boldsymbol{p}' = \pm\beta\boldsymbol{p}$, the unit vector $\boldsymbol{n}$ is directed from $\boldsymbol{r}'$ to $\boldsymbol{r}$ and $\beta = (\epsilon\text{-}1)/(\epsilon\text{+}1)$ is the electrostatic reflection coefficient of a sample with permittivity ϵ. The sign of $\boldsymbol{p}' = \pm\beta\boldsymbol{p}$ depends on the orientation of $\boldsymbol{p}$, as illustrated in Figure 3.6b. A vertical orientation of $\boldsymbol{p}$ induces the image dipole $\boldsymbol{p}' = +\beta\boldsymbol{p}$ in the sample and a horizontal orientation of $\boldsymbol{p}$ induces the image dipole $\boldsymbol{p}' = -\beta\boldsymbol{p}$ in the sample.[10] When $\boldsymbol{p}$ is oriented vertically ($\boldsymbol{p} \parallel z$), the reflected field at the position of $\boldsymbol{p}$ itself (i.e. at the centre of the sphere drawn in Figure 3.6a) is given by

$$\boldsymbol{E_{refl}}(0,0,H\text{+}R) = \frac{1}{16\pi\epsilon_0} \frac{\beta\boldsymbol{p}}{(H\text{+}R)^3} \equiv G_z\boldsymbol{p} \tag{3.10}$$

from which we identify G_z, which carries the index z to show that $\boldsymbol{p}$ is oriented vertically. By plugging G_z into Equation (3.8) we obtain

$$\alpha_{eff}^z = \frac{\alpha_t}{1\text{-}\dfrac{\alpha_t\beta}{16\pi\epsilon_0(H\text{+}R)^3}}. \tag{3.11}$$

Analogously, when $\boldsymbol{p}$ is oriented horizontally ($\boldsymbol{p} \perp z$), we obtain

$$\boldsymbol{E}_{\mathbf{refl}}(0,0,H+R) = \frac{1}{32\pi\epsilon_0}\frac{\beta \boldsymbol{p}}{(H+R)^3} \equiv G_x \boldsymbol{p} \tag{3.12}$$

and

$$\alpha_{\mathrm{eff}}^{x} = \frac{\alpha_t}{1-\frac{\alpha_t \beta}{32\pi\epsilon_0 (H+R)^3}}. \tag{3.13}$$

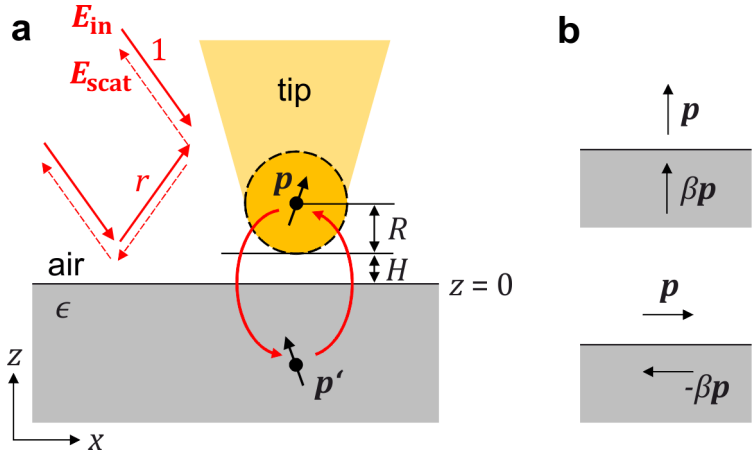

Figure 3.6: Point dipole model for semi-infinite samples. (a) The nano-FTIR tip is modelled by a spherical particle of radius R at a height H above a sample with permittivity ϵ and electrostatic reflection coefficient $\beta = (\epsilon-1)/(\epsilon+1)$. The illuminating electric field $\boldsymbol{E}_{\mathbf{in}}$ induces a point dipole $\boldsymbol{p}$ at the sphere center, which interacts with its image dipole $\boldsymbol{p}'$ induced in the sample (illustrated by curved arrows). The self-interacting dipole $\boldsymbol{p}$ produces the electric field $\boldsymbol{E}_{\mathbf{scat}}$, which is detected in the far field. The model accounts for far-field illumination and detection of the tip-scattered field via reflection at the sample surface, with Fresnel reflection coefficient r (indicated by red straight arrows). (b) Image dipole $\boldsymbol{p}' = \pm\beta\boldsymbol{p}$ illustrated for vertically oriented dipoles (upper panel) and horizontally oriented dipoles (lower panel).

Using Equations (3.11) and (3.13), we simulate the nano-FTIR amplitude s_3 on a gold sample for a vertically oriented dipole (solid curve in Figure 3.7) and a horizontally oriented dipole (dashed curve in Figure 3.7) as a function of tip-sample distance H. The calculation includes the tip height modulation and higher harmonic signal demodulation (here tip tapping amplitude A = 30 nm and demodulation order n = 3) by calculating $\alpha_{\mathrm{eff}}^{z}$ and $\alpha_{\mathrm{eff}}^{x}$ for one oscillation cycle of $H(t)$ and taking the nth-order Fourier coefficient $\hat{F}_n$ with respect to time, as explained above (Equations (3.4) and (3.6)). Both curves show that s_3 quickly decays as the tip-sample distance increases, which is typical of near field interaction between the nano-FTIR tip and the sample.[10] We further find for small tip-sample distances, that the nano-FTIR amplitude is larger when the dipole is oriented vertically, compared to a horizontally oriented dipole. A vertical orientation of the tip- and sample-dipoles leads to increased tip-sample interaction and thus an increased

effective polarizability of the tip. This increased tip-polarizability along the *z*-direction is further enhanced in nano-FTIR experiments by using probing tips with an elongated structure (with nm-sized tip apex radius and µm-sized tip shaft length). Therefore, $\alpha_{\mathrm{eff}}^{x}$ is typically and in the following neglected and only $\alpha_{\mathrm{eff}}^{z}$ is considered relevant to describe nano-FTIR amplitude and phase signals.

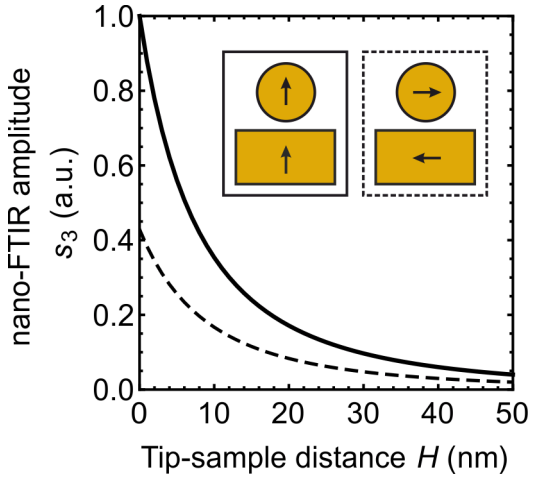

Figure 3.7: Approach curve calculated by PDM. Nano-FTIR amplitude s_3 as a function of tip-sample distance H, calculated for a vertically oriented dipole (solid curve) and a horizontally oriented dipole (dashed curve). Calculated for a gold tip and gold sample with permittivity ϵ_s = -5000+i1000, tip radius R = 30 nm, tip tapping amplitude A = 30 nm and demodulation order n = 3.

3.4.2 Point dipole model for layered samples

The PDM for layered samples[51] is illustrated in Figure 3.8a. As before, the tip is modelled as a sphere with polarizability α_t and radius R which is located at a height H above the sample surface. The sample consists of an arbitrary number of horizontally stacked layers and each layer i has a thickness d_i, permittivity ϵ_i and permeability μ_i. For simplicity, we assume that all materials are isotropic and non-magnetic, i.e. ϵ_i is a scalar and μ_i = 1. The bottom-most layer (in the figure labelled with "ϵ_4") is semi-infinite. As explained above, illumination of the tip-sample system with the electric field $\boldsymbol{E}_{\mathbf{in}}$ induces the electric dipole

$$\boldsymbol{p} = \alpha_t \boldsymbol{E}_{\mathbf{in}} + \alpha_t \boldsymbol{G} \cdot \boldsymbol{p} \tag{3.14}$$

in the sphere centre. To express the near-field induced dipole $\boldsymbol{p}_1 = \alpha_t \boldsymbol{G} \cdot \boldsymbol{p}$, Aizpurua et al. used the Green's function of a dipole located at height $z_0 = R+H$ above the sample surface.[10,51]

In the following, $\boldsymbol{G}(\boldsymbol{r_0},\boldsymbol{r_0})$ corresponds to the reflection term in the Green's function of an arbitrarily oriented dipole $\boldsymbol{p}$ located at $\boldsymbol{r_0} = (0,0,z_0)$, and the Green's function is taken at the position $\boldsymbol{r_0}$ of the dipole itself (see Appendix 6.2):

$$\boldsymbol{G}(\boldsymbol{r_0},\boldsymbol{r_0}) = \frac{i\omega^2\mu_0}{8\pi^2}\int_0^\infty [\boldsymbol{M}^{\mathbf{s}}_{\mathbf{refl}}+\boldsymbol{M}^{\mathbf{p}}_{\mathbf{refl}}]qe^{i2k_{z1}z_0}\,dq\,, \tag{3.15}$$

$$\boldsymbol{M}^{\mathbf{s}}_{\mathbf{refl}} = \frac{\pi r_s(q)}{k_{z1}}\begin{bmatrix}1 & 0 & 0\\ 0 & 1 & 0\\ 0 & 0 & 0\end{bmatrix}, \tag{3.16}$$

$$\boldsymbol{M}^{\mathbf{p}}_{\mathbf{refl}} = \frac{-\pi r_p(q)}{k_1^2}\begin{bmatrix}k_{z1} & 0 & 0\\ 0 & k_{z1} & 0\\ 0 & 0 & -2q^2/k_{z1}\end{bmatrix}, \tag{3.17}$$

where $\omega = ck$ is the angular frequency of the incident light in vacuum, the waves in medium i carry the total momentum $k_i = \frac{\omega}{c}\sqrt{\epsilon_i}$, out-of-plane momentum $k_{zi} = \sqrt{k_i^2-q^2}$ and in-plane momentum $q = \sqrt{k_x^2+k_y^2}$, and $r_s(q)$ respectively $r_p(q)$ are the reflection coefficients of the entire sample for s- and p-polarized light as a function of q. As an example, $r_p(q)$ for one layer on a substrate is given by[18]

$$r_p = \frac{r_{12}+r_{23}e^{i2k_{z2}d_2}}{1+r_{12}r_{23}e^{i2k_{z2}d_2}}, \tag{3.18}$$

with the single-interface Fresnel reflection coefficients $r_{ij} = (\epsilon_j k_{zi} - \epsilon_i k_{zj})/(\epsilon_j k_{zi} + \epsilon_i k_{zj})$ and the layer thickness d_2. Multiple layers on a substrate can be described by recursively using Equation (3.18) as expression for r_{23} or using the transfer matrix method[32].

The integral in Equation (3.15) can be interpreted as a superposition of plane waves with in-plane momenta q, which are produced by the dipole $\boldsymbol{p}$ and reflected at the sample surface. This so-called angular spectrum representation[10] is highly suited for the description of layered samples, because the in-plane momentum q is conserved across all material boundaries[10]. Figure 3.8b illustrates the momentum q in the sample plane (xy-plane) for a propagating wave (red arrow, $q \le k_1$) and an evanescent wave (blue arrow, $q > k_1$). For propagating waves, the in-plane momentum $q = k_i \sin\theta_i$ is determined by the angle of incidence θ_i with respect to the surface normal (Figure 3.8c). For evanescent waves, the large in-plane momentum $q > k_i$ leads to a fast decay of the electric fields along the z direction, which is determined by momentum conservation $k_{zi} = \sqrt{k_i^2-q^2}$ and which is illustrated in Figure 3.8d.

Equations (3.15) - (3.17) are greatly simplified by assuming a vertically oriented dipole $\boldsymbol{p} = (0,0,p_z)$. In this case, only the single matrix element G_{zz} contributes to Equation (3.14) and thus the effective tip polarizability in z-direction is given by

$$\alpha_{\mathrm{eff}}^{z} = \frac{\alpha_{\mathrm{t}}}{1-\alpha_{\mathrm{t}} G_{zz}}, \tag{3.19}$$

$$G_{zz} = \frac{\mathrm{i}\omega^2\mu_0}{4\pi k_1^2}\int_0^{\infty} r_{\mathrm{p}}(q)\frac{q^3}{k_{z1}}\mathrm{e}^{\mathrm{i}2k_{z1}z_0}\,\mathrm{d}q, \tag{3.20}$$

which in combination with Equation (3.1) describe nano-FTIR amplitude and phase spectra of samples made of an arbitrary number of isotropic layers.

Importantly and in contrast to the PDM for bulk samples, the sample response is described in Equation (3.20) by the *electrodynamic* reflection coefficient $r_{\mathrm{p}}(q)$, which for each q is weighted with the factor

$$w_{\mathrm{PDM}}(q) = (q^3/k_{z1})\mathrm{e}^{\mathrm{i}2k_{z1}z_0}, \tag{3.21}$$

that describes which momenta are provided and probed by the tip. This so-called coupling weight function (CWF) $w_{\mathrm{PDM}}(q)$ is highly important for the correct description of nano-FTIR signals[51,54,58,59] and is discussed in more detail in chapter 3.4.5.

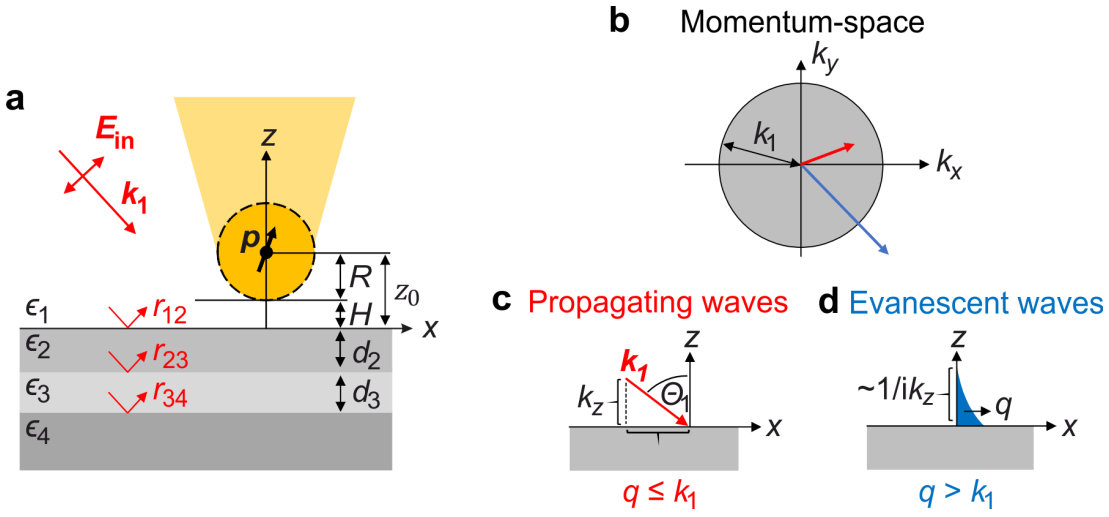

Figure 3.8: Point dipole model for layered samples. (a) The nano-FTIR tip is modelled by a spherical particle of radius R at a distance H above a layered sample. Each layer i has a permittivity ϵ_i, thickness d_i and single-interface Fresnel reflection coefficient $r_{ij}(q)$ with respect to the underlying layer j. The illuminating light with wavevector k_1 and electric field vector E_{in} induces a point dipole p at the sphere center, which interacts with the sample. (b) The in-plane momentum $q = \sqrt{k_x^2+k_y^2}$ is illustrated for a propagating wave (red arrow, $q \leq k_1$) and an evanescent wave (blue arrow, $q > k$) in comparison with the momentum k_1 of the incident light in air. (c,d) Illustrations showing the relation between (c) in-plane momentum q and incidence angle θ_1 (for propagating waves in air) and (d) in-plane momentum q and exponential decay length ik_z (for evanescent waves).

3.4.3 Finite dipole model for bulk samples

The finite dipole model[13,48] (FDM) is illustrated in Figure 3.9. The nano-FTIR tip is modelled as a perfectly conducting prolate spheroid in air, with apex radius R and major half-axis length L, located at a height H above the sample surface. Analytical calculations show that such spheroid produces (under external illumination) a near-field distribution that closely matches that of a point charge, rather than that of a point dipole or extended dipole.[48] Therefore, and in contrast to the PDM, the dipole induced in the tip is spatially extended. The primary dipole $p_0 \approx 2LQ_0$ (blue arrow in Figure 3.9) that is induced by the illuminating field E_{in} consists of the point charges $\pm Q_0$ which are located at distances $W_0 = \frac{1.31RL}{L+2R}$ from the spheroid apexes. Due to the large distance of the upper point charge ($-Q_0$) to the sample surface, it is considered to not contribute to the near-field interaction between tip and sample.

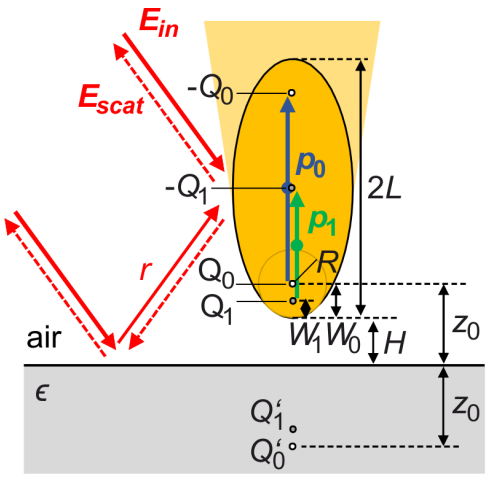

Figure 3.9. Finite dipole model for semi-infinite samples. The nano-FTIR tip is modelled by a prolate spheroid of length $2L$ and apex radius R at a distance H above a sample with permittivity ϵ and electrostatic reflection coefficient $\beta = (\epsilon-1)/(\epsilon+1)$. The illuminating electric field E_{in} induces an extended dipole $\boldsymbol{p_0}$ (blue arrow) in the tip, constituted by the point charges $\pm Q_0$ which are located at distances W_0 from the tip apexes. The point charge Q_0 creates an image charge Q_0' in the sample, which yields an additional near-field induced dipole $\boldsymbol{p_1}$ (green arrow) in the tip. The dipole $\boldsymbol{p_1}$ consists of the point charges Q_1 at a distance W_1 from the sample-near tip apex and $-Q_1$ in the spheroid center. The model accounts for far-field illumination and detection of the tip-scattered field E_{scat} via reflection at the sample surface, with Fresnel reflection coefficient r (indicated by red arrows).

In the FDM, the near-field interaction between tip and sample is described by the charge $+Q_0$, which induces an image charge $Q_0' = -\beta Q_0$ in the sample, with $\beta = (\epsilon-1)/(\epsilon+1)$ being the quasi-electrostatic Fresnel reflection coefficient for a semi-infinite sample with permittivity ϵ. The distance $z_0 = R+H$ of Q_0' to the sample surface is the same as the height of Q_0 above the sample, z_0 (method of image charges[57]). The image charge Q_0' acts back on the tip by inducing a line charge distribution in the tip, which is approximated by a point charge $Q_1 = \beta Q_0 f_0$ at a

distance $W_1 = R/2$ from the tip apex and its counter charge $-Q_1$ at the spheroid center, which together form the dipole $p_1 \approx LQ_1$ (green arrow in Figure 3.9). Self-consistent treatment of the problem yields[13]

$$Q_1 = \beta Q_0 f_0 + \beta Q_1 f_1, \tag{3.22}$$

where f_i are geometry factors depending on the tip apex radius R, spheroid major half-axis length L and tip-sample distance H, and given by

$$f_i = \left(g - \frac{R+2H+W_i}{2L}\right) \cdot \frac{\ln\left(\frac{4L}{R+4H+2W_i}\right)}{\ln\left(\frac{4L}{R}\right)} \tag{3.23}$$

with $I = \{1, 2\}$. The g-factor is a model parameter that describes the amount of the induced line charge that is still relevant for the near-field interaction. It is empirically found to be $g \approx 0.7 \pm 0.1$.[48] By expressing the total induced dipole moment $p = p_0 + p_1 = \alpha_{\text{eff}} E_{\text{in}}$ using Equation (3.22), it can be shown that

$$\alpha_{\text{eff}} \propto 1 + \frac{1}{2} \cdot \frac{\beta f_0}{1 - \beta f_1}, \tag{3.24}$$

which in combination with Equation (3.1) describes nano-FTIR amplitude and phase spectra. The proportionality is sufficient when only relative material contrasts are considered, i.e., a reference material is used to normalize nano-FTIR spectra.

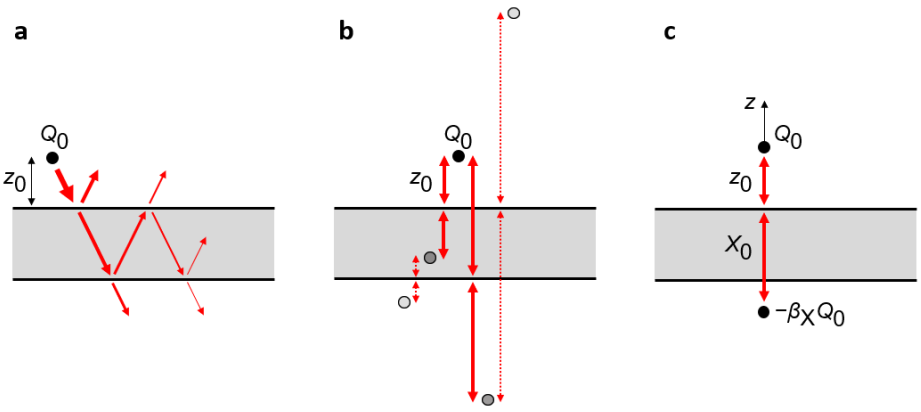

Figure 3.10: Multiple reflections inside a layered sample. A point charge Q_0 at a height z_0 above a multilayer sample produces an electric field which is repeatedly reflected at the layer interfaces, as illustrated in (a) using a ray-optics picture and (b) using an image charge picture. (c) The total reflection of the multilayer sample is described by Hauer et al. using a single effective image charge of strength $-\beta_X Q_0$ at a distance X below the sample surface.[54]

3.4.4 Finite dipole model for layered samples

The FDM in Equation (3.24) is valid only for semi-infinite samples, in which the sample response to a point charge is described with a single image charge. In layered samples, however, multiple reflections between the sample interfaces take place (Figure 3.10a), which can be described by a series of image charges (Figure 3.10b).[60] In order to extend the FDM to layered samples, Hauer et al. replaced the infinite series of image charges by one *effective* image charge (Figure 3.10c), for which the location X and strength β_X are calculated numerically.[54] To this end, Hauer et al. used the reflected electrostatic potential Φ (which is produced by a charge Q_0 at height z_0 and reflected at the surface of a multilayer sample) which along the tip-axis (z-axis) is given by[61]

$$\Phi(z) = \int_0^\infty \beta(q) e^{-2qz_0 - qz}\, dq, \tag{3.25}$$

where q is the in-plane momentum of light and $\beta(q)$ is the quasi-electrostatic reflection coefficient of the multilayer sample. As an example, $\beta(q)$ for one layer of thickness d on a substrate is given by

$$\beta(q) = \frac{\beta_{12} + \beta_{23} e^{-2qd}}{1 + \beta_{12}\beta_{23} e^{-2qd}}. \tag{3.26}$$

By the method of image charges, the reflected electrostatic potential Φ is equivalent to that of a point charge below the sample surface (the *effective* image charge). By applying the boundary conditions of the electric potential and its derivative along the surface normal $\Phi' = (\partial\Phi/\partial z)$, the following expressions for the effective charge strength β_X and effective position X are obtained:[54]

$$\beta_X = -\frac{\Phi^2}{\Phi'}\Big|_{z=0} \quad \text{and} \quad X = \frac{\Phi}{\Phi'}\Big|_{z=0} - z_0. \tag{3.27}$$

Finally, Equation (3.27) is used in modified versions of Equations (3.23) and (3.24),[54]

$$f_{i,X} = \left(g - \frac{R+H+X_i}{2L}\right) \cdot \frac{\ln\left(\frac{4L}{R+2H+2X_i}\right)}{\ln\left(\frac{4L}{R}\right)}, \tag{3.28}$$

and

$$\alpha_{\text{eff}} \propto 1 + \frac{1}{2} \cdot \frac{\beta_X f_{0,X}}{1 - \beta_X f_{1,X}}, \tag{3.29}$$

which in combination with Equation (3.1) describe nano-FTIR amplitude and phase spectra.

From a computational standpoint, it can be beneficial to introduce the dimensionless variable $\xi = q \cdot z_0$ in Equation (3.25), which yields the practical expression for the electrostatic potential

$$\Phi = \frac{1}{z_0}\int_0^\infty \beta\left(\frac{\xi}{z_0}\right) e^{-\xi(2z_0+z)/z_0}\, d\xi. \tag{3.30}$$

Note that the sample response is described in Equations (3.25) and (3.30) by the quasi-electrostatic reflection coefficient $\beta(q)$, which for each q is weighted with a weight function similar to Equation (3.21) of the PDM for multilayer samples. Specifically, the CWF of the FDM is obtained from the expression for the electric field $E_z = -\partial\Phi(z)/\partial z$ and given by[62]

$$w_{FDM} = qe^{-2qz_0} \tag{3.31}$$

In the following, the role of a CWF in nano-FTIR spectroscopy is briefly discussed, as it will be used extensively in the results chapter 5. For simplicity, only w_{PDM} is discussed and similar results are expected for w_{FDM}.

3.4.5 Momentum-dependent probing of the Fresnel reflection coefficient

In order to understand more intuitively which sample properties are actually probed in nano FTIR spectroscopy, this chapter briefly discusses the relation between the sample permittivity ϵ_s, the sample's Fresnel reflection coefficient $r_p(\nu,q)$ and the coupling weight function (CWF) $w_{PDM}(q) = (q^3/k_{z1})e^{i2k_{z1}z_0}$ of nano-FTIR (Equation (3.21)), followed by a brief comparison with far-field FTIR and total internal reflection (TIR) FTIR. To this end, we consider a layer of a hypothetical material which features a charge-carrier response and a molecular vibration in the mid-IR spectral range. The permittivity ϵ_s is described using the Drude-Lorentz model via[63]

$$\epsilon_s(\nu) = \epsilon_\infty\left(1 - \frac{\nu_p^2}{\nu^2 + i\nu\gamma_p}\right) + \frac{A_L^2}{\nu_L^2 - \nu^2 + i\nu\gamma_L}, \tag{3.32}$$

with the high-frequency permittivity ϵ_∞, plasma frequency ν_p, electronic damping rate γ_p, Lorentz oscillator strength A_L, frequency ν_L and damping rate γ_L (Figure 3.11a). Calculated nano-FTIR spectra for a layer thickness d = 200 nm (solid lines) and d = 20 nm (dashed lines) are shown in Figure 3.11b. Each amplitude spectrum (black curves) shows two spectral features with a dispersive line shape and each phase spectrum (red curves) shows two spectral peaks around ν_p and ν_L, caused by collective electron excitation and excitation of the molecular vibration respectively. Despite their similar appearance in nano-FTIR spectra, the contrasts (i.e. peak heights) differ in their relation to the sample permittivity. For weak oscillators (Re $\epsilon > 0$, including molecular vibrations of organic materials) the nano-FTIR amplitude and phase follow approximately the real and imaginary parts of the permittivity[49]. In contrast, for strong oscillators (Re $\epsilon < 0$, including plasmons or phonons), the nano-FTIR amplitude is resonantly enhanced around $\epsilon \approx -2$ (Ref. 50), owing to a resonant coupling between tip and sample, as further explained and exploited in chapter 4. Importantly, Figure 3.11b shows that nano-FTIR spectra are not entirely defined by the sample permittivity, but also depend on the sample geometry. Specifically, the nano-FTIR amplitude spectra show that the spectral peak position

associated with charge carrier excitations is strongly shifted as a function of the layer thickness *d*. In chapter 5 it is thoroughly investigated how nano-FTIR spectra of an organic layer featuring a molecular vibration are modified as function of the sample geometry (i.e. varying thickness or depth of the organic layer).

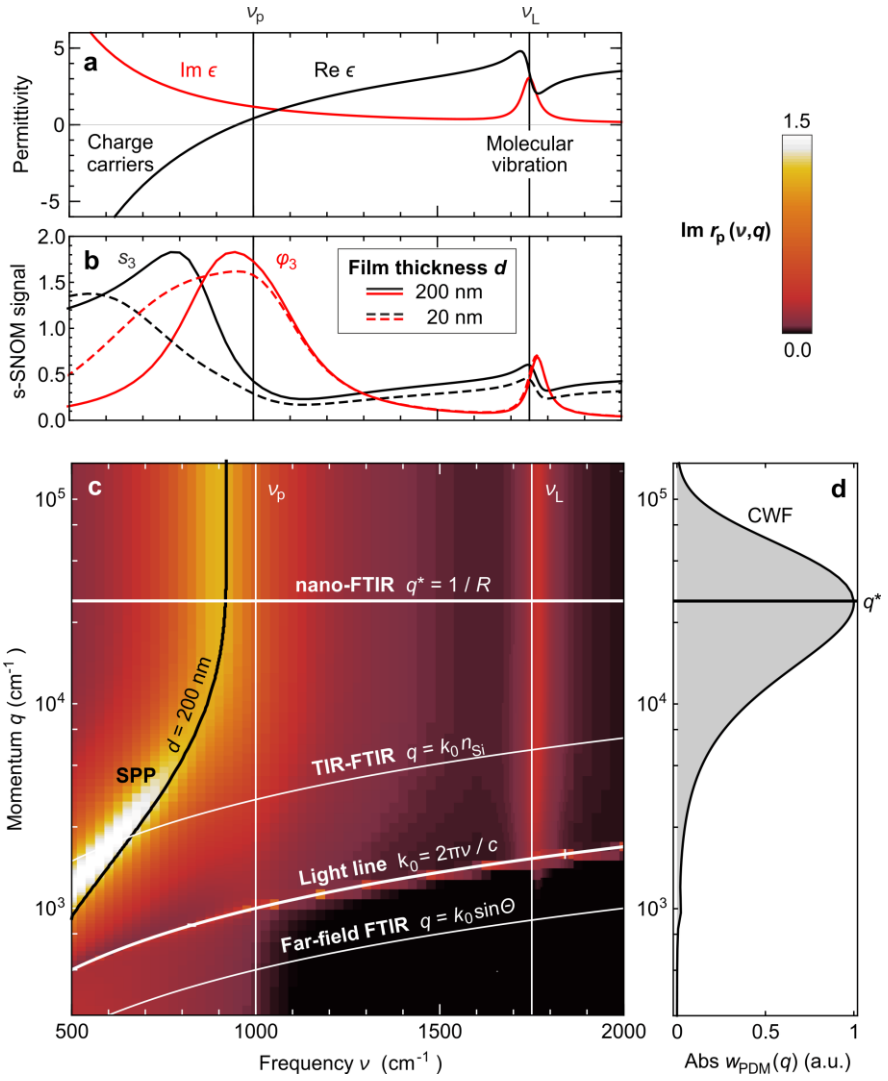

Figure 3.11: Relation between nano-FTIR spectra, the coupling weight function and momentum-dependent Fresnel reflection coefficient. (a) Real and imaginary parts of the permittivity ϵ_s for a hypothetical material described by a Drude-Lorentz model with ϵ_∞ = 5, ν_p = 1000 cm^{-1}, γ_p = 250 cm^{-1}, A_L = 500 cm^{-1}, frequency ν_L = 1750 cm^{-1} and damping rate γ_L = 50 cm^{-1}. (b) Corresponding nano-FTIR spectra of a d = 200 nm-thick layer (solid curves) and d = 20 nm-thick layer (dashed curves) in air, calculated using the PDM for layered samples for a tip radius R = 50 nm, tapping amplitude A = 25 nm and demodulation order n = 3. (c) Imaginary part of the Fresnel reflection coefficient $r_p(\nu,q)$ of the 200 nm-thick layer sample, as a function of frequency ν and in-plane momentum q. Vertical lines indicate ν_p (solid) and ν_L (dashed). The solid black curve indicates the dispersion of symmetric slab-mode SPPs in a layer of thickness d = 200 nm. White curves indicate the dispersion of free-space photons ("Light line") and the momenta probed by nano-FTIR, TIR-FTIR (n_{Si} = 3.4) and far-field FTIR spectroscopy (Θ = 30°). (d) Coupling weight function of the PDM, $w_{PDM}(q)$, for a tip-sample separation distance H = 1 nm. The horizontal line indicates q^* = 1/R.

The origin of spectral features in (nano-)FTIR spectra becomes more apparent when plotting the sample's Fresnel reflection coefficient $r_p(\nu,q)$ as a function of illumination frequency ν and in-plane photon-momentum q, rather than the sample permittivity. Figure 3.11c shows Im $r_p(\nu,q)$ for a layer of thickness d = 200 nm, calculated using Equation (3.18). The light-line (thick white line, defined by $2\pi\nu = ck_0$) indicates the photon-momentum in vacuum and separates the plot into propagating waves with $q \leq k_0$ (far fields) and evanescent waves with $q > k_0$ (near fields). The vertical bright stripe at ν_L is caused by molecular absorption and the bright yellow branch at frequencies below ν_p can be assigned to a symmetric slab-mode surface plasmon polariton (SPP), as confirmed by plotting the dispersion of such SPP (solid black curve), defined by[64]

$$\epsilon_s(\nu)k_{z,air} + \epsilon_{air}k_{z,s}\coth\frac{k_{z,s}d}{2} = 0. \tag{3.33}$$

To intuitively connect the Fresnel reflection coefficient (Figure 3.11c) and the nano-FTIR spectra (Figure 3.11b), we need to consider that nano-FTIR signals are determined by near fields which are provided by the tip and reflected at the sample surface back to the tip itself. The reflection of near fields is described by the Fresnel reflection coefficient and the momentum distribution of the reflected near fields is described by the CWF (Figure 3.11d, plotted for a tip-sample separation distance H = 1 nm). The CWF has a maximum at $q^* = 1/R$, determined by the tip radius R. As a result, a rough approximation of nano-FTIR spectra is obtained as $r_p(\nu,q^*)$, corresponding to the horizontal line labelled "nano-FTIR" in Figure 3.11c.[62] The crossing-points of the "nano-FTIR"-line with the bright yellow spectral features in Figure 3.11c (caused by the free-carrier response and the molecular vibration respectively) agree well with the spectral features observed in the nano-FTIR spectra (solid curves in Figure 3.11b). This approach is sometimes called "r_p-approximation" and yields only a qualitative description of nano-FTIR spectra, but can be applied also to polariton-resonant or 2D materials.[62,65,66] Note that the electrostatic limit

$$\lim_{q\to\infty} r_p(\nu,q) \to \beta(\nu), \tag{3.34}$$

would correspond to the upper-most row of data in Figure 3.11c.

To further illustrate the value of relating infrared spectra with the momentum-dependent Fresnel coefficient, the same picture is applied in Figure 3.11c also to far-field FTIR and total internal reflection FTIR (TIR-FTIR). For a detailed explanation of the techniques, see Refs [14,67]. Data below the light line corresponds to far-field FTIR spectra, where the in-plane photon-momentum q is determined by the angle of incidence Θ via $q = k_0 \sin\Theta$ (illustrated for Θ = 30°, curve labelled "Far-field FTIR"). As is typical for the far-field reflection of Drude-like conductors, the plasma edge is clearly visible at frequencies below the plasma frequency ν_p (bottom left corner of Figure 3.11c). On the other hand, near fields with in-plane photon-momenta slightly above the light line are obtained in total internal reflection (TIR) FTIR microscopy. In TIR-FTIR employing the Otto configuration, the sample is illuminated through a medium with high refractive index (here n_{Si} = 3.4) at an angle of incidence larger than the critical angle.[10] In this case, the incident light is totally reflected inside the higher-index medium and leaky evanescent waves with momenta $q = k_0 n_{Si}$ penetrate into the sample (curve labelled "TIR-FTIR"). The

crossing-point of the "TIR-FTIR"-line with the SPP dispersion (black curve) indicates that SPPs can be excited and probed – as routinely exploited for example in molecular sensors based on SPP resonances[68]. Importantly, the optical properties of the sample are entirely contained in the Fresnel reflection coefficient and different FTIR techniques (including nano-FTIR) merely probe different parts (different momenta) of the same reflection coefficient. To briefly recap, the main message of Figure 3.11 and the above discussion is that in nano-FTIR, the reflection coefficient $r_p(\nu,q)$ is probed at momenta around $q^* = 1/R$,[62,65,66] which will be further exploited in chapter 5 to explain spectral peak shifts in nano-FTIR spectra of thin organic surface and subsurface layers.

At this point it must be noted that the CWF is still poorly understood and its relation to the sample's Fresnel reflection coefficient yield only a strongly simplified description of nano-FTIR spectroscopy, and that important aspects such as the tip modulation and signal demodulation are completely neglected. This paragraph is meant to give a small overview on variations of the CWF found in literature and to highlight some of the existing problems related to the CWF. Firstly, note that for nano-FTIR spectroscopy a single value of q is insufficient to properly describe observations in nano-FTIR experiments, as the entire CWF (Figure 3.12a) must be considered. For example, the high lateral spatial resolution in s-SNOM and nano-FTIR is explained by probing strongly confined evanescent waves with high momenta $q \sim 1/R$, whereas the vertical probing depth in s-SNOM is much larger, indicating that (also) longer-reaching evanescent waves with smaller momenta $q \sim 0.1/R$ are probed.[24,54,69] This point is further discussed in chapter 5.

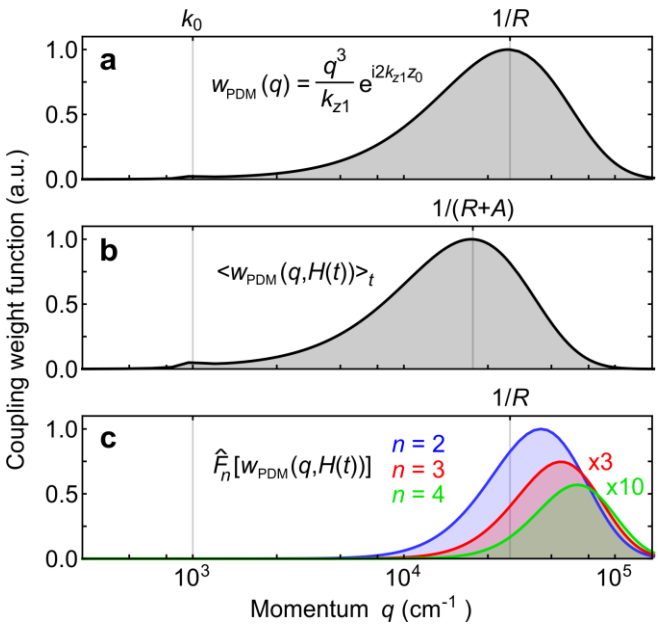

Figure 3.12: Variations of the coupling weight function (CWF). CWF of the PDM for layered samples. (a) Plotted for H = 1 nm. (b) Time-averaged CWF $<w_{PDM}(q,H(t)>_t$ over one oscillation cycle of the tip modulation $H(t)$ with tapping amplitude A = 25 nm. (c) Demodulated CWF for A = 25 nm and demodulation orders n = {2, 3, 4}. (a-c) Tip radius R = 50 nm.

Furthermore, the peak position of the CWF depends on the tip-sample separation distance H – larger distances H favouring lower momenta q. To account for the tip height modulation of nano-FTIR experiments, a time-averaged CWF $<w(q,H(t))>_t$ is therefore frequently used in literature,[66,70] which effectively shifts the CWF to *lower* momenta (Figure 3.12b). On the other hand, it is experimentally found that the spatial resolution actually increases, when the tip height is modulated and the signal is demodulated[20,21,71] – an effect also known as "virtual tip sharpening"[72,73] – which corresponds to a shift of the CWF to *higher* momenta. This apparent contradiction between experimental observations and the time-averaged CWF shows that further studies related to the CWF are needed, particularly to investigate the role of the tip modulation and signal demodulation parameters.

As of date, a direct relation between higher harmonic signal demodulation and the CWF has not yet been demonstrated. Here, a simplified "demodulated coupling weight function" is obtained (for illustrative purposes only) by modulating the tip height and taking the n-th order Fourier coefficients $\widehat{F}_n$ of $w_{\mathrm{PDM}}(q,H(t))$ with respect to time (analogous to Equation (3.6)). The demodulated CWF (Figure 3.12c) describes well that the spatial resolution is increased by tip modulation and signal demodulation, i.e. that the CWF is shifted to higher momenta compared to the standard CWF (Figure 3.12a). Furthermore, the shift increases for higher demodulation orders n, which is consistent with the further increased spatial resolution at larger n observed in s-SNOM experiments. Note that Figure 3.12c should be used with care, as a more rigorous (and by no means trivial) derivation is needed that accounts for multiple reflections of near fields between tip and sample (i.e. account for the full nano-FTIR model such as the PDM).

3.5 Fourier-transform infrared spectroscopy (FTIR)

In this chapter the working principle of FTIR spectroscopy is explained, as it sets the foundation for nano-FTIR spectroscopy. This chapter essentially follows the descriptions of Refs [14,40], including the main data processing steps required to obtain infrared spectra from experimental data. A typical FTIR spectrometer is based on a Michelson interferometer setup as shown in Figure 3.13. Broadband infrared radiation of the IR light source is split by a beam splitter (BS) into two beams A and B. The two beams are reflected in the interferometer arms and (A+B) recombined at the detector position. Importantly, the two beams have an optical path length difference of $2\Delta x$, which can be adjusted by linearly translating the reference (RM) mirror along the beam axis by a distance Δx. The interference of the beams A+B varies as a function of the optical path length difference.

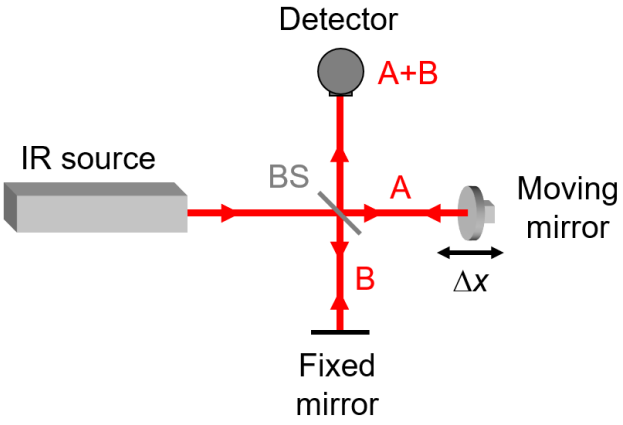

Figure 3.13: Michelson interferometer setup as used in FTIR spectroscopy. Broadband infrared radiation is split by a beam splitter (BS) into two beams A and B, which are reflected by flat mirrors and recombined by the BS at the detector position (A+B). Linear translation of a moving mirror by a distance Δx introduces a phase difference between the beams A and B, thus modifying the interference of A+B at the detector position (e.g. from constructive interference to destructive interference).

For a mathematical description of the interference, we first assume a monochromatic light source that emits a plane wave electric field $E_0 = |E_0|e^{i\nu_0 t}$ with frequency $\nu_0 = 1/\lambda_0$ (given in cm^{-1}), free-space wavelength λ_0 and intensity $I_0 \propto |E_0|^2$. The light is split by the beamsplitter into two beams $E_A = |E_A|e^{i\nu_0 t}$ and $E_B = |E_B|e^{i\nu_0 t + i\varphi_B}$ which propagate along the two paths A and B respectively, with $\varphi_B = 4\pi\nu_0\Delta x$ being the phase difference caused by a different length Δx of the interferometer arms. The magnitudes of $|E_A|$ and $|E_B|$ depend on the details of the experimental setup such as the transmission characteristics of the beamsplitter, atmospheric absorption or the spectral sensitivity of the infrared detector. Interference of the beams A and B at the detector position yields the intensity

$$I(\Delta x) \propto |E_A|^2 + |E_B|^2 + 2|E_A||E_B| \cos[4\pi\nu_0\Delta x], \tag{3.35}$$

which oscillates as a function of the path difference Δx due to $\varphi_B = 4\pi\nu_0\Delta x$. In the following,

we refer to the oscillating part of $I(\Delta x)$ as interferogram, neglecting a constant offset value. The emission spectrum $I(\nu)$ of the monochromatic light source emitting at a single frequency ν_0 and the corresponding interferogram $I(\Delta x)$ are respectively shown in Figure 3.14a,e. The interferogram shows the typical cosine oscillation described by Equation (3.35). The intensity maxima occur for $\varphi_B = 2\pi N$ (constructive interference) and intensity minima occur when $\varphi_B = 2\pi N + \pi$ (destructive interference), with N being an integer value. Importantly, the data contained in the interferogram is sufficient to determine the emission spectrum of the light source, as further elaborated in the following.

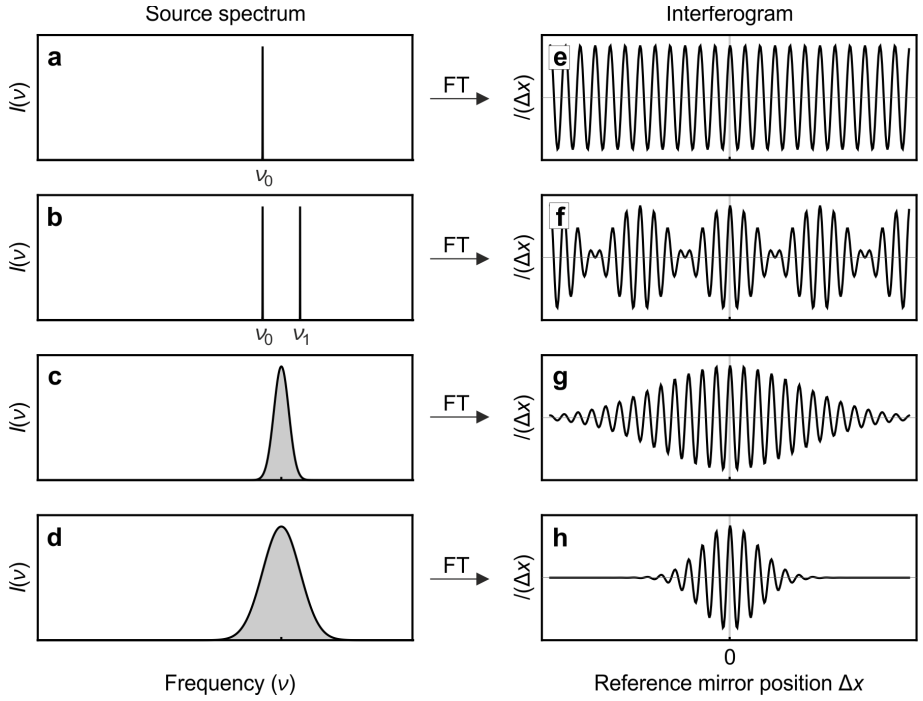

Figure 3.14: Relation between light source spectra and corresponding interferograms. (a-d) Light source emission spectra $I(\nu)$ and (e-h) corresponding interferograms $I(\Delta x)$ obtained by Fourier transformation (FT), for light sources emitting (a,e) at frequency ν_0, (b,f) at frequencies ν_0 and ν_1, (c,g) a spectrally narrow Gaussian intensity distribution and (d,h) a spectrally broad Gaussian intensity distribution.

We now consider the more relevant case when a broadband light source with an arbitrary emission spectrum $I(\nu)$ is used. In this case the interferogram is given by the super-imposed interference of all frequencies[14]

$$I(\Delta x) = \int_{-\infty}^{\infty} I(\nu) \cos(4\pi\nu\Delta x)\, d\nu. \tag{3.36}$$

Most importantly, Equation (3.36) shows that the interferogram $I(\Delta x)$ can be obtained by cosine Fourier transform of the source spectrum $I(\nu)$ and *vice versa*. In FTIR spectroscopy techniques, the interferogram is measured and the corresponding spectrum is obtained by inverse Fourier transformation thereof:[14]

$$I(\nu) = \int_{-\infty}^{\infty} I(\Delta x) \cos(4\pi\nu\Delta x)\, \mathrm{d}(\Delta x). \tag{3.37}$$

Equation (3.37) shows that it is possible to determine the spectrum $I(\nu)$ by variation of Δx (linear translation of the refence mirror), which is the basic working principle of (nano-)FTIR spectroscopy. By placing a sample in the infrared beam (for example between the BS and the detector, as in transmission FTIR spectroscopy[67]), the infrared spectrum of the sample is obtained.

To further illustrate the relation between the interferogram and source spectrum, Figure 3.14b-d exemplary show the emission spectra of different light sources with emission (b) at ν_0 and ν_1, (c) of a spectrally narrow Gaussian intensity distribution and (d) of a spectrally broad Gaussian intensity distribution, and Figure 3.14f-h show the corresponding interferograms obtained by Fourier transformation of the interferograms. The beating pattern observed in the interferogram of Figure 3.14f is typical for the interference of two waves with different frequency. A continuous broadband source spectrum yields an interferogram showing fast oscillations below an envelope function (Figure 3.14f-h). The maximum intensity is observed at the so-called white light position (WLP), at which all frequencies interfere constructively because the path difference is zero, $\Delta x = 0$. For a broader source spectrum, the envelope function of the interferogram is narrower, but still centered around the same WLP.

Spectral resolution

The integral in Equation (3.37) assumes that the reference mirror position Δx can be varied over an infinitely long distance. Experimentally however, the maximum and minimum path difference Δx is limited by the driving range of the reference mirror. As a result, the spectral resolution $\Delta\nu$ at which the spectrum $I(\nu)$ can be obtained is limited, and the spectral resolution limit is given by[40]

$$\Delta\nu_{\mathrm{min}}\left[\mathrm{cm}^{-1}\right] = \frac{10^4}{2\left|\Delta x_{\mathrm{max}}[\mu\mathrm{m}] - \Delta x_{\mathrm{min}}[\mu\mathrm{m}]\right|}. \tag{3.38}$$

In this work, the maximum interferogram length of the employed nano-FTIR setup is limited to $|\Delta x_{\mathrm{max}} - \Delta x_{\mathrm{min}}| = 800$ µm, yielding a spectral resolution that is limited to $\Delta\nu_{\mathrm{min}} = 6.25\ \mathrm{cm}^{-1}$.

To illustrate the relation between spectral resolution and the interferogram length, Figure 3.15a,e show the quasi-infinitely long interferogram (only a part of the interferogram is shown) of a bi-chromatic light source emitting at ν_0 and ν_1 and the corresponding spectrum obtained by inverse Fourier transform of the interferogram. The two sharp emission peaks at ν_0 and ν_1 are well reproduced. Figure 3.15b shows an interferogram of the same light source, but limited to a finite driving range of the reference mirror position (indicated by the red dashed line). The corresponding interferogram again yields two peaks, but with increased full-width half-maxima, indicating a reduced spectral resolution (Figure 3.15f). An even shorter interferogram

(Figure 3.15c) yields a spectrum, in which only one broad peak can be observed (Figure 3.15g). Clearly, the spectral resolution has decreased such that the frequencies ν_0 and ν_1 are not resolved anymore. Note that the fast oscillations observed in the spectra (panels f, g) are an artifact caused by the sudden stop of the interferogram at the maximum and minimum positions of Δx. As shown in Figure 3.15d,h, the inverse Fourier transformation of the boxcar functions produces a spectrum that shows the same fast oscillatory behavior, which is not related to the light source but can be considered as part of the instrument response function. The oscillations can partially be removed at the cost of a slightly reduced spectral resolution, as explained below in the following.

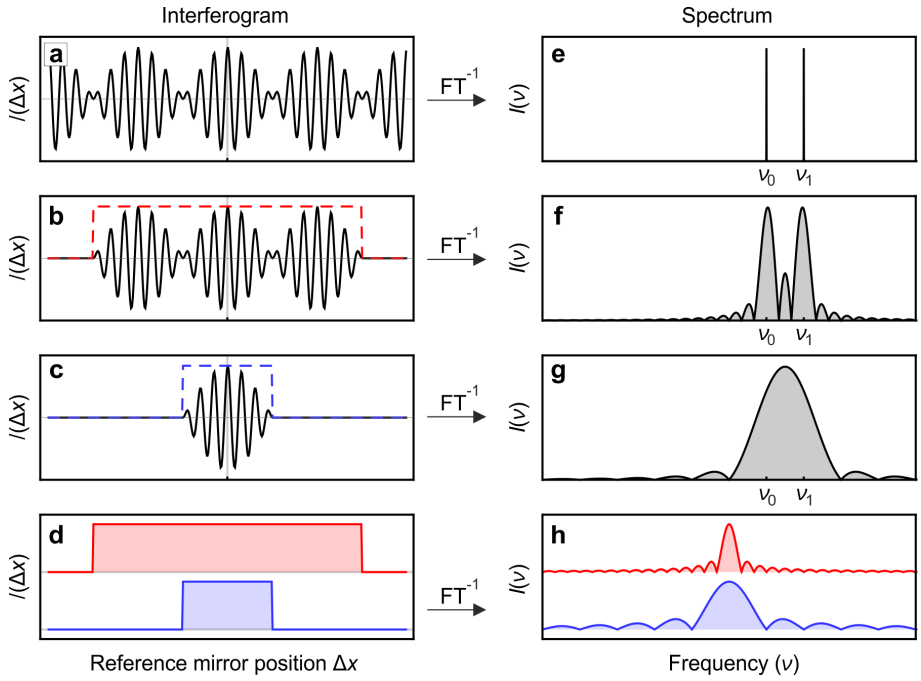

Figure 3.15: Spectral resolution as a function of interferogram length. (a-c) Interferograms of different length and (e-g) corresponding spectra obtained by inverse Fourier transformation (FT^{-1}). In all cases, the same bi-chromatic light source emitting at frequencies ν_0 and ν_1 is assumed. (d) Boxcar functions that describe the finite interferogram lengths that are used in panels b and c and (h) the corresponding spectra.

Apodization

As shown above and for convenience repeated in Figure 3.16a,e the sudden ending of an interferogram leads to an artifact which is observed as satellite oscillations on both sides of the main peaks. By multiplying the interferogram with a smooth function – the so-called apodization function or window function – the sudden ending of the interferogram is smoothed out, which effectively suppresses the fast oscillations in the spectrum (Figure 3.16b-h). The interferogram in Figure 3.16b is obtained by multiplying the original interferogram with a Blackman-Harris 3-term function[14] (blue dashed line) and the corresponding spectrum

(Figure 3.16f) is essentially artifact-free. However, the spectral resolution is decreased, because the interferogram is effectively shortened by the apodization function. In general, a trade-off between artifact-suppression and spectral resolution must be made. The nano-FTIR spectra shown in this thesis are obtained using a modified Blackman-Harris 3-term function (green dashed curve in Figure 3.16c). In this case, only the datapoints near the interferogram edges are modified, leaving most data points near the WLP unmodified. The resulting spectrum is mostly artifact-free, while maintaining a high spectral resolution (Figure 3.16g). The effect of the apodization function on the resulting spectrum can be visualized by directly plotting the inverse Fourier transformation of the apodization function (Figure 3.16h), which will be convoluted with the original spectrum.

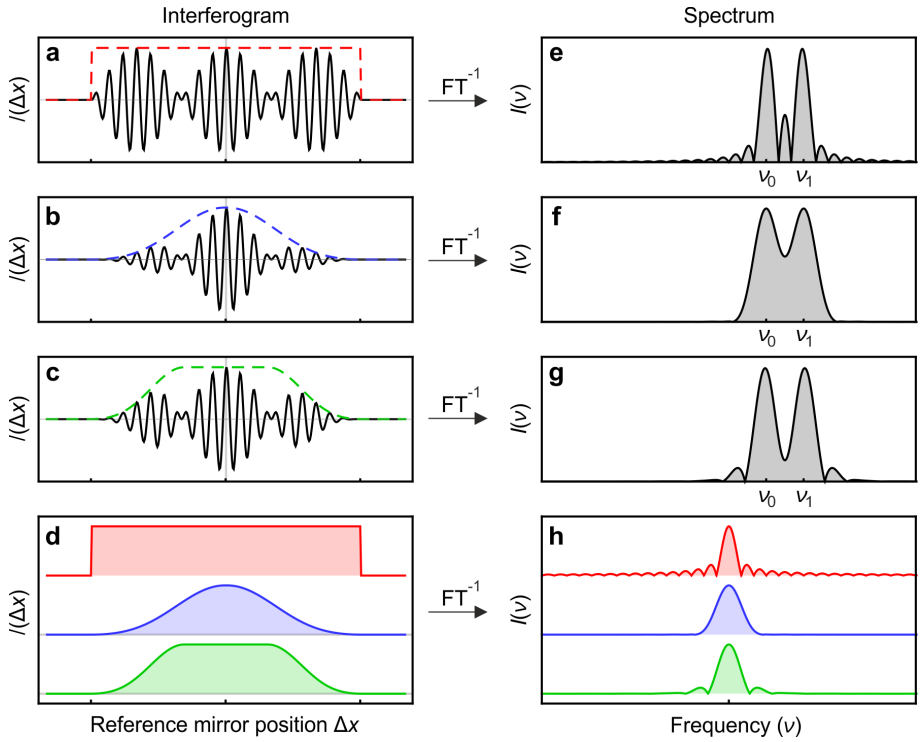

Figure 3.16: Varying apodizations of the same interferogram. (a-c) The same interferogram is multiplied by various apodization functions (dashed lines) and (e-g) corresponding spectra obtained by inverse Fourier transformation (FT^{-1}). (d) Apodization functions used in panels a-c and (h) their corresponding spectra.

Zero-filling

As explained above, the spectral resolution of a spectrum depends on the length of the interferogram that is measured. After post-processing of the data however, additional spectral details may become visible by zero-filling of the interferogram (Figure 3.17). To this end, the length of the interferogram is artificially increased by adding zeros at the interferogram ends. As an example, compare the interferogram of Figure 3.17a with that of Figure 3.17b, in which

the interferogram length is increased by a factor of 7, i.e. zero-filling with a filling-factor of 7 has been performed. The spectra with and without zero-filling are plotted together in Figure 3.17d, showing that the original data points (black) are maintained, but the spectrum of the zero-filled interferogram is evaluated at far more frequencies (red), thus improving the visibility of the underlying spectral features. Note that zero-filling only reveals additional spectral details by showing more data points of a spectrum but does not increase the experimentally obtained spectral resolution.

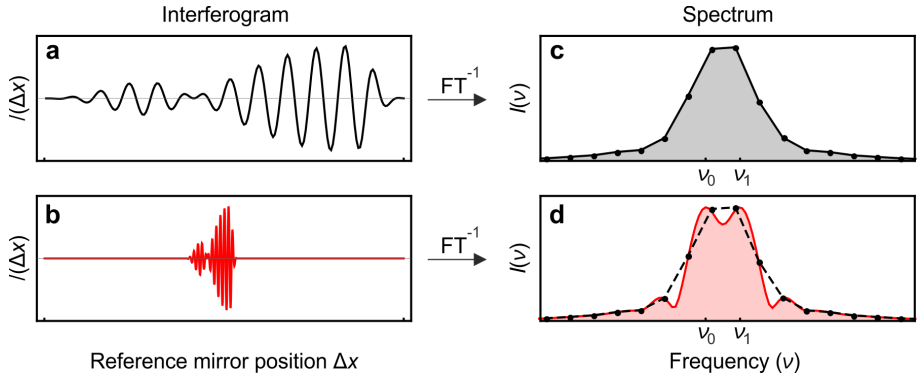

Figure 3.17: Zero-filling of the interferogram increases the apparent spectral resolution. (a) Interferogram without zero-filling and (b) with zero-filling using a fill-factor of 7. (c-d) Corresponding spectra obtained by inverse Fourier transformation (FT^{-1}). The dashed line in panel d shows the same data points as panel c.

3.6 Experimental setup for s-SNOM and nano-FTIR

In nano-FTIR spectroscopy, infrared light emitted by a broadband laser source is focussed onto the metallized tip of an AFM tip, which acts as optical antenna and nano-focusses the light onto the sample (chapter 3.1). The tip-scattered light is modified by the near-field interaction between tip and sample (chapters 3.2 and 3.4) and analysed in a Michelson interferometer setup yielding frequency-resolved infrared spectra analogous to FTIR spectroscopy (chapter 3.5). In order to isolate the pure near-field signal from unwanted background signals in the tip-scattered light, the AFM is operated in tapping-mode (explained below), which modulates the near-field interaction between tip and sample (and thus the tip-scattered light) at the oscillation frequency Ω of the AFM tip. By demodulating the detected signal at higher harmonics $n\Omega$, the background-free near-field signal is obtained (chapter 3.3). In the following, the employed nano-FTIR setup is explained, highlighting also that nano-FTIR spectroscopy yields complex-valued (amplitude and phase) spectra, whereas conventional FTIR spectroscopy typically only yields amplitude spectra.

Tapping-mode atomic force microscopy (AFM)

Atomic force microscopy (AFM) is a scanning-probe microscopy technique, in which a sharp tip (the "probe") is scanned across the surface of a sample, while monitoring the mechanical forces between probe and sample as a function of the probe position.[74,75] By using an AFM tip with a nanoscale-sized tip radius (typically 10 - 50 nm for metallized tips or even smaller for silicon tips), nanoscale-resolved images of the sample are routinely obtained. To detect the mechanical forces between the probe and sample, the tip is attached to a flexible cantilever, which deflects up and down when the mechanical force between the probe and sample varies. This deflection (or bending) of the cantilever is measured by reflecting a laser beam at the backside of the cantilever and detecting the reflected light using a four-quadrant photodiode (Figure 3.18a).

When the AFM is operated in tapping mode, the probe tip is oscillated vertically near the cantilever's mechanical resonance frequency Ω, with typical oscillation amplitudes $A \approx 10$ nm. During every oscillation cycle, the tip briefly contacts the sample (i.e. the tip "taps" onto the sample), which slightly reduces the oscillation amplitude compared to the free oscillation amplitude when no sample is present. As a result, the oscillation amplitude is sensitive to the forces between the tip and sample, which varies for example due to changes in the sample topography (Figure 3.18b). Practically, a closed feedback-loop is employed to keep the oscillation amplitude (and thus the force) constant while scanning the sample surface. As a result, when the oscillation amplitude decreases, the sample is moved away from the tip – or when the oscillation amplitude increases, the sample is moved closer to the tip (Figure 3.18c). By monitoring the vertical position of the sample as a function of (lateral) tip position, a topography image of the sample is obtained.

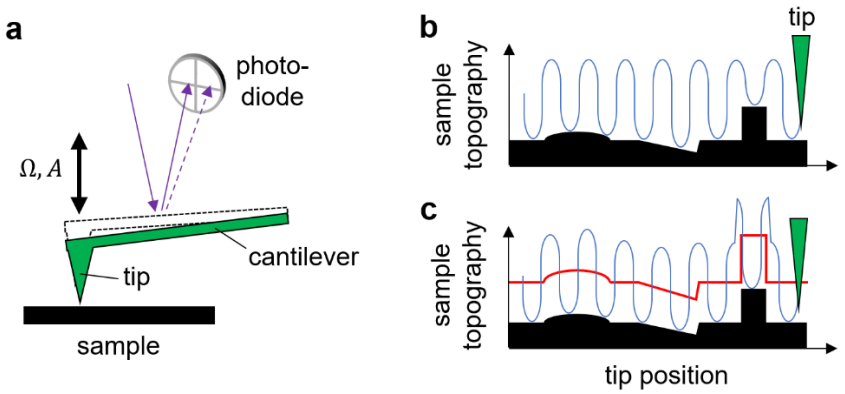

Figure 3.18: Illustration of tapping-mode AFM. (a) Side view of a sample being contacted (tapping-mode) by the sharp tip of an AFM probe, which is oscillating vertically with an amplitude *A* at the mechanical resonance frequency Ω of a flexible cantilever. By focusing laser light at the backside of the cantilever and measuring the reflected light using a four-quadrant photodiode (purple arrows), the cantilever movement is monitored. (b) The sample topography (black) modifies the tip oscillation amplitude (illustrated by blue line). (c) By continuously adjusting the vertical sample position (red line) using a closed feedback-loop, the tip oscillation amplitude is kept constant while scanning the sample surface.

Note that the vertical oscillation of the tip introduces a modulation to the optical near-field interaction between the tip and sample. In combination with higher harmonic demodulation of the tip-scattered light, this allows for suppression of unwanted background scattering, as explained above (chapter 3.3).

Optical setup for s-SNOM and nano-FTIR

The setup used in this thesis for infrared near-field spectroscopy is based on a commercial s-SNOM (neaSNOM from neaspec GmbH), which employs a tunable quantum cascade laser (QCL, Daylight Solutions) for s-SNOM imaging and a broadband infrared laser continuum (generated by difference frequency generation, DFG) for nano-FTIR spectroscopy (Figure 3.19). The laser beams are focused using a parabolic mirror (PM) onto the probing tip of an atomic force microscope (AFM). In this work, standard platinum-coated AFM tip (NCPt arrow tip, Nanoworld) are used with an apex radius of about 30 nm. The light backscattered by the tip is collected with the same parabolic mirror and detected in one of two asymmetric Michelson interferometer setups – one for s-SNOM imaging and one for nano-FTIR spectroscopy (left and right hand sides of Figure 3.19 respectively). In an *asymmetric* Michelson interferometer, the sample is placed in one of the interferometer arms (below the AFM tip), which allows for the measurement of amplitude *and* phase of the tip-scattered light[15,16,52,67], in contrast to conventional (far-field) FTIR experiments where typically only amplitude signals are obtained. The intensity of the tip-scattered light is detected and demodulated at higher harmonics $n\Omega$ of the tip tapping frequency Ω (here $\Omega \approx 250$ kHz), using an infrared detector and digital lock-in amplifier. In the following, the complex-valued spectral scattering coefficient obtained at the nth demodulation order is named $\sigma_n = s_n e^{i\varphi_n}$, which can be separated into near-field (nano-FTIR) amplitude s_n and phase φ_n.

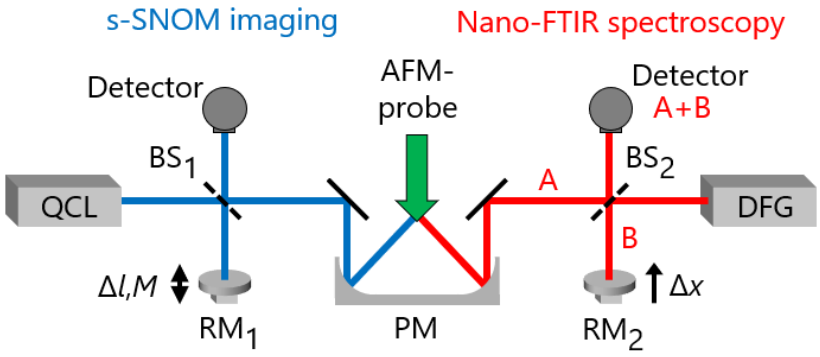

Figure 3.19: Illustration of the s-SNOM and nano-FTIR setup. Top view of a quantum cascade laser (QCL) being used for s-SNOM imaging and an infrared laser continuum based on difference frequency generation (DFG) being used for nano-FTIR spectroscopy. A parabolic mirror (PM) is used for focusing the laser radiation onto the tip apex of a metallized AFM probe, which is in contact (tapping mode) with the sample (not shown). After collection of the tip-scattered light with the same PM, two independent asymmetric Michelson interferometers are used for detection, each interferometer comprising a beam splitter (BS), moveable reference mirror (RM) and infrared detector. In nano-FTIR spectroscopy, the reference mirror RM_2 is linearly translated by a distance Δx along the beam axis. In s-SNOM imaging, the reference mirror RM_1 is modulated at a frequency M with an oscillation amplitude Δl.

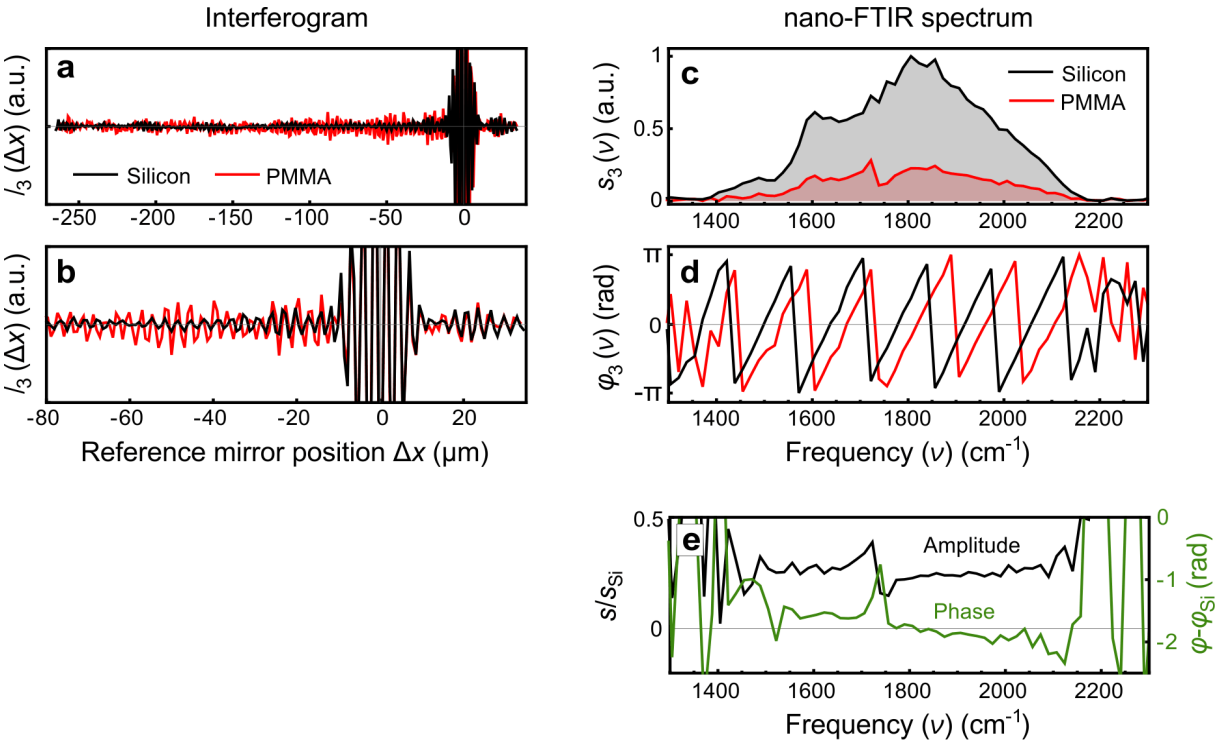

Figure 3.20: Normalization of experimental nano-FTIR spectra. (a) Interferograms measured on a silicon sample (black) and a PMMA sample (red), showing the demodulated detector signal I as a function of reference mirror position Δx. (b) Zoom-in of panel a. (c) Nano-FTIR amplitude s_3 and (d) phase φ_3 spectra obtained by apodization and inverse Fourier transformation of the interferograms shown in panel a. (e) Nano-FTIR amplitude an phase spectra of PMMA, normalized to that of silicon.

In nano-FTIR spectroscopy (right-hand side of Figure 3.19), the intensity of the tip-scattered light is demodulated and recorded as a function of the path length difference Δx between the interferometer arms by linearly translating the reference mirror (RM_2 in Figure 3.19) along the beam axis, yielding nano-FTIR interferograms. Figure 3.20a,b exemplary show the interferograms experimentally obtained on a silicon sample (black) and a PMMA sample (red) and Figure 3.20c,d show the corresponding nano-FTIR amplitude s_3 and phase φ_3 spectra obtained by inverse Fourier transformation of the interferograms. Note that nano-FTIR interferograms are asymmetric around the WLP, which is best seen in the interferogram recorded on PMMA (red curve in Figure 3.20b). The excitation of molecular vibrations in PMMA and their subsequent free induction decay introduces a phase-lag of the sample-beam (but not of the reference-beam), which modifies the interference only on one side of the WLP and thereby enables the detection of both amplitude and phase spectra.[15,16,52,67] In a symmetric Michelson interferometer setup (as used in far-field FTIR spectroscopy, chapter 3.5) this phase-lag would be contained in the beams of both interferometer arms and thus cancel out in the interference – preventing the detection of phase spectra.

For a quantitative analysis of the nano-FTIR spectra, all spectra must be normalized to the nano-FTIR spectrum of a reference sample with known optical properties via $\sigma_n^{\text{norm}} = \sigma_n(\text{sample}) / \sigma_n(\text{ref})$, as explained in the following. As the silicon sample can be considered highly reflective for near fields and spectrally flat in the mid-IR spectral range, the nano-FTIR spectrum obtained on silicon essentially characterizes the spectral instrument response function (black curves in Figure 3.20c,d). In order to remove the instrument characteristics and thus to obtain the pure nano-FTIR spectrum of the PMMA sample, the nano-FTIR spectrum of silicon is exemplarily used as a reference for signal normalization. The normalized nano-FTIR amplitude and phase spectrum of PMMA are thus given by $s_n(\text{PMMA}) / s_n(\text{Si})$ and $\varphi_n(\text{PMMA}) - \varphi_n(\text{Si})$ respectively (Figure 3.20e). The normalized spectra clearly reveal the presence of PMMA, which can be identified in the nano-FTIR phase spectrum (green) via a peak around 1740 cm^{-1} and in the nano-FTIR amplitude spectrum (black) via the dispersive line shape, which correspond to the C=O vibrational mode of PMMA.[76]

Note that the tip modulation and higher harmonic signal demodulation described in chapter 3.3 removes only an *additive* background. In general, the interference of background-scattering and near-field scattering also produces a *multiplicative* background. In nano-FTIR spectroscopy, however, the multiplicative background contributes only as a complex-valued offset to the interferogram, and thus (after Fourier transformation of the interferogram) the nano-FTIR spectra are free of multiplicative background for spectral frequencies $\nu > 0$.[40]

In s-SNOM imaging, the multiplicative background is commonly removed by using a pseudo-heterodyne interferometric detection scheme[12,13] (left-hand side of Figure 3.19). To this end, the position of the reference mirror RM_1 is oscillating along the beam axis with an oscillation amplitude Δl and oscillation frequency M (typically $M \approx 300$ Hz). The phase-modulation of the reference beam yields additional side bands at frequencies $n\Omega \pm mM$ with m being an integer value.[12,13] Demodulation of the tip-scattered light at one or several side bands with $m \neq 0$ yields a near-field signal free of multiplicative background (and as a reminder: contributions of additive background scattering are suppressed by using higher harmonic demodulation at $n > 2$). Furthermore, amplitude and phase information are separated and obtained simultaneously by adjusting the reference mirror oscillation amplitude to $\Delta l \approx 0.21\lambda$ and considering at least one odd and one even side band.[12,13] Experimentally, this condition is fulfilled by linearly sweeping the reference mirror position along the beam axis, while adjusting Δl, such that the optical amplitude is not affected by the linear phase sweep.

4 Substrate-enhanced IR Nanospectroscopy of Molecular Vibrations

Infrared nanospectroscopy based on Fourier transform infrared near-field spectroscopy (nano-FTIR) is an emerging nanoanalytical tool with large application potential for label-free mapping and identification of organic and inorganic materials with nanoscale spatial resolution. However, the detection of thin molecular layers and nanostructures on standard substrates is still challenged by weak signals. This chapter demonstrates a significant enhancement of nano-FTIR signals of a thin organic layer by exploiting polariton-resonant tip-substrate coupling and surface polariton illumination of the probing tip. When the molecular vibration matches the tip-substrate resonance, nearly one order of magnitude signal enhancement is achieved on a phonon-polaritonic quartz (c-SiO_2) substrate, as compared to nano-FTIR spectra obtained on metal (Au) substrates, and up to two orders of magnitude when compared to the standard infrared spectroscopy substrate CaF_2. The results will be of critical importance for boosting nano-FTIR spectroscopy towards the routine detection of monolayers, single molecules and for other challenging experiments with weak signals such as nanospectroscopy of subsurface organic material as presented in chapter 5.

4.1 Introduction

Scattering-type scanning near-field optical microscopy (s-SNOM)[2] and Fourier transform infrared nanospectroscopy (nano-FTIR)[15,17,77] have been widely applied in numerous studies of both fundamental and applied aspects, including nano-FTIR chemical nanoidentification of organic and inorganic samples[15,17,77,78], contact-less s-SNOM conductivity and phase transition mapping[17,79–83] and secondary structure mapping of protein complexes[84]. However, when applied to very thin layers of weakly absorbing substances, particularly monolayers or individual molecular complexes, s-SNOM and particularly nano-FTIR signals are often at or below the detection limit[84–86].

To enhance the infrared near-field signals in s-SNOM and nano-FTIR, the sample layers are typically deposited on strongly reflecting substrates such as silicon or gold[2,15,51,77,78,85–89]. The signal enhancement can be explained by the electromagnetic field concentration in the gap between tip and substrate, similar to tip-enhanced Raman spectroscopy (TERS) in gap mode configuration[90]. However, despite various recent developments and rapid diffusion of the nano-FTIR technique, only few studies discuss in detail the signal enhancement by tip-substrate coupling and its potential further exploitation beyond standard Si and Au substrates. Recently, spectroscopic s-SNOM imaging of molecules deposited on infrared-resonant metal antennas has demonstrated an enhancement of the vibrational signature[91–93]. However, this approach requires the fabrication of antennas and limits the enhancement to the relatively small areas where electromagnetic hot spots are formed. The predicted enhancement of s-SNOM and

nano-FTIR spectroscopic signatures of weak molecular vibrations via tip-induced polariton excitation in flat substrates[51] has not been demonstrated so far experimentally.

In this chapter it is studied how the substrate influences nano-FTIR molecular vibrational spectroscopic features. First experimental evidence is given that spectroscopic features can be enhanced by one to two orders of magnitude when placing a molecular layer on flat polaritonic substrates instead of standard IR substrates such as CaF_2, provided that the molecular vibration matches the tip-substrate resonance. Particularly, 13 nm-thin layers of poly(ethylene oxide) (PEO) molecules are studied to demonstrate experimentally that a significant signal enhancement - beyond that provided by flat gold substrates - can be achieved due to polariton-resonant near-field coupling between tip and substrate, here a quartz crystal featuring a tip-induced phonon polariton resonance matching the molecular vibration of PEO. An even higher signal enhancement can be achieved by additional illumination of the tip via surface phonon polaritons on the quartz crystal that are launched at discontinuities on the sample surface.

This chapter is an extended version of the *Nano Letters* publication[30], and provides a more detailed explanation of the tip-induced phonon polariton resonance. I clarify that the results were jointly obtained, and that the contribution of the first author Marta Autore is equal to my contribution.

4.2 Methods

Experimental setup

A detailed explanation of the experimental s-SNOM and nano-FTIR setup is given in chapter 3.6. For convenience, a short description of the setup is given in Figure 4.1.

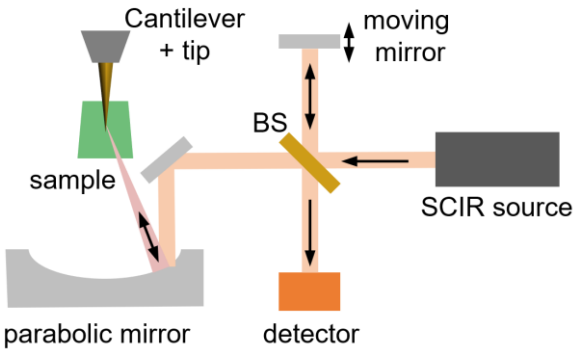

Figure 4.1. Experimental setup for nano-FTIR spectroscopy. A metallized AFM tip is in contact (tapping mode) with the sample. The tip is illuminated by broadband mid-infrared supercontinuum (SCIR) laser radiation, which is focused to the tip apex using a parabolic mirror. The tip-scattered light is collected by the same parabolic mirror and detected in an interferometer which comprises a beam splitter (BS), a linearly moving mirror and the detector. For fixed tip-sample positions, the detector signal is recorded as a function of the moving mirror position, yielding an interferogram from which a nano-FTIR spectrum is obtained by Fourier transformation.

Sample Preparation

The studied samples consist of 13 nm-thick poly(ethylene oxide) layers on top of CaF_2, Si, Au and c-SiO_2 substrates. To that end, a 0.25% solution of PEO in acetonitrile was spin-coated at 150 rps during 2 minutes on each substrate.

Calculations

All calculated nano-FTIR spectra shown in this chapter were calculated using the finite dipole model (FDM) for layered samples[48,54], as explained in more detail in chapter 3.4.4. Briefly, the FDM describes the nano-FTIR probing tip as a prolate spheroid with apex radius R and a major half-axis length L. The multilayer sample is described by the permittivities ϵ of all layers. Here the model parameters are R = 25 nm, L = 150 nm, g = 0.6+i0.2 and a tapping amplitude A = 37 nm (the latter corresponding to the experimental value). The factor g is found empirically and describes which portion of charge induced in the tip is relevant for near-field interaction[48].

4.3 Standard IR substrates

Figure 4.2 panels a and c show the measured amplitude and phase spectra of PEO on two standard IR-substrates, Au and CaF_2, respectively. For PEO on CaF_2 (red curves) we observe a near-zero amplitude signal with a barely visible spectral feature at around 1105 cm^{-1}, which can be attributed to the symmetric and asymmetric stretching of the C-O-C group of PEO[94]. It is better seen in the phase spectrum, although the signal-to-noise-ratio (S/N) is rather low. Strikingly, for PEO on Au we obtain a typical dispersive-like feature in the amplitude spectrum (black curve in Figure 4.2a), where the signal difference between maximum and minimum is a factor of about 20 larger than for PEO on CaF_2. Further, the phase spectrum (black curve in Figure 4.2c) exhibits a clear peak with a significantly improved S/N ratio as compared to the PEO spectrum on CaF_2.

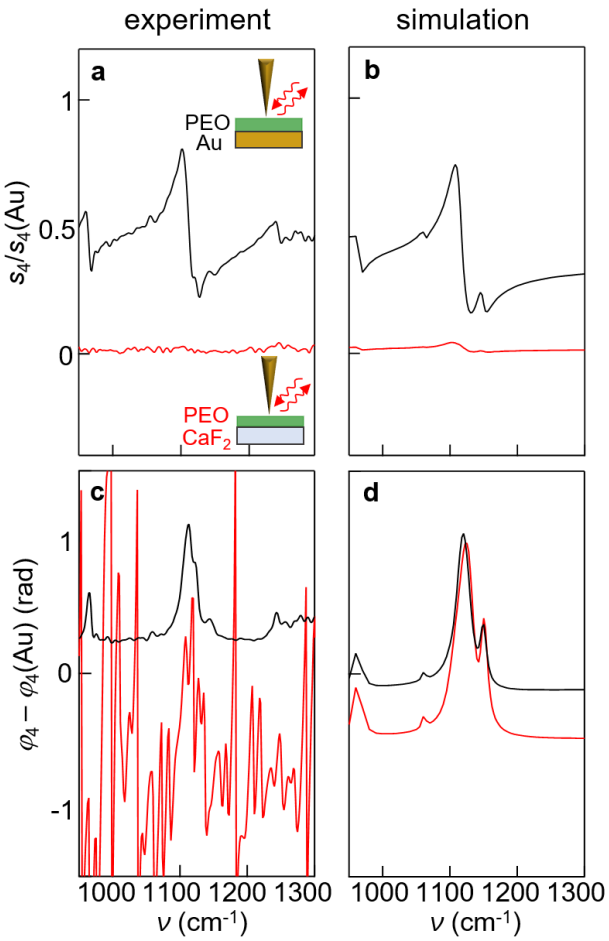

Figure 4.2. nano-FTIR spectroscopy of 13 nm thick PEO layers on CaF_2 and Au substrates. (a,c) Experimental amplitude (a) and phase (c) spectra of 13 nm-thick PEO on Au (black curve) and CaF_2 substrate (red curve). (b,d) Calculated spectra, analogous to panels a,c. All spectra are normalized to the nano-FTIR spectrum of a bare Au sample.

We corroborate the experimental nano-FTIR spectra and the substrate-induced signal enhancement with calculations using the multilayer finite dipole model, in which the tip is described as an elongated dipole[48] that interacts with the several sample layers[54] that are characterized by their dielectric function. In this model, the tip-scattered field is given by

$$E_{scat} \propto (1+r)^2 \alpha_{eff} \tag{4.1}$$

where α_{eff} is the effective polarizability of the tip that accounts for the near-field interaction between the tip and the layered sample. r is the far-field reflection coefficient of the substrate (for calculation details see Methods). The calculated amplitude and phase spectra are shown in Figure 4.2 panels b and d. We observe a remarkable agreement between experiment and calculations, particularly regarding the strong enhancement of the vibrational signature in the amplitude spectrum of the PEO layer on the Au substrate as compared to PEO on CaF_2. This signal amplitude enhancement is caused by (*i*) the large far-field reflection coefficient of Au (r = 1) as compared to CaF_2 (r = -0.06), which is the Fresnel reflection coefficient obtained for a p-polarized wave at 60 degree incidence normal to the sample surface and a refractive index[95] n_{CaF2} = 1.34 which leads to a more efficient tip illumination and collection of the tip-scattered field, and (*ii*) the increased near-field interaction between tip and gold substrate yielding to a stronger local field enhancement at the tip apex[51,87]. On the other hand, the calculated phase spectra indicate that the phase contrast (peak height) of PEO on CaF_2 is slightly larger than that of PEO on Au. However, because of the much lower signal on CaF_2 (see amplitude spectra), the experimental S/N ratio is too low for this effect to be beneficial in a practical way.

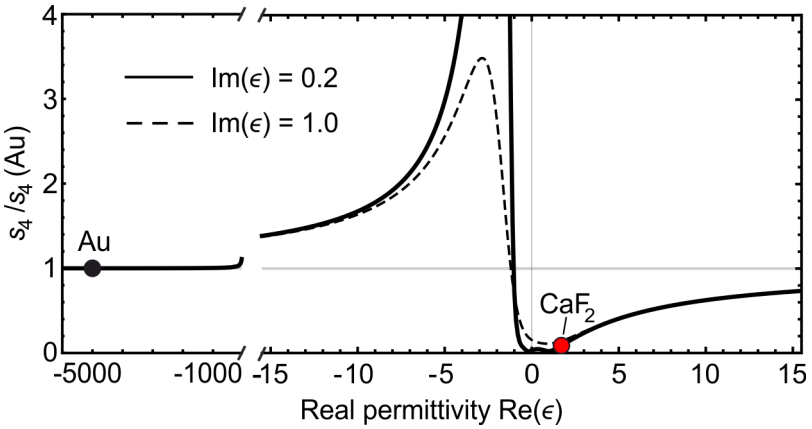

Figure 4.3: Nano-FTIR amplitude as function of substrate permittivity. Calculated normalized nano-FTIR amplitude s_4/s_4(Au) for semi-infinite substrates with varying permittivity Re(ϵ) and fixed Im(ϵ) = 0.2 (solid curve), respectively Im(ϵ) = 1.0 (dashed curve). Symbols highlight the results for substrates made of gold (ϵ_{Au} = -5000+i1000) and calcium fluoride (ϵ_{CaF2} = 1.8). For calculation details see Methods section.

To illustrate the increased near-field interaction between tip and gold substrate, and to generalize the results to other substrate materials, Figure 4.3 shows calculated nano-FTIR amplitude signals s_4/s_4(Au) as a function of substrate permittivity ϵ and normalized to the amplitude signals obtained on a gold substrate (black symbol). In good agreement with Figure 4.2, the amplitude signal obtained on a CaF2 substrate (red symbol) is significantly weaker than that of a gold substrate. Strikingly, the calculated nano-FTIR amplitude increases far beyond the level of a gold substrate when the substrate permittivity is slightly negative. We recall that in most models for tip-sample near-field interaction the effective polarizability of the tip, α_{eff}, is a function of the near-field (quasi-electrostatic) reflection coefficient β, which for a semi-infinite surface in vacuum is given by

$$\beta = \frac{(\epsilon-1)}{(\epsilon+1)} \tag{4.2}$$

where ϵ is the dielectric function of the sample[2,15,50,51]. The effective polarizability, and thus the tip-scattered field, exhibit a resonance near $\epsilon \approx -1$ (Figure 4.3) owing to the divergence of β, which corresponds to the excitation of localized surface polaritons by the concentrated near fields at the tip apex (e.g. surface plasmon polaritons in metals and doped semiconductors, or surface phonon polaritons in polar crystals[50]). In Ref. 51 we predicted that this resonant near-field interaction could enhance the infrared spectral contrast of molecular vibrations of thin layers in the tip-substrate gap. Up to date, however, this effect has not been demonstrated experimentally. In the following we thus explore the possibility of further increasing the nano-FTIR signals of PEO by resonant tip-substrate coupling.

4.4 Phonon polariton-resonant substrate

For a first experimental demonstration of surface-polariton enhanced nano-FTIR spectroscopy of molecular vibrations, we selected crystalline quartz (c-SiO_2) substrates, an exemplary polar crystal supporting surface phonon polaritons[96,97] near the molecular vibrational resonance of PEO. The measured far-field reflectivity spectrum of c-SiO_2 is shown in Figure 4.4a. It exhibits a typical *Reststrahlen band*, where $R \approx 1$. Within this band (between 1070 and 1220 cm^{-1}), the real part of the dielectric function, ϵ_1, is negative, which in case of c-SiO_2 is a consequence of multiple phonon excitations. By fitting the far-field spectrum with Fresnel equations we obtained the complex-valued dielectric function of c-SiO_2, which is plotted in Figure 4.4b. Around 1150 cm^{-1} we find $\epsilon_{1,\text{c-SiO2}} \simeq -1$, such that the condition for a tip-induced polariton resonance in the substrate is fulfilled near the PEO molecular vibrational resonance at 1105 cm^{-1} (marked by vertical dashed line and defined by the maximum of $\epsilon_{2,\text{PEO}}$) that can be clearly recognized in the dielectric function of PEO (Figure 4.4c). Indeed, the nano-FTIR spectrum of a clean quartz surface (normalized to the spectrum of bare gold) reveals the expected resonance[96] (blue curve in Figure 4.5d) where the normalized amplitude signal s_4/s_4(Au) exhibits

values that are up to 3.5 (i.e. 3.5 times higher than that of the gold reference surface). The multiple-peak structure of the spectrum (maxima at 1135 and 1170 cm^{-1}) can be ascribed to the presence of several phonon resonances contributing to the Reststrahlen band of quartz[96].

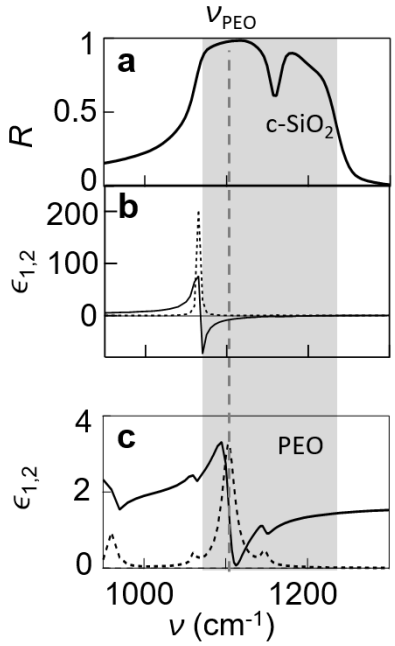

Figure 4.4. Optical properties of the quartz substrate and of PEO molecules. (a) Reflectivity spectra of bare quartz. (b) Real (black curve) and imaginary (dashed black curve) part of the dielectric function obtained by fitting the Drude-Lorentz model to the quartz reflection spectrum using the RefFIT software[98]. (c) Real (black curve) and imaginary (dashed black curve) part of the dielectric function of PEO, obtained by fitting far-field transmission spectra of 500 nm thick PEO layers on CaF_2 by the Drude-Lorentz model using the RefFIT software. The gray shaded area indicates the Reststrahlen band of quartz and the vertical dashed line indicates the resonance frequency ν_{PEO} of the PEO vibration.

To explore the effect of tip-quartz coupling on the nano-FTIR spectra of thin PEO layers, we evaporated 30 nm of Au onto one half of the quartz substrate and spin-coated PEO as described above. That way we obtained a PEO layer on gold and on quartz within one sample, which allows for a reliable comparison of the two situations under the same experimental conditions (same tip, as well as same microscope settings and adjustment).

We obtained self-assembled islands of PEO on top of the gold and quartz surfaces with a rather homogeneous height of 13 nm and an average diameter of about 150 nm. The PEO areas are clearly visible in the AFM image (1x0.5 μm^2) shown in Figure 4.5b and in the s-SNOM image of the same area taken at 1114 cm^{-1} (amplitude image, s_4, Figure 4.5c). The formation of islands offers the advantage that nano-FTIR spectra of adjacent regions of PEO on c-SiO_2 and bare c-SiO_2, as well as of PEO on Au and bare Au, can be measured under the same experimental conditions, thus allowing for a reliable comparison of spectra. Note that in both data analysis and simulations we do not consider the island-like morphology of the PEO layer. The measurements were done in the center of larger islands, which have a diameter of typically

100-200 nm, and thus can be considered in first approximation as an extended layer compared to the tip of about 25 nm apex radius and corresponding spatial resolution.

In Figure 4.5d we compare nano-FTIR spectra of PEO on quartz with nano-FTIR spectra of pure quartz. We observe a strong dip in the PEO spectrum at the position close to the peak maximum of the pure quartz spectrum, which we attribute to the vibrational resonance of PEO (marked by dashed line). This finding strongly resembles the features found in surface- and antenna-enhanced infrared spectra (SEIRA) of molecules on resonant plasmonic antennas, where Fano interference between the molecular vibration and plasmons occurs[99,100]. Analogously, we can explain the observation in our nano-FTIR spectra by Fano interference between the molecular vibration and the tip-induced phonon-polariton in the substrate, similar to phononic SEIRA[101].

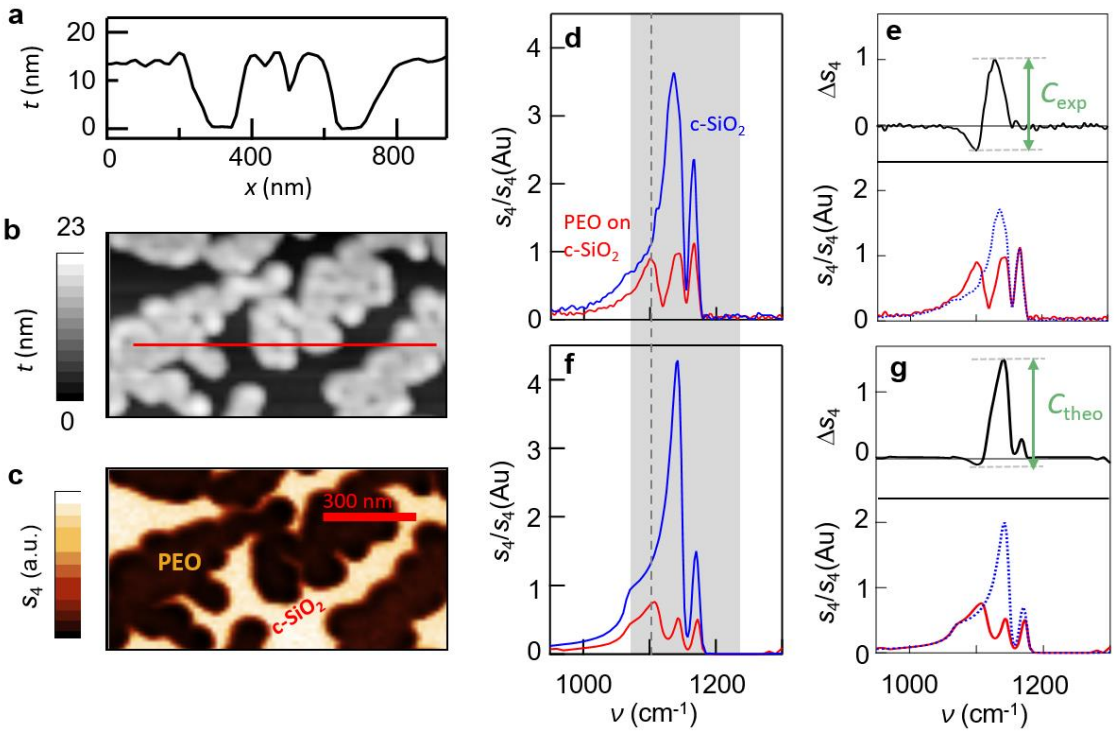

Figure 4.5. nano-FTIR spectroscopy on a resonant quartz substrate. (a) Topography line profile along the red line in panel b). (b) Topography and (c) s-SNOM image recorded at ν = 1114 cm^{-1} (shown for illustrative purposes only) of a 1x0.5 µm^2 c-SiO_2 substrate with spin-coated PEO on top, the latter forming nanoscale islands. (d) Experimental and (f) calculated nano-FTIR amplitude spectra (4th harmonics, normalized to gold spectrum) of quartz (blue) and PEO on quartz (red). Panels (e) and (g) show the normalized quartz spectra (blue dashed curves) used for calculating the maximum spectral contrast C (defined as difference between maximum and minimum of Δs_4 shown by black curves) of the polariton-enhanced vibrational feature of PEO on quartz for experimental and calculated data, respectively.

We measure the magnitude of the polariton-enhanced molecular vibrational signature analogously to what is conventionally done in SEIRA measurements. We first subtract the spectrum of PEO on quartz from the spectrum of bare quartz and then calculate the difference between maximum and minimum of the resulting spectral feature (as illustrated in Figure 4.5e). To apply this procedure, we need to take into account the reduced tip-substrate coupling

caused by the increased tip-substrate distance when the tip is on top of PEO. To that end, we normalized the spectrum of quartz, s_4(c-SiO_2)/s_4(Au), in such a way that the signal between 980-1050 cm^{-1} (assumed to be barley affected by the PEO vibration because of its rather large spectral distance to the phonon resonance) matches with the one of the spectrum of PEO on quartz, s_4(PEO on c-SiO_2)/s_4(Au). We denote the resulting spectrum $\bar{s_4}$(c-SiO_2)/s_4(Au) and show it as blue dashed line in Figure 4.5e. With $\Delta s_4 = \bar{s_4}$(c-SiO_2)/s_4(Au)-s_4(PEO on c-SiO_2)/s_4(Au) we finally obtain the polariton-enhanced vibrational spectral contrast (black curve in Figure 4.5e). Although our normalization step does not take into account the spectral shifts caused by the increased tip-substrate distance[102,103] we can reliably determine the enhancement of C on c-SiO_2 as compared to Au (for a comparison of different normalization procedures, see Appendix 6.1).

The spectral contrast Δs_4 exhibits an asymmetric shape, neither resembling the amplitude nor the phase spectrum of PEO on CaF_2 or Au substrates. This observation is typical for a Fano-type interaction between a broad excitation (the phonon polaritons in this case) and a narrow mode (the PEO vibration), where the spectral shape depends on both the interaction strength and on the spectral overlap between the two modes[99]. Most importantly, the spectral contrast Δs_4 is larger than the one obtained for PEO on Au, as we will highlight and quantify below. Before, we corroborate the experimental results by calculations using the multilayer finite dipole model described above. As shown in Figure 4.5 panels f,g, the spectral behavior is well reproduced and the enhancement of the vibrational contrast is confirmed. We note that the near-field phase contrast Δs_4 (data not shown) is barely enhanced. For that reason, we analyze in this work essentially near-field amplitude spectra.

In the following, we compare quantitatively the enhancement factors of the PEO vibrational signature in the case of non-resonant substrates with different reflection coefficients (CaF_2, Si, Au) and resonant c-SiO_2. The results are summarized in Figure 4.6b. The three top curves show the amplitude spectra of PEO on CaF_2 (green), Si (orange) and Au (black). Taking the maximum spectral contrast of the PEO on the Au substrate (C = 0.46) as a reference, we find a reduction of C to 54% for PEO on Si and to 7% for the CaF_2 substrate. This finding can be explained by (*i*) the reduced reflection coefficient r of Si and CaF_2 compared to Au (r_{Si} = 0.28, r_{CaF2} = -0.06, r_{Au} = 1)[95] which reduces both the illumination and scattering of the tip via the substrate (top illustration of Figure 4.6a), and (*ii*) the reduced near-field interaction between tip and substrate owing the smaller near-field reflection coefficient β (Equation (4.2)) of Si and CaF_2[23]. When PEO is placed on c-SiO_2 we achieve a 300% increase (compared to Au substrate) of C, which is determined according to the procedure described above from the red spectrum shown as inset. We can explain this significant enhancement compared to Au only by the enhanced near-field interaction (described by α_{eff}) between tip and substrate due to tip-induced phonon polariton excitation, as tip illumination and tip scattering via the substrate reaches is maximum for the Au surface (we stress that r is the far-field Fresnel reflection coefficient of the substrate, which cannot exeed r = 1). Actually, the tip illumination and tip scattering via the quartz surface reduces the signal amplitude by $Abs[(1+r_{c\text{-}SiO2})^2/(1+r_{Au})^2] \approx 50\%$, which is, however, more than compensated by the enhanced near-field interaction. Note that a native oxide is present on the Si substrate, with a phonon-resonance at the position of the PEO vibrational mode.

However, this oxide layer is typically as thin as a few nanometer. Although it can be observed in s-SNOM, it provides a rather small and thus negligible contribution to the near-field interaction between tip and silicon substrate[69].

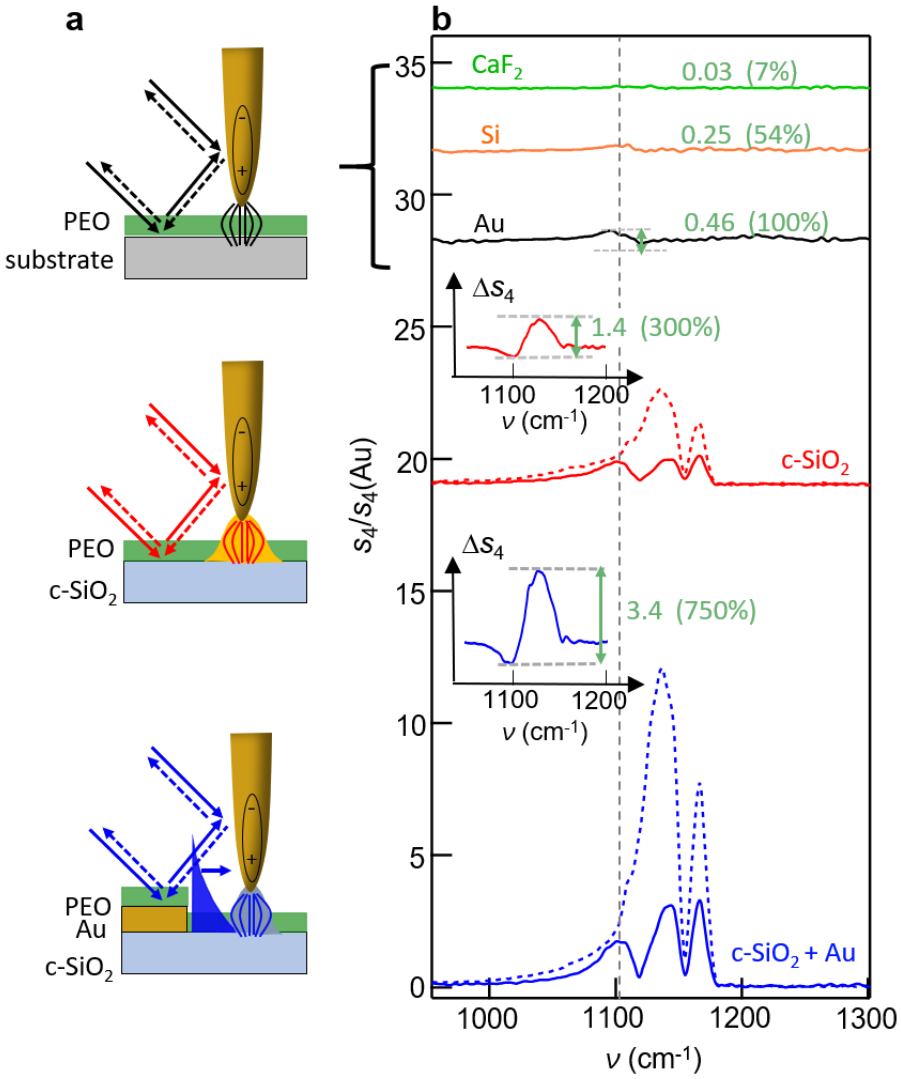

Figure 4.6. Comparison of different substrates for nano-FTIR spectroscopy of PEO. (a) Sketches of the different mechanisms contributing to the tip illumination in the performed experiments. From top to bottom: indirect illumination of the tip via the substrate (top), additional resonant tip-substrate coupling due to tip-induced phonon polariton excitation in the substrate (middle), and additional tip illumination via propagating surface phonon polaritons launched by the edge of a gold film (bottom). (b) From top to bottom: nano-FTIR amplitude spectra of PEO on CaF_2, Si, Au and quartz (c-SiO_2) substrates (solid curves). The very bottom spectrum was obtained in 1 µm distance to the edge of an extended Au film launching surface phonon polaritons. Dotted lines show spectra without PEO. For better visibility of the vibrational features, the spectra on the different substrates are offset. Inset: The red and blue curves show the calculated spectral contrast Δs_4. Note that the scale of the vertical axes Δs_4 and s_4/s_4(Au) are the same.

4.5 Additional tip illumination by propagating surface phonon-polaritons

We finally explore the possibility of further boosting the enhancement of the vibrational contrast by exploiting additional tip illumination via propagating surface phonon polaritons. To that end, we deposited an extended gold film on quartz. The gold edge serves as a surface phonon polariton (SPhP) launcher[104] (see sketch in Figure 4.6a, bottom). When the tip is placed close to the gold edge, i.e. within the propagation length of the SPhPs, the polariton field provides an additional (coherent) tip illumination, thus boosting the near-field enhancement at the tip apex. The experimental verification of this concept is shown by the spectra (blue) of Figure 4.6b. The dashed blue curve represents the spectrum of quartz taken at 1 µm distance from the gold edge. The signal amplitude is up to 12 times higher than the signal on gold, and approximately 3 times higher than the signal of quartz far from the Au edge. We explain this significant additional signal enhancement by (*i*) the high reflection coefficient *r* of Au (which – as explained above – increases the signal amplitude by a factor of 2 compared to quartz) and (*ii*) the additional tip illumination through the SPhP (both aspects illustrated in the sketch of Figure 4.6a). We estimate that the additional tip illumination through the SPhP enhances the signal amplitude by an additional factor of about 1.5.

To verify that the gold edge indeed launches a surface phonon polariton, we recorded a large s-SNOM image (Figure 4.7 panels a,b) at 1114 cm^{-1} (photon wavelength λ = 9.0 µm) provided by a quantum cascade laser (MIRcat, Daylight Solutions). We see fringes parallel to the gold edge with a spacing of d = 24 µm, caused by the interference of the SPhP field with the incident field at the position of the tip apex[56,104]. For α = 42° (angle of incidence with respect to the sample surface) we obtain a SPhP wavelength of λ_{SPhP} = 8.1 µm according to $\lambda_{SPhP} = \lambda d/[\lambda + d\cos\alpha]$, matching the calculated SPhP wavelength using the relation $2\pi/\lambda_{SPhP} = \mathrm{Re}\left[\omega/c\sqrt{\epsilon_{c\text{-}SiO2}/(\epsilon_{c\text{-}SiO2}+1)}\right]$. Note that for this s-SNOM experiment the laser focus size had to be enlarged significantly as compared to the nano-FTIR experiments, in order to illuminate both tip and gold edge for distances as large as 100 µm, which is required for unambiguous observation of the interference fringes.

We apply the edge-launched SPhPs for enhancing nano-FTIR signals and measure the spectrum of PEO on quartz at 1 µm distance from the gold edge (solid blue curve in Figure 4.6b). By determining the spectral contrast Δs_4 (blue curve, inset of Figure 4.6b) we obtain C = 3.4, which corresponds to 750% of the value obtained for PEO on the Au substrate and almost 1400% of the value obtained on Si, the latter being the standard nano-FTIR substrate.

We note that the value of C oscillates with distance to the gold edge according to the local field at the tip apex that is governed by the interference between the incident and SPhP field (Figure 4.7b), which we demonstrate by measuring nano-FTIR spectra at various distances from the gold edge. The spectra recorded on pure quartz (obtained when the tip is positioned in between PEO islands, Figure 4.7c) clearly show a modulation of the peak maxima with increasing distance from the Au edge. The peak height agrees well with the behavior of the s-SNOM amplitude signal shown in Figure 4.7b. We then recorded the spectra of PEO on quartz, at the same distances from the Au edge obtained when the tip is positioned on top of the PEO

islands, Figure 4.7d) and calculated the spectral contrast Δs_4 (Figure 4.7e). We find that the spectral contrast indeed follows the local field above the quartz surface, which is determined by the interference of the incident field and the field of the surface phonon polariton launched at the gold edge.

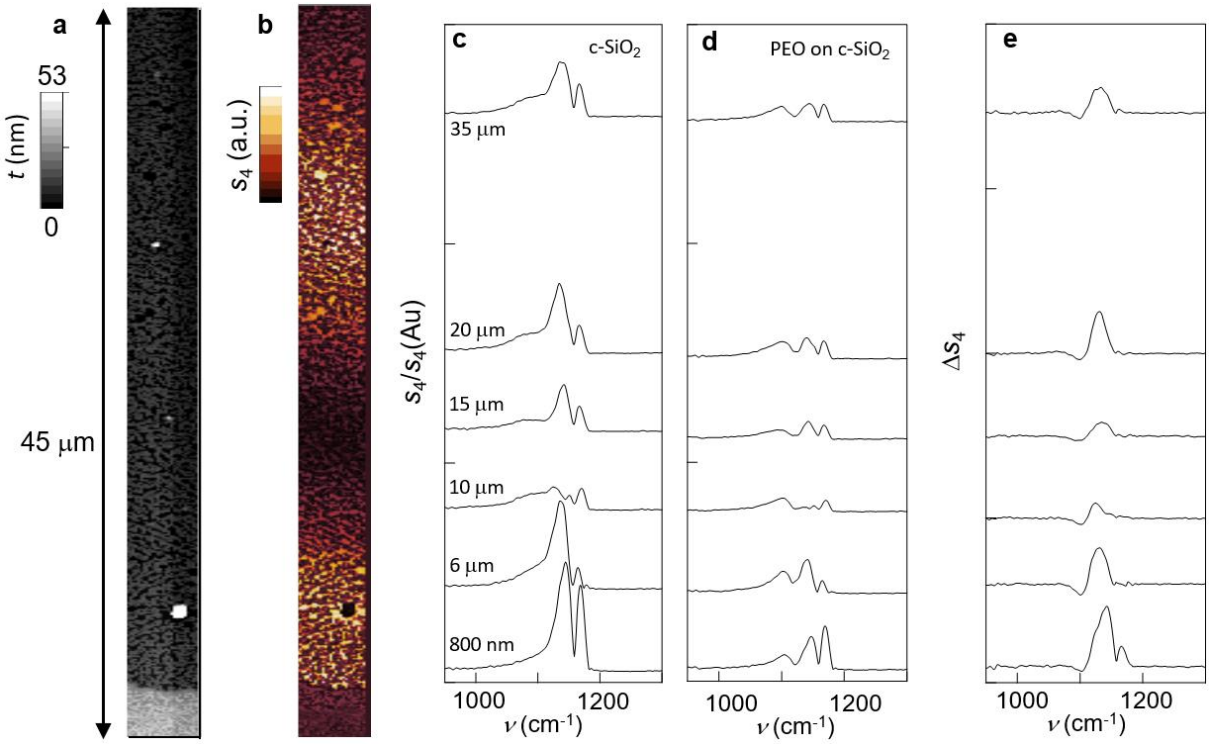

Figure 4.7. s-SNOM images and nano-FTIR amplitude spectra of PEO on quartz substrate close to a gold edge. (a) AFM topography image and (b) infrared amplitude image (recorded at 1114 cm^{-1}) of a large area of PEO on quartz close to a gold edge (seen at the bottom). (c and d) nano-FTIR amplitude spectra of quartz (c) and PEO on quartz (d), recorded at several distances (provided by the numbers labeling the spectra) from the gold edge. (e) spectral contrast Δs_4 calculated at each distance.

4.6 Increased tip-substrate coupling on ultra-thin films

To gain further insights into the spectral contrast enhancement, particularly for thinner molecular layers, we show simulations of nano-FTIR spectra in Figure 4.8 (experimentally we could not achieve PEO layers thinner than 13 nm). Figure 4.8a shows spectra of 1 nm and 2 nm thick PEO layers on the quartz substrate (brown and green curves, respectively) in comparison to the 13 nm thick PEO layer on quartz (red curve) and the pure quartz spectrum (blue curve). We clearly see a significant modification of the quartz spectrum caused by even these thin PEO layers. Following the procedure described in Figure 4.5, we calculate the maximum spectral contrast $C_{c\text{-}SiO2}(d)$ of the molecular vibration of a PEO layer of thickness d on a quartz substrate. The black curve in Figure 4.8b shows that for a few nanometer thick layer the spectral contrast $C_{c\text{-}SiO2}$ is larger than that of a 13 nm thick PEO layer on a gold substrate. $C_{c\text{-}SiO2}$ reaches a

maximum around 10 nm PEO thickness, before it decreases with increasing *d*. We explain this decrease by the decreasing tip-substrate near-field coupling. For a comparison, we show the thickness-dependent spectral contrast $C_{Au}(d)$ for PEO layers on a gold substrate (black dashed curve), highlighting that the enhancement of the PEO spectral contrast on the quartz substrate increases for thinner PEO layers. This observation can be better appreciated by plotting the ratio $C_{c\text{-}SiO2}(d)/C_{Au}(d)$ in Figure 4.8c (black curve). The increasing enhancement for thin layers can be explained by the stronger surface phonon polariton excitation when the distance between tip and quartz decreases.

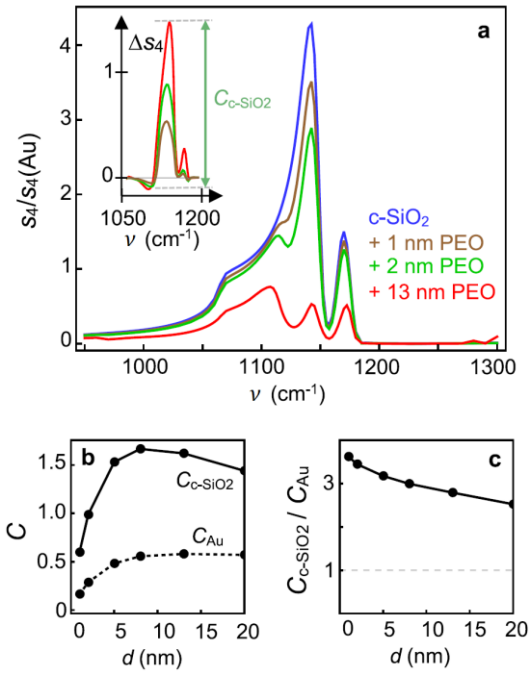

Figure 4.8. Simulation of thickness-dependent spectra and spectral contrasts. (a) Calculated nano-FTIR amplitude spectra of differently thick PEO layers on a quartz substrate. Inset: Spectral contrast Δs_4 of the differently thick PEO layers, analogous to Figure 4.5. (b) Maximum spectral contrast for differently thick PEO layers on quartz and Au substrates, $C_{c\text{-}SiO2}$ and C_{Au} (c) Ratio $C_{c\text{-}SiO2}/C_{Au}$.

4.7 Summary and Conclusions

In summary, we first demonstrated the crucial role of highly reflecting substrates for enhancing the infrared nanospectroscopy signals of thin molecular layers. Au substrates were found to provide an about one order of magnitude enhancement of nano-FTIR spectral signatures as compared to CaF_2 substrates. Exploiting tip-induced surface phonon polariton excitation in polar crystal substrates (here quartz), a further enhancement by a factor of 3 can be achieved. An even further enhancement could be achieved by implementing additional tip illumination which includes propagating surface polaritons, altogether boosting the nano-FTIR spectroscopic signal of molecular vibrations by nearly one order of magnitude compared to nano-FTIR employing Au substrates. Polariton-enhanced nano-FTIR spectroscopy - eventually

in combination with infrared-resonant tips[105] - could open promising avenues for molecular vibrational spectroscopy of very thin layers of analytes, monolayers or maybe even single molecules. Finally, we speculate that polariton-enhanced near-field coupling could also boost the sensitivity in tip-enhanced photothermal infrared nanospectroscopy[41] and photo-induced force microscopy[43,44].

The enhancement of nano-FTIR spectroscopy by tip-induced resonant surface polariton excitation could be realized with various substrates supporting either surface phonon polaritons (polar crystals such as SiC or Al_2O_3)[55], dielectrically loaded polar crystals that provide stronger surface polariton confinement[97,106] or surface plasmon polaritons. The latter exhibit resonances at mid-infrared frequencies on highly doped semiconductors, offering the advantage that the resonances can be spectrally shifted via the carrier concentration to match specific molecular vibrations[80] (illustrated in Figure 4.9 for a hypothetical semiconductor material with various carrier concentrations). Strong resonances could be achieved with semiconductors with large carrier mobilities, such as GaAs or InAs[107–110]. On the other hand, tip-induced surface polariton excitation (as described in this work) cannot be achieved by employing extended flat slabs (flakes) of uniaxial 2D materials (such as h-BN[111]) as a substrate, as they do not support *surface* polaritons at the slab surface. Surface polaritons exist at the flake edges[112] but resonant coupling with the tip has not been reported yet. Nevertheless, it might be worth exploring mechanisms to enhance nano-FTIR signals by exploiting graphene plasmons[113,114] or hyperbolic plasmon and phonon polaritons in multilayer 2D materials such as h-BN[111].

We finally note that focusing of surface polaritons onto the probing tip – independent of polariton-resonant tip-substrate coupling - could further boost the nano-FTIR signals. This could be accomplished, for example, with appropriately designed polariton launchers on conventional polar crystals[115], metal films or van der Waals material substrates[116–118] as well as on plasmonic[91–93] and phononic resonators[101,119–122]. Although the required substrate structuring might limit imaging applications, the combination of nano-FTIR with polariton launchers and resonators could become a valuable platform for studying strong light-matter interactions at the nanoscale, particularly of infrared light and molecular vibrations[92,101].

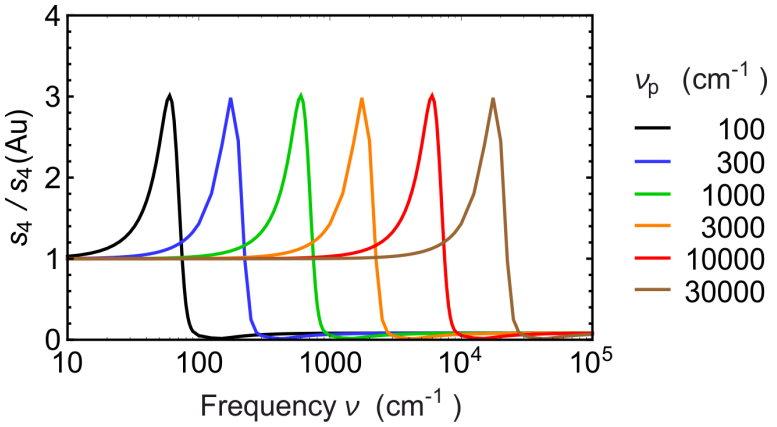

Figure 4.9: Spectrally tuneable tip-substrate resonance on doped semiconductors. nano-FTIR amplitude spectra normalized to gold, s_4/s_4(Au), calculated for a hypothetical semiconductor material with varying plasma frequencies ν_p, damping coefficient $\gamma = 0.3\nu_p$, high-frequency permittivity $\epsilon_\infty = 2$ and electron effective mass $m^* = m_e$, where m_e is the free electron mass. The plasma frequency relates to the carrier concentration N via $\nu_p^2 = Ne^2/(\epsilon_\infty \epsilon_0 m^*)$, where e is the elementary charge and ϵ_0 is the vacuum permittivity.

5 Subsurface chemical nanoidentification by nano-FTIR spectroscopy

Nano-FTIR spectroscopy based on Fourier transform infrared near-field spectroscopy allows for label-free chemical nanocharacterization of organic and inorganic composite surfaces. The potential capability for subsurface material analysis, however, is largely unexplored terrain. In this chapter, nano-FTIR spectroscopy of subsurface organic layers is demonstrated, revealing that nano-FTIR spectra from thin surface layers differ from that of subsurface layers of the same organic material. Further, the correlation of various nano-FTIR peak characteristics is studied, thereby establishing a simple and robust method for distinguishing surface from subsurface layers without the need of theoretical modelling or simulations (provided that chemically induced spectral modifications are not present). The experimental findings are confirmed and explained by a semi-analytical model for calculating nano-FTIR spectra of multi-layered organic samples. The results are critically important for the interpretation of nano-FTIR spectra of multilayer samples, particularly to avoid that geometry-induced spectral peak shifts are explained by chemical effects.

5.1 Introduction

S-SNOM and nano-FTIR are often considered to be surface characterization techniques, however, the finite penetration depth of near fields into the sample allows for subsurface probing of nanoscale structures and defects up to a depth of 100 nm.[19,20,24,28,123] For s-SNOM it has been also shown that depth-resolved information – with the potential of three-dimensional sample reconstruction - can be obtained by analysis of several higher harmonic signals, each of them having a different probing depth.[23,25–27] However, the potential capability for chemical identification of subsurface material by nano-FTIR experiments is largely unexplored terrain.

In this chapter, an experimental and theoretical nano-FTIR spectroscopy study of thin subsurface organic layers is presented. It is demonstrated (*i*) that nano-FTIR peaks of subsurface layers are shifted to lower frequency as compared to that of bulk materials or thin surface layers, and (*ii*) that surface and subsurface layers can be differentiated by analyzing the ratio of peak heights obtained at different demodulation orders *n*, without theoretical modelling or simulations. To that end, an exemplary study of the well-defined C = O vibrational mode of a thin polymethyl-methacrylate (PMMA) layer on silicon covered by a polystyrene (PS) layer of varying thickness is performed and then compared with differently thick uncovered PMMA layers on silicon. It is further elucidated how a semi-analytical model can be used to understand and predict nano-FTIR spectra of multi-layered samples. Finally, the validity and applicability of the findings for a large variety of materials is demonstrated, by summarizing and discussing the results of an extended theoretical and experimental study of the nano-FTIR peak characteristics of differently thick subsurface layers exhibiting various molecular vibrational modes. The results were previously published in *Nature Communications* (Ref. 22).

5.2 Systematic nano-FTIR spectroscopy study of subsurface organic layers

For subsurface infrared near-field spectroscopy we use the experimental s-SNOM and nano-FTIR setup explained in chapter 3.6. For convenience, a short description of the setup is given in Figure 5.1a. Importantly, the AFM tip acts as an optical antenna and creates strongly enhanced near fields around the tip apex, yielding a spatial resolution in the order of the tip radius, here R = 25 nm. Furthermore, the near fields penetrate into the sample (Figure 5.2b), thus allowing for probing of subsurface material. For a quantitative analysis of subsurface nano-FTIR spectra, all spectra in this chapter are normalized to the nano-FTIR spectrum of a clean silicon substrate via $\sigma_n^{\text{norm}} = \sigma_n/\sigma_n^{\text{Si}}$. We focus our analysis on organic sample systems and thus evaluate normalized nano-FTIR phase spectra $\varphi_n^{\text{norm}}(\nu) = \text{Arg}[\sigma_n/\sigma_n^{\text{Si}}]$, which qualitatively relate to the absorptive properties of molecular samples.[19,85,88,124] The superscript $^{\text{norm}}$ is omitted in the following for simplicity.

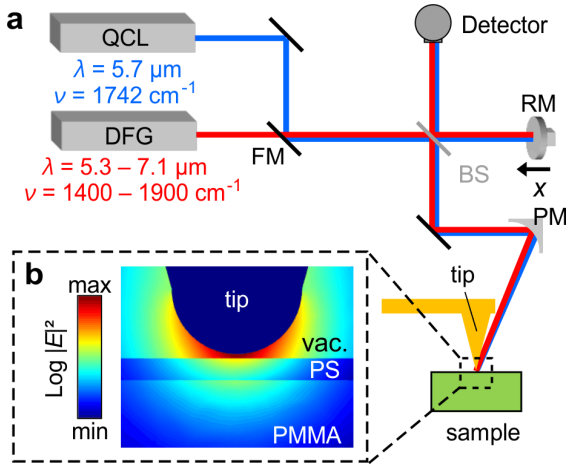

Figure 5.2: Experimental s-SNOM and nano-FTIR setup. (a) Illustration of the s-SNOM and nano-FTIR setup. A quantum cascade laser (QCL) is used for s-SNOM imaging. An infrared laser continuum based on difference frequency generation (DFG) is used for nano-FTIR spectroscopy. The light source is selected with a flip mirror (FM). A parabolic mirror (PM) is used for focusing the laser radiation onto the tip apex. After collection of the tip-scattered light with the PM, a Michelson interferometer comprising a beam splitter (BS) and moveable reference mirror (RM) is used for detection. (b) Near-field distribution $|E|^2$ around the tip apex (30 nm radius) of a 10 µm-long silicon cone with 20 nm-thick gold coating located 2 nm above a sample comprised of a 10 nm-thick PS layer (with permittivity ϵ_{PS}=2.5)[125] on PMMA (with permittivity ϵ_{PMMA} = 1.52+i0.83)[126]. Simulated with the COMSOL Multiphysics software based on the finite element method, for an illumination wavelength λ = 5.75 µm, corresponding to ν = 1739 cm^{-1}, at illumination angle of 60° with respect to the sample surface normal.

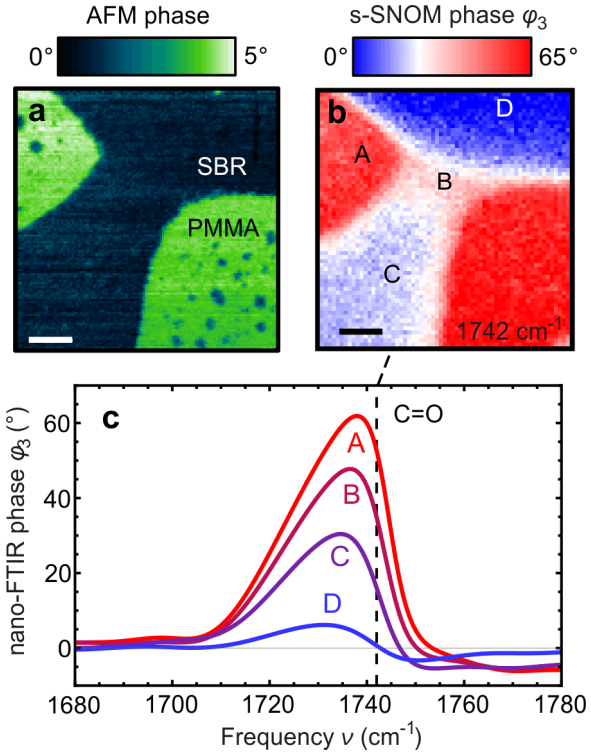

Figure 5.3: Near-field imaging and spectroscopy of organic nanocomposites. (a) AFM mechanical phase image of a two-component rubber blend (SBR/PMMA) and (b) corresponding s-SNOM phase φ_3 image recorded at 1742 cm^{-1}, which maps the absorption of the C=O vibrational mode of PMMA. Scale bar: 200 nm. (c) Nano-FTIR phase φ_3 spectra of selected positions A - D. Vertical dashed line marks the imaging frequency.

5.2.1 Motivation

We motivate our systematic nano-FTIR spectroscopy study of well-defined multilayer samples with s-SNOM images and nano-FTIR spectra of a Styrene-Butadiene-Rubber (SBR) / PMMA composite sample of unknown vertical structure. The sample was fabricated by drop-casting a commercially available solution of SBR and PMMA (Nanosurf) onto a silicon substrate. Figure 5.3a shows the AFM mechanical phase image, revealing two homogeneous areas that indicate a separation of PMMA and SBR with sharp boundaries at the sample surface. To map the absorption of the C=O vibrational mode of PMMA, we recorded an s-SNOM phase image of the same area at ν = 1742 cm^{-1} (Figure 5.3b). We find two strongly absorbing areas (red, marked A), corresponding to the green areas in the mechanical phase image (Figure 5.3a) that subsequently can be identified as PMMA (note that SBR has no absorption in the spectral region of the C=O bond[127]). Interestingly, we find significant s-SNOM phase signals within the SBR area, indicating the presence of PMMA. Considering the sharp material boundaries observed in the mechanical phase images, we assume that PMMA is located below the SBR. The presence of PMMA is confirmed by nano-FTIR spectra recorded at positions B-D, which clearly reveal the same spectral peak as observed at position A (Figure 5.3c). However, we observe a significant shift of the peak to lower frequencies when the peak maximum decreases.

As we can exclude peak shift due to chemical interaction[128,129], we speculate that the peak shifts are due to the subsurface location of PMMA. To corroborate subsurface nano-FTIR spectroscopy of organic materials and to confirm that it comes along with significant peak shifts, we performed a fundamental comparative study of multilayer organic samples with well-defined composition and geometry, as described in the following.

5.2.2 Experiments on PMMA/PS test sample

As model sample for subsurface nano-FTIR spectroscopy we have chosen a PMMA layer of thickness t_2 = 59.4±4.7 nm on a silicon substrate that is covered by a PS layer of varying thickness d_2 = 0 to 110 nm (see schematics and AFM line profile in Figure 5.4a). The sample was fabricated by spin-coating a 2% solution of PMMA (molecular weight 495 kDa) dissolved in Anisole at 6000 rpm for 60 s onto a clean silicon substrate and subsequently annealing the sample at 180 °C for 90 s to achieve a smooth PMMA surface. PS was spin-coated using the same parameters (but no annealing) on two identical PMMA surfaces as 1.5% and 3% solution in 1-chloropentane (yielding a different range of PS thickness depending on the concentration). We chose 1-chloropentane as chemically selective solvent for PS to ensure a sharp interface between the layers.[130] The wedge shape was obtained by tilting the sample at an angle of ~15° during the PS spin coating step. The heights of the PMMA and PS layers were determined by AFM height measurements, after the underlying silicon substrate was scratched free with freshly cleaned tweezers. Reference nano-FTIR phase spectra of PMMA and PS are shown in Figure 5.4b. We identify PMMA via the C=O vibrational stretch mode around 1738 cm^{-1}.[76] The smaller plateau-like feature around 1440 to 1500 cm^{-1} corresponds to vibrations in the O-CH_3 group. Characteristic for PS are the two distinct absorption lines at 1452 cm^{-1} and 1493 cm^{-1} (and a weaker mode at 1601 cm^{-1}), which arise from C-C stretching vibrations in the aromatic ring.[131] The reference spectrum of PS does not exhibit any phase contrast around 1700 to 1800 cm^{-1}, i.e. it is spectrally flat, which simplifies the following discussion.

Figure 5.4c shows subsurface nano-FTIR spectra of PMMA at different depths d_2 below PS. Without a capping layer (red, d_2 = 0), we clearly observe the characteristic C=O and O-CH_3 vibrational modes of PMMA. As the depth d_2 of the PMMA layer (i.e. thickness t_1 of the PS capping layer) increases, the spectral feature from 1440 to 1500 cm^{-1} gradually changes from plateau-like (which is characteristic for PMMA) towards two distinct peaks at 1452 cm^{-1} and 1493 cm^{-1} (which are characteristic for PS). Simultaneously, the C=O peak height (PMMA) rapidly decreases with depth d_2, but still allows for chemical identification of PMMA at a depth of d_2 = 110 nm. We note that the C=O peak shifts to lower frequencies (red shifts) with increasing depth (indicated in Figure 5.4c by $\Delta\nu_3^{max}$), which reminds us of peak-shifts previously reported in experimental nano-FTIR studies of surface PMMA layers[18] and surface silicon dioxide layers[69] of varying thicknesses.

In order to better understand the nano-FTIR phase spectra, we focus our analysis on the C=O peak of PMMA around 1738 cm^{-1}. Specifically, we investigate the depth-dependence of the spectral peak position ν_n^{max} and peak height φ_n^{max} (defined in the inset of Figure 5.5) for the

two different higher harmonic demodulation orders n = 3 and n = 4. For comparison, we performed a similar study on thin PMMA layers of varying thickness t_1 at the surface. The results are shown in Figure 5.5 (large symbols).

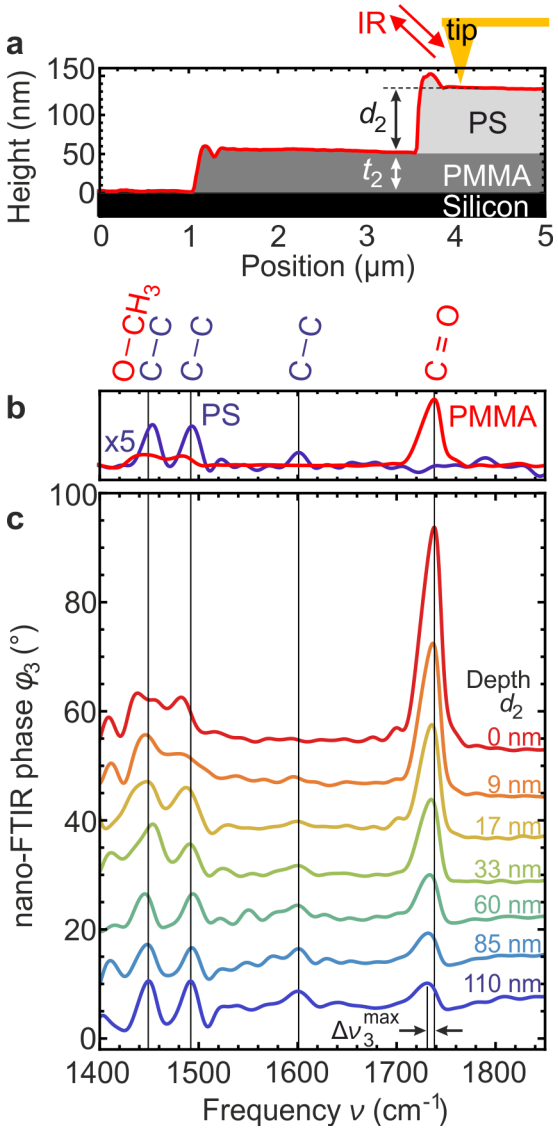

Figure 5.4: Subsurface nano-FTIR spectroscopy experiments on well-defined multi-layer samples. (a) Schematics of the experiment and PMMA/PS test sample, including the topography line profile of a d_2 = 85 nm-thick PS layer covering the t_2 ≈ 59.4 nm-thick PMMA layer on Si. (b) Reference nano-FTIR phase spectra recorded on thick PMMA and PS layers. (c) Subsurface nano-FTIR phase spectra of PMMA at different depths d_2 below PS (average of 50 spectra (80 spectra for d_2 ≥ 85 nm), 30 s acquisition time per interferogram, ×128 zero filling, 17 cm^{-1} spectral resolution). Black arrows in (c) indicate the spectral peak-shift $\Delta\nu_3^{max}$.

Figure 5.5a,b show the results for the subsurface PMMA layer. We observe that the peak height (Figure 5.5a) for both demodulation orders rapidly decreases when the depth d_2 of the PMMA layer (i.e. thickness of the PS capping layer) increases. This decay can be explained by the exponential decay of the near fields from the tip apex into the sample (as seen in Figure 5.2b). The deeper the PMMA layer, the less near fields it is absorbing, i.e. the less material is probed. The C=O peak can still be identified at a depth of d_2 = 110 nm. Further, we observe a red shift of the peak position with respect to the peak position ν_{ref} (horizontal line in Figure 5.5 panels b,d) with increasing d_2 (of up to $\Delta\nu_3^{max} = \nu_{ref} - \nu_3^{max}$ = 7 cm^{-1} at d_2 = 110 nm). Interestingly, we find that signal demodulation at higher harmonics yields stronger red-shifts and a faster decay of the peak height with increasing depth, that is, the relative contrast $C = \varphi_4^{max}/\varphi_3^{max}$ decreases with increasing depth. We attribute this behavior to the stronger confinement of near fields to the tip apex at higher demodulation orders[20,21,27]. We further analyze C below to distinguish nano-FTIR spectra of subsurface layers from thin layers at the surface.

For comparison, Figure 5.5c,d show the results for the surface PMMA layers of varying thickness t_1. We observe that the peak height φ_n^{max} for both demodulation orders slowly decreases when the thickness t_1 of the PMMA layer decreases. This decay can be explained by the decreased amount of absorbing material within the nano-FTIR probing volume. The thinner the PMMA layer, the less near fields it is absorbing, i.e. more silicon is probed, which is non-absorbing in this spectral range. Further, we see a red-shift of the peak position with decreasing t_1 (of up to $\Delta\nu_3^{max}$ = 2 cm^{-1}), as previously reported and explained by Mastel et al.[18] A thin organic layer on a highly reflective substrate promotes reflections of near fields between the tip and sample, which changes the probing mechanism from absorption-like to an absorption-reflection mechanism, thus causing a shift of the peak position.[18] Interestingly, Figure 5.5 also shows that the spectral peak shift in nano-FTIR phase spectra is much larger for subsurface layers when compared to surface layers. Notably, and in contrast to the subsurface PMMA layers, we find that the relative contrast $C = \varphi_4^{max}/\varphi_3^{max}$ and the spectral peak position for PMMA layers at the sample surface vary only slightly with the demodulation order n, as we further analyze and exploit below.

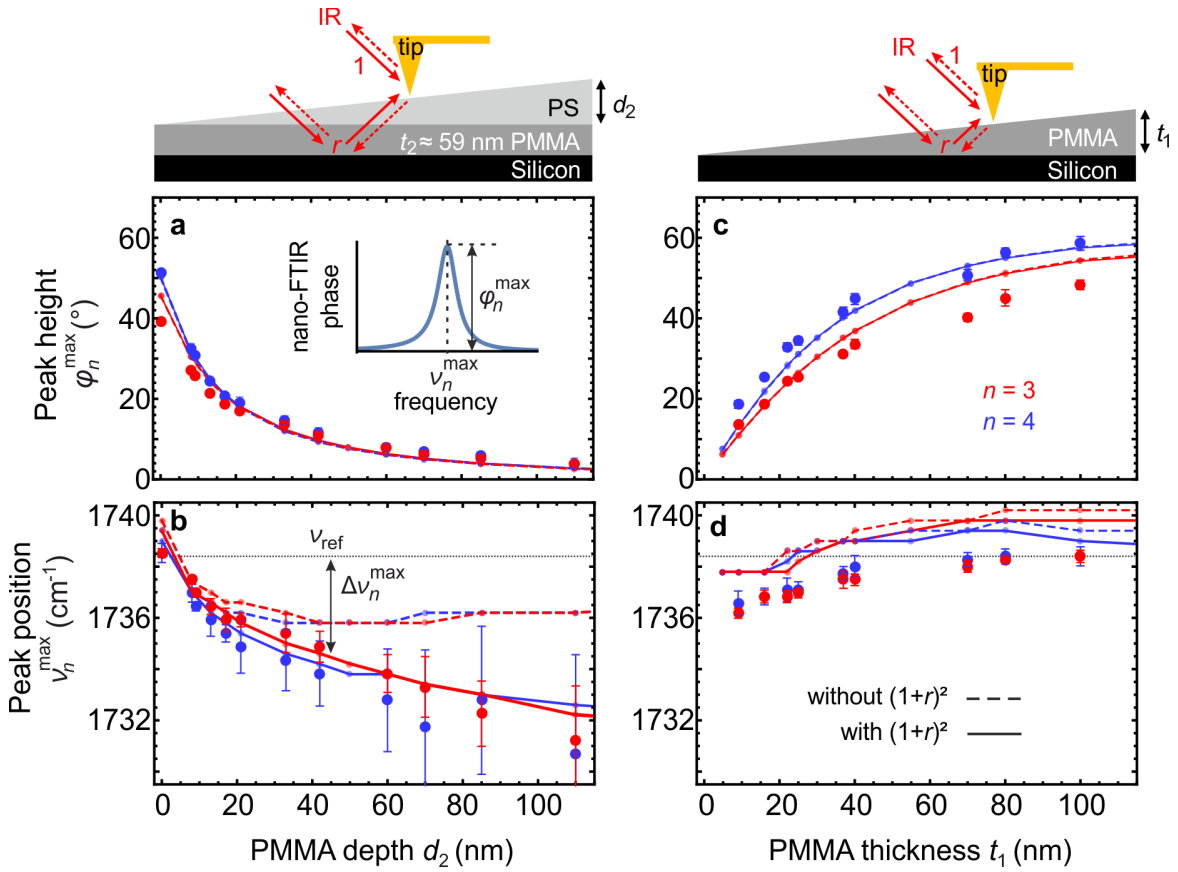

Figure 5.5: Comparison of PMMA subsurface layers and thin PMMA surface layers. (a,c) Peak heights φ_n^{max} and (b,d) spectral peak positions ν_n^{max} extracted from experimental (large dots) and calculated (lines) nano-FTIR phase spectra as a function of PMMA depth d_2 (left column) and PMMA thickness t_1 (right column), for different demodulation orders n = 3 (red) and n = 4 (blue). The solid and dashed lines are calculated with and without the far-field factor $(1+r)^2$ in Equation (1) respectively. The gray horizontal dotted line indicates the peak position ν_{ref} experimentally obtained on thick PMMA surface layers. Inset: definition of φ_n^{max} and ν_n^{max}. Each experimental data point shows mean values and standard deviation (error bars) obtained from 10 averaged (5×) spectra (16 averaged spectra for d_2 ≥ 85 nm).

5.2.3 Interpretation of nano-FTIR spectra of multi-layered samples

To better understand nano-FTIR spectra of vertically inhomogeneous samples, we performed model calculations based on the finite dipole model (FDM), which is illustrated in Figure 5.6a and explained in more detail in chapter 3.4.3. In short, s-SNOM signals are described by calculating the scattering coefficient $\sigma = E_{scat}/E_0$, where E_0 is the incident field and E_{scat} is the tip-scattered field. The tip is modelled as elongated spheroid with major half-axis length L and tip apex radius R. It is illuminated directly and indirectly via reflection at the sample surface with the far-field reflection coefficient r, yielding a local electric field at the tip, $E_{loc} \propto (1+r)E_0$, which induces an electric dipole p_0 in the tip. The near-field interaction of p_0 with the sample is mediated predominantly via one of the charges associated with this dipole, Q_0, located close to the tip apex,[13,48] which induces an additional dipole p_1 in the tip. The total induced dipole moment is $p = p_0 + p_1 = \alpha_{eff}E_{loc}$, where α_{eff} is the effective polarizability of the coupled tip-sample system. The scattered (far) field of this dipole is measured directly and via reflection from the sample, $E_{scat} \propto (1+r)p$. The scattering coefficient can thus be described by

$$\sigma = (1+r)^2\alpha_{eff}. \tag{5.1}$$

In the FDM the effective polarizability is given by [13,48]

$$\alpha_{eff} = 1+\frac{1}{2}\frac{f_0(H)\beta(\epsilon)}{1 - f_1(H)\beta(\epsilon)}, \tag{5.2}$$

where $\beta = (\epsilon-1)/(\epsilon+1)$ is the quasi-electrostatic reflection coefficient of a semi-infinite (bulk) sample with permittivity ϵ, and $f_i(H)$ (given in Equation (3.23)) describe the tip geometry and tip-sample distance $H(t) = A(1+\cos\Omega t)$. The higher harmonic signal demodulation (used for background suppression) is included in the model as explained in chapter 3.3 by taking the nth Fourier coefficient $\hat{F}_n$ with respect to time, yielding the nth-order demodulated scattering coefficient [13,48]

$$\sigma_n = (1+r)^2\hat{F}_n\left[1+\frac{1}{2}\frac{f_0\big(H(t)\big)\beta}{1 - f_1\big(H(t)\big)\beta}\right]. \tag{5.3}$$

To facilitate the interpretation of Equation (5.3) in the following, we express the scattering coefficient as Taylor series in β of order N,[52] such that nano-FTIR signals are simply proportional to powers j of β:

$$\sigma_n \approx (1+r)^2\cdot\frac{1}{2}\sum_{j=1}^{N}\hat{F}_n\left[f_0 f_1^{j-1}\cdot\beta^j\right], \tag{5.4}$$

which is valid for weak molecular oscillators with $|\beta| < 1$ (which includes for example polymers and biological matter).

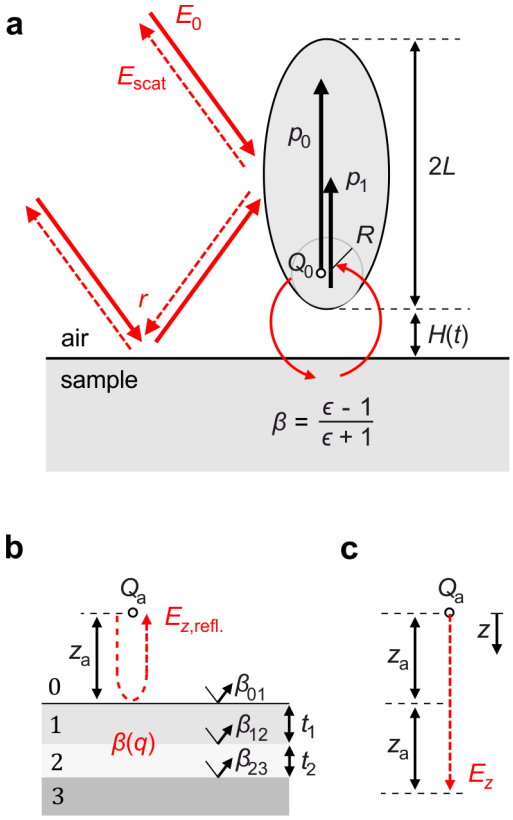

Figure 5.6: Illustration of the finite dipole model for bulk and multi-layered samples. (a) The nano-FTIR tip is modelled as a prolate spheroid of length $2L$ and apex radius R, which is located at height $H(t)$ above a bulk sample with permittivity ϵ and electrostatic reflection coefficient $\beta = (\epsilon\text{-}1)/(\epsilon+1)$. The incident electric field E_0 induces the primary electric dipole p_0, which interacts with the sample via the point charge Q_0, yielding the near-field induced dipole p_1 (indicated by red curved arrows). The model accounts for far-field illumination and detection of the tip-scattered field E_{scat} via reflection at the sample surface, described by the Fresnel reflection coefficient r (indicated by red straight arrows). (b-c) Illustration of (b) monopole field reflected at a multilayer sample, $E_{z,refl}$, and (c) monopole field E_z without sample. Both red dashed arrows have a length of $2z_a$. The multilayer sample in (b) is characterized by the quasi-electrostatic reflection coefficient $\beta(q)$, which is obtained from the single-interface electrostatic reflection coefficients β_{ij} and layer thicknesses t_j.

Equations (5.3) and (5.4) can be used to calculate relative material contrasts in nano-FTIR spectroscopy, however, they are valid only for semi-infinite samples. To extend the model to multi-layered samples, we use the multi-layer reflection coefficient $\beta(q)$ which depends on the momentum q and for one layer on a substrate it is given by [18,54]

$$\beta(q) = \frac{\beta_{01}+\beta_{12}\exp(-2qt_1)}{1+\beta_{01}\beta_{12}\exp(-2qt_1)}, \tag{5.5}$$

where $\beta_{ij} = (\epsilon_j - \epsilon_i)/(\epsilon_j + \epsilon_i)$ are the single-interface reflection coefficients and t_1 is the layer thickness, as indicated in Figure 5.6b. Multiple layers on a substrate can be described by recursively using Equation (5.5) as expression for β_{12}.[51] The FDM (Equation (5.3) and (5.4)), however, does not explicitly support momentum-dependent reflections (because the quasi-

static approximation $q \to \infty$ is made). Instead of using the FDM for layered samples by Hauer et al. (chapter 3.4.4), we substitute β in Equation (5.3) and (5.4) by the effective near-field reflection coefficient $\bar{\beta} = E_{z,\mathrm{refl}}/E_z$, where $E_{z,\mathrm{refl}}$ is the electric field produced by an effective point charge Q_a (located at a distance z_a from the sample surface, Figure 5.6b), reflected at the multi-layered sample surface and evaluated at the position of Q_a itself (indicated by red dashed arrow in Figure 5.6b). E_z is the electric field of Q_a at a distance of $2z_\mathrm{a}$ (Figure 5.6c). It can be shown (see Appendix 6.3) that

$$\bar{\beta} = \frac{E_{z,\mathrm{refl}}}{E_z} = \frac{\int_0^\infty \beta(q) q \mathrm{e}^{-2qz_\mathrm{a}}\,\mathrm{d}q}{\int_0^\infty q \mathrm{e}^{-2qz_\mathrm{a}}\,\mathrm{d}q}, \tag{5.6}$$

where $z_\mathrm{a} = H(t) + a$. Here a describes the height of the effective charge Q_a above the tip apex. The value a will be found such that good agreement between calculation and experiment is achieved. In contrast to the description by Hauer et al. (Equation (3.27)), the effective reflection coefficient $\bar{\beta}$ in Equation (5.6) can directly be interpreted as the weighted average of $\beta(q)$, averaged over momenta q with the weight of each q given by $q\mathrm{e}^{-2qz_\mathrm{a}}$. As further discussed below, this allows to directly relate nano-FTIR spectra to the sample's Fresnel reflection coefficient.

We use Equations (5.4) and (5.6) to calculate nano-FTIR phase spectra $\varphi_n(\nu)$ of surface and subsurface PMMA layers corresponding to the sample geometries of Figure 5.5 and extract the spectral peak positions $\nu_n^{\max}$ and peak heights $\varphi_n^{\max}$ for various layer thicknesses and depths. PMMA is described by dielectric permittivity data obtained by infrared ellipsometry[126] and we assume PS and Silicon to be non-absorbing in the considered spectral range, with $\epsilon_{\mathrm{PS}} = 2.5$ and $\epsilon_{\mathrm{Si}} \approx 11.7$.[95,125] The employed model parameters are: A = 30 nm, R = 30 nm, L = 200 nm, g = 0.65 (g describes the amount of induced charge that is relevant for the near-field interaction[13,48]). Convergence of the calculated $\nu_n^{\max}$ and $\varphi_n^{\max}$ (red and blue lines for demodulation orders n = 3 and n = 4, respectively) is achieved for Taylor expansion orders $N \geq 5$, and we find good agreement with the experimental data for $a = 1.4R$. The effective charge Q_a is thus located slightly higher than the charge Q_0 (located at distance R from the tip apex), indicating that the near-field interaction takes place also via the apex-near part of the tip shaft, which is located further away than the tip apex. Indeed, probing of subsurface layers is frequently attributed to the elongated tip shape, which provides longer-reaching evanescent waves (with lower momenta q) that are not captured well by the unmodified FDM for bulk samples.[24,54,69]

Note that for large subsurface layer depths $d_2 \geq 30$ nm we observe a dispersive line shape in the experimental nano-FTIR spectra (Figure 5.4c). We attribute this finding to the far-field reflection of both the illumination and tip-scattered field at the sample surface (considered in Equation (5.1) by the far-field refection coefficient r), which carries the far-field absorption characteristics of the subsurface PMMA layer. This PMMA far-field contribution to the tip-scattered field becomes notable when the near-field contribution vanishes at larger probing depths. We support our explanation with Figure 5.7, where we compare calculated nano-FTIR peak shapes, revealing that the far-field factor $(1+r)^2$ in Equation (5.1) indeed yields a dispersive

line shape for large d_2. For a more quantitative comparison we show in Figure 5.5 the calculated peak positions and peak heights obtained without the far-field reflection coefficient (dashed lines). We find that for d_2 < 20 nm the peak positions are nearly the same as for the calculation including the factor $(1+r)^2$ (solid lines), revealing that the peak shift is essentially a near-field effect. For d_2 > 20 nm, the peak shift stays rather constant and clearly differs from the calculation including the factor $(1+r)^2$. The continuous red shift for d_2 > 20 nm observed in the experiment can be thus attributed to the far-field contribution. We note that the constant peak position for d_2 > 20 nm does not imply the absence of near-field probing. The peak height still decreases until d_2 > 100 nm, which is a clear near-field signature. We finally note that for layers of lateral extensions smaller than the illumination wavelength we expect the contribution from the far-field reflection becoming less pronounced, yielding peak shifts located between the dashed and solid curves in Figure 5.5.

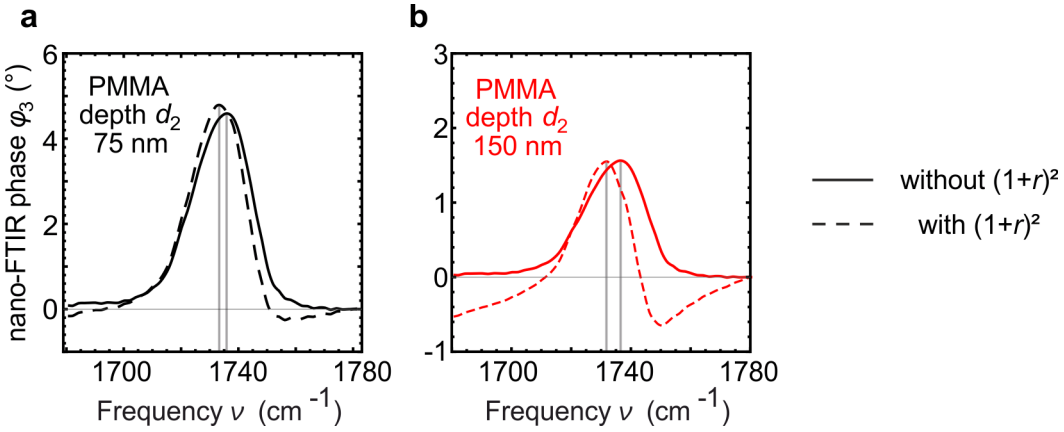

Figure 5.7: Calculated nano-FTIR phase spectra with and without far-field reflection at sample. Calculated nano-FTIR phase spectra of a t_2 = 59 nm-thin subsurface PMMA layer on a silicon substrate, located at depth (a) d_2 = 75 nm and (b) d_2 = 150 nm below PS. Dashed and solid lines are calculated with and without the factor $(1+r)^2$ in Equation (5.1), which accounts for far-field illumination and detection via the sample surface. Vertical gray lines indicate peak positions. The figure shows that the factor $(1+r)^2$ yields an additional red-shift of the peak (panel a) and an increasingly pronounced dispersive line shape with increasing depth of the subsurface layer. Note that in the experiment this effect appears already at smaller depth d_2.

5.2.4 Relating nano-FTIR spectra to the Fresnel reflection coefficient

The analytical nature of our model lets us elucidate the physical cause of the spectral peak shifts observed in nano-FTIR phase spectra of multi-layered samples. Our model (Equations (5.4) and (5.6)) shows that the spectral behavior of nano-FTIR signals essentially follows the spectral behavior of $\bar{\beta}$, as neither the exponent j nor the geometry-factors f_0 and f_1 in Equation (5.4) lead to spectral peak shifts. Furthermore, $\bar{\beta}$ can be interpreted as weighted average of $\beta(q)$, with the weights being determined by the (spectrally independent) coupling weight function (CWF)

$$w_{\mathrm{FDM}}(q,H) = q\mathrm{e}^{-2qz_{\mathrm{a}}(H)}. \tag{5.7}$$

To illustrate the spectral shifts, we compare in Figure 5.8 the phase of the Fresnel reflection coefficient, Arg $\beta(\nu,q)$, for three PMMA samples with different geometries. The C=O vibrational mode of PMMA is described by a dielectric function (plotted in Figure 5.8a), which can be well described by a Lorentz oscillator. It can be thus considered a highly representative example of a typical molecular vibration. Figure 5.8b shows Arg $\beta(\nu,q)$ of bulk PMMA. We find a spectral maximum (traced by the vertical black line) at 1741 cm^{-1}, which is independent of q. The situation changes for a thin PMMA layer (thickness t_1 = 20 nm) on a silicon substrate (Figure 5.8c). For decreasing q, we observe that the spectral maximum shifts to lower frequencies when compared to bulk PMMA (as indicated by $\Delta\nu$ in Figure 5.8c). Analyzing finally Arg $\beta(\nu,q)$ for a subsurface PMMA layer (thickness t_2 = 20 nm, on top of Si substrate and covered by a d_2 = 40 nm-thick PS layer), we find that for all momenta q the spectral maximum is shifted to lower frequencies compared to bulk PMMA (Figure 5.8d). This shift $\Delta\nu$ is larger than that of thin PMMA surface layers (Figure 5.8c) and increases with increasing q (contrary to the thin surface layer). For a comparison with nano-FTIR phase spectra $\varphi_n(\nu)$ we have to consider that the nano-FTIR tip provides and probes a broad distribution of momenta, which is described by the CWF, i.e. for a tip-sample distance H = 0 (Figure 5.8e). Note that similar expressions for a CWF are also found in mathematically rigorous s-SNOM models,[54,58,59] however a direct correlation with nano-FTIR spectra is less apparent due to the complexity of such models. Here, we multiply the CWF (Figure 5.8e) with the Fresnel reflection coefficient (Figure 5.8b-d) and subsequently integrate over all momenta q, and we obtain Arg $\bar{\beta}(\nu)$ (Figure 5.8f), which we directly compare with calculated nano-FTIR phase spectra $\varphi_3(\nu)$ (Figure 5.8g). We find qualitative agreement between the spectral shifts in Arg $\bar{\beta}(\nu)$ and $\varphi_3(\nu)$, indicating that the root cause of spectral nano-FTIR shifts in layered samples are spectral shifts of the multilayer Fresnel reflection coefficient and thus a true spectroscopic feature of the sample.

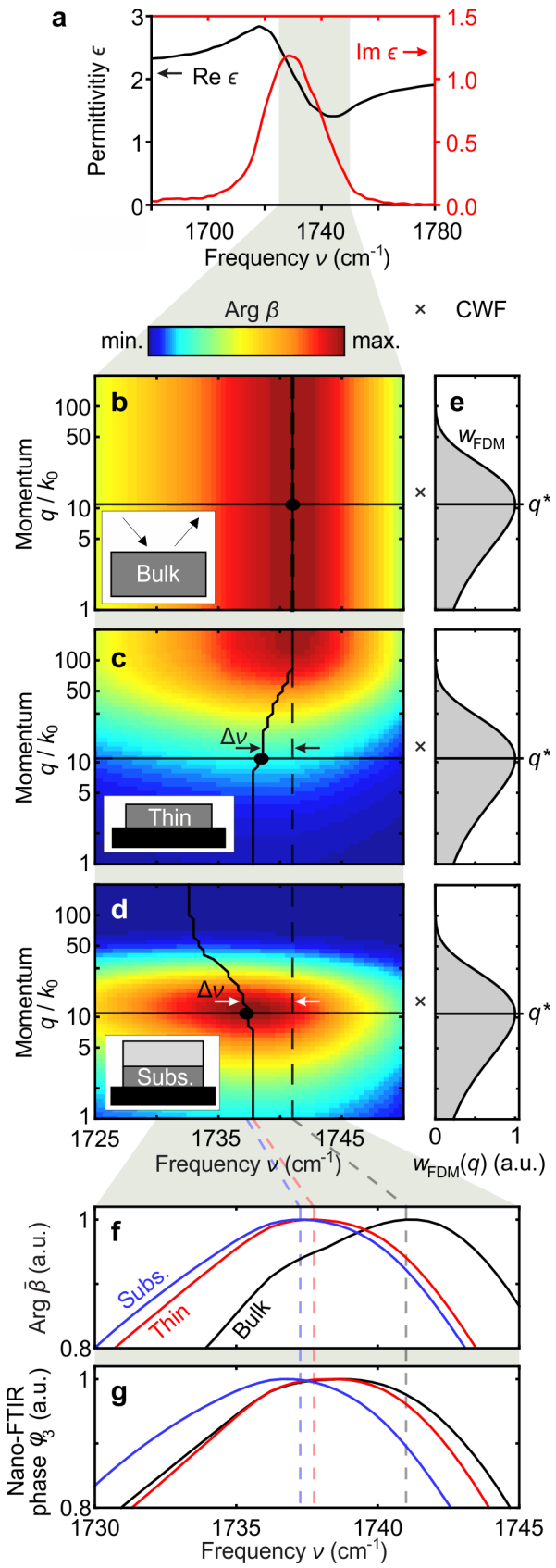

Figure 5.8: Geometry- and momentum-dependent spectral shifts in nano-FTIR phase spectra. (a) Real (black) and imaginary (red) parts of the dielectric function of PMMA, showing a typical Lorentz oscillator shape. (b-d) Phase of the Fresnel reflection coefficient, Arg β, for different PMMA samples: (b) bulk PMMA, (c) t_1 = 20 nm-thick PMMA layer at the surface of a silicon substrate, (d) t_2 = 20 nm-thick subsurface PMMA layer at the surface of a silicon substrate and at depth d_2 = 40 nm below PS. The vertical/curved solid lines indicate the frequency where Arg β has its maximum. (e) Coupling weight function w_{FDM} (q) calculated with the tip in contact with sample (H = 0). Horizontal lines indicate the momentum q^* of highest tip-sample coupling. (f) Phase of near-field reflection coefficient, Arg $\bar{\beta}$, obtained by multiplying the Fresnel reflection coefficient (panels b-d) with the CWF (panel e), and integration over all momenta q. (g) Calculated nano-FTIR phase spectra φ_3.

The quantitative differences between Arg $\bar{\beta}(\nu)$ and $\varphi_3(\nu)$ can be explained by signal demodulation in nano-FTIR, which has not been considered so far in our analysis of $\bar{\beta}$. Equations (5.4) and (5.6) imply that signal demodulation (described by the Fourier components $\hat{F}_n$) acts on the CWF, $w_{\mathrm{FDM}}(q,H)$, which depends on the modulated tip-sample distance H. It is well known[20,26,27] that s-SNOM imaging at higher demodulation orders improves the lateral spatial resolution and reduces the probing depths, indicating that near fields of larger momenta are probed. This corresponds to near-field probing at higher momenta q for increasing n, and explains the reduction of the nano-FTIR spectral peak shifts for surface layer and an increase for subsurface layers (compared to bulk) observed in Figure 5.8g. As probing with higher momenta implies better spatial resolution, we expect that inhomogeneities in surface layers can be better resolved than in subsurface layers.

We point out that the observed peak shifts observed in nano-FTIR are not specific to near-field spectroscopy. They also occur in far-field infrared spectroscopy, for example, when the reflected power $R = |r(\nu,q)|^2$ is measured.[132] This is because the far-field reflection coefficient $r(\nu,q)$ depends – as well as the quasi-electrostatic near-field reflection coefficient – on the momentum $q = k_0 \sin(\Theta)$, which in far-field spectroscopy is determined by angle of incidence, Θ. We illustrate this dependence in Figure 5.9 by calculating the reflected power of a 10 nm-thin PMMA layer on a silicon substrate that is illuminated under normal-incidence (Θ = 0 degree, red) and grazing-incidence (Θ = 90 degree, blue). Figure 5.9c shows that in this case a peak-shift of 10 cm^{-1} is observed.

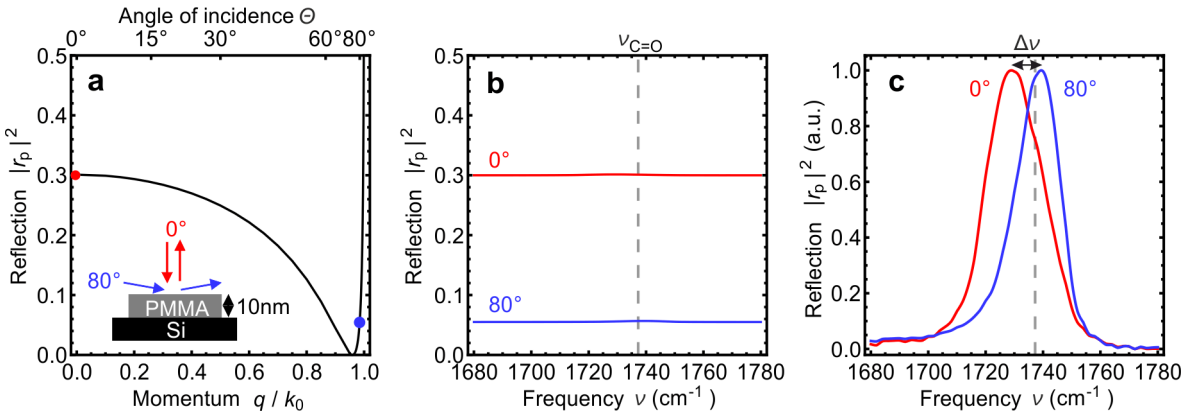

Figure 5.9: Momentum-dependent spectral peak shifts in far-field infrared reflection spectroscopy. Calculated reflected power $|r_p|^2$ of p-polarized infrared far-field radiation, reflected from the surface of a 10 nm-thin PMMA layer on a silicon substrate (as illustrated in the inset), (a) for varying in-plane momenta q which correspond to varying angles of incidence Θ via $q = k_0 \cdot \sin(\Theta)$ for a fixed frequency ν = 1737 cm^{-1} near the C=O vibrational mode of PMMA, (b) for varying frequencies ν at normal-incidence (Θ = 0°, red) and grazing-incidence (Θ = 80°, blue). (c) Same as panel b, but shown after baseline subtraction and normalization for better visibility of the angle-dependent spectral peak-shift $\Delta\nu \approx$ 10 cm^{-1}.

5.3 Model-free differentiation of subsurface and surface layers

Finally, we elucidate how the observed spectral differences between nano-FTIR spectra of thin organic layers at the surface and subsurface organic layers could be exploited for distinguishing the two cases without the need of theoretical modelling, which is to date still a challenging and time-consuming task. To this end, we analyze the correlation between peak height φ_3^{max} and spectral peak position ν_3^{max}, as well as the correlation between peak height φ_3^{max} and peak height ratio $C = \varphi_4^{max}/\varphi_3^{max}$. In Figure 5.10a,c (experimental and calculated data, respectively) we observe that the peak position in nano-FTIR phase spectra of both thin PMMA surface layers (black symbols) and PMMA subsurface layers (red symbols) show similar trends, i.e. that a decrease in peak height comes along with a spectral red-shift. However, for subsurface layers the red-shift is much stronger. The peak height ratio $C = \varphi_4^{max}/\varphi_3^{max}$ shows opposing trends for thin PMMA surface and subsurface layers (experimental and calculated data in Figure 5.10b,d, respectively). With decreasing peak height, we find that C increases for surface layers and decreases for subsurface layers. We explain this correlation of C and peak height by the reduced probing depth (and increased surface-sensitivity) at higher harmonic demodulation orders.[20,21,27] The reduced probing depth at higher harmonic demodulation orders (illustrated in Figure 5.11) causes φ_4^{max} to decrease faster than φ_3^{max}, as the depth d_2 of a subsurface layer increases – thus the ratio $\varphi_4^{max}/\varphi_3^{max}$ decreases for subsurface layers (Figure 5.11c,f). On the other hand, as the thickness t_1 of a surface layer decreases, the increased surface-sensitivity at higher demodulation orders causes φ_4^{max} to reduce slower than φ_3^{max} – thus the ratio $\varphi_4^{max}/\varphi_3^{max}$ increases for surface layers (Figure 5.11b,e).

In the calculations we also considered subsurface layers of different thicknesses t_2. We find that both the peak shifts and peak height ratios (red curves in Figure 5.10c,d respectively) are always located below the curves obtained for the surface layers (black lines). Our observations thus offer a rather easy procedure for distinguishing surface and subsurface layers. We assume that the correlations for PMMA surface layers (black curves) are known from reference measurements or can be approximated by a straight line connecting reference measurements obtained for a very thin surface layer (leftmost black data points in Figure 5.10b,d) and a bulk surface (rightmost black data points in Figure 5.10b,d). Sample measurements yielding data points below the black reference curve (i.e. located within the areas marked by gray colors) thus indicate that subsurface material is probed. Interestingly, when a data point exhibits both a smaller peak height and a smaller peak height ratio than a PMMA bulk surface (i.e. is located within the area marked by the dark gray color), we can conclude that the probed material is below the surface even without reference measurements on thin surface layers. As discussed below for various molecular vibrational bonds, the correlation of peak height ratios and peak heights (Figure 5.10b,d) is a rather general and robust method for distinguishing surface and subsurface layers.

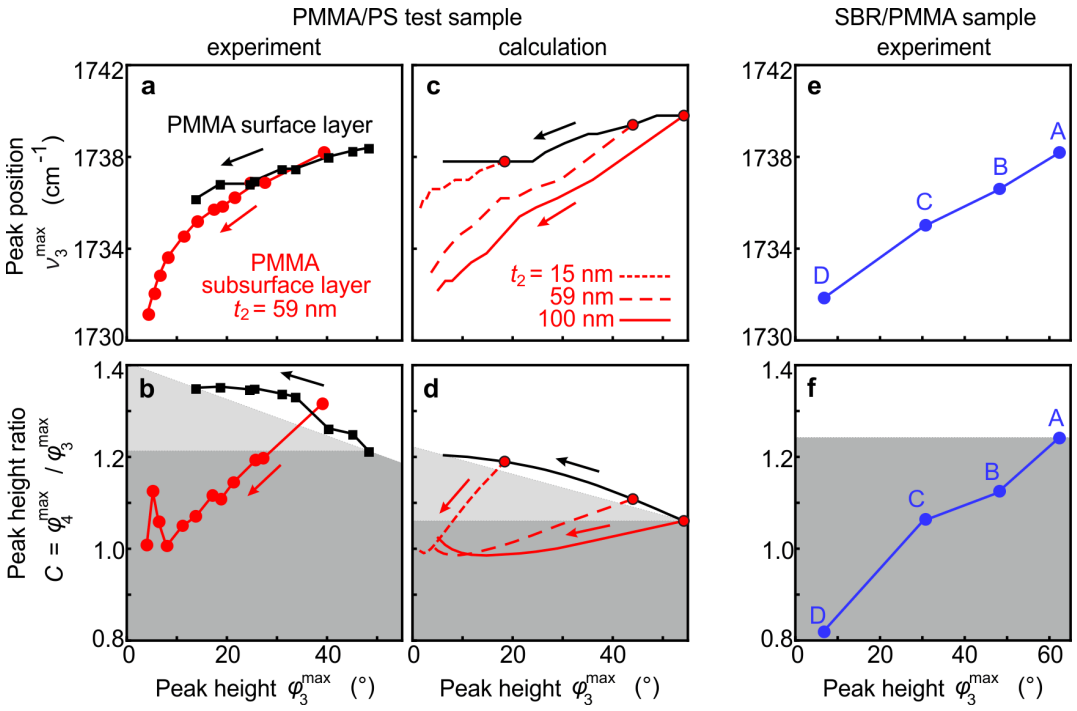

Figure 5.10: Correlation of nano-FTIR peak characteristics. (a) Spectral peak positions ν_3^{max} and (b) peak height ratios C of PMMA surface (black symbols) and PMMA subsurface (red symbols) layers are plotted versus the corresponding peak heights φ_3^{max} (experimental data taken from Figure 5.4). Arrows indicate decreasing PMMA surface layer thickness t_1 (black) and increasing PMMA subsurface layer depth d_2 (red). Subsurface PMMA layer thickness is t_2 = 59 nm. (c,d) Calculation results analogous to panels a and b. Additionally, results for PMMA subsurface layers of thicknesses t_2 = 15 nm (dotted red line) and t_2 = 100 nm (solid red line) are shown. (e) PMMA nano-FTIR peak positions ν_3^{max} and (f) peak height ratios C are plotted versus the corresponding peak heights φ_3^{max} (data measured at positions A-D in Figure 5.3b). (b,d,f) Gray areas indicate the data spaces that correspond to subsurface material.

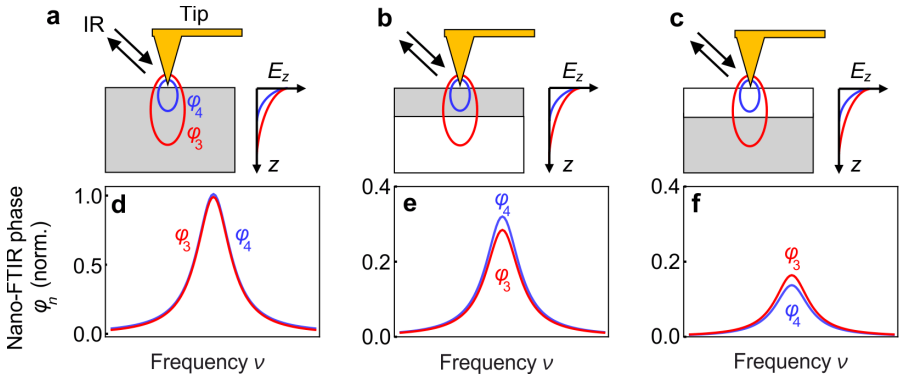

Figure 5.11: Illustration of the peak height ratio criterium. (a-c) Schematic of the nano-FTIR experiment employing different higher harmonic demodulation orders n = 3 (red) and n = 4 (blue) for three samples with different geometries: (a) bulk material, (b) thin surface layers and (c) subsurface layers. Gray areas mark the absorbing material. Ellipses below the tip illustrate the probing volumes. Graphs illustrate the exponential decay of near fields E_z for different demodulation orders. (d-f) Sketch of qualitative nano-FTIR phase spectra, corresponding to panels a-c. For a given n, all φ_n spectra are normalized to φ_n^{max} of bulk.

We apply our findings to clarify the location of PMMA in the SBR/PMMA blend studied in Figure 5.3. To that end, we plotted the spectral peak positions ν_3^{max} and peak height ratios C recorded at positions A to D versus the corresponding peak heights φ_3^{max} (Figure 5.10 panels e,f). We find that the peak position $\nu_3^{max} \approx 1738$ cm^{-1} for the largest peak height φ_3^{max} (position A) agrees well with the peak position of a thick PMMA surface layer (compare Figure 5.10e with Figure 5.10a). Together with the large peak height and the sharp material boundaries at the sample surface observed in the AFM mechanical phase image (see description of Figure 5.3), we conclude that at position A a thick PMMA surface layer is probed. As discussed above, we use the data point recorded at position A as reference measurement to clarify the location of PMMA at the points B to D. The combined reduction of C and φ_3^{max} (relative to position A) at each of the positions B, C and D reliably reveals that a subsurface PMMA layer is probed (as indicated in Figure 5.10f by the dark gray area analogous to Figure 5.10b,d). This conclusion is supported in Figure 5.10e, where we observe strong spectral red-shifts down to $\nu_3^{max} = 1732$ cm^{-1} as the peak height decreases (positions B-D), which is much stronger than that for thin PMMA surface layers (black dots in Figure 5.10a and Mastel et al.[18]).

We note that for the discrimination of surface and subsurface layers one could apply nano-FTIR peak ratios obtained from other demodulation orders n (for example the ratios $\varphi_4^{max}/\varphi_2^{max}$ or $\varphi_3^{max}/\varphi_2^{max}$, see Figure 5.12), as far as the respective near-field signals are background free and of sufficiently large signal-to-noise ratio.

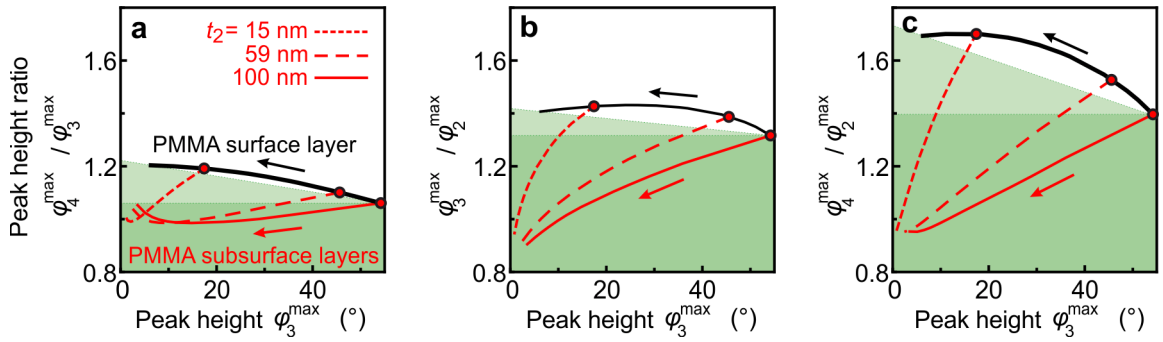

Figure 5.12: Comparison of calculated peak height ratios for different signal demodulation orders. (a) $\varphi_4^{max}/\varphi_3^{max}$, (b) $\varphi_3^{max}/\varphi_2^{max}$ and (c) $\varphi_4^{max}/\varphi_2^{max}$ of PMMA surface (black curve) and PMMA subsurface (red curves) layers are plotted versus the corresponding peak heights φ_3^{max}. Arrows indicate decreasing PMMA surface layer thickness t_1 (black) and increasing PMMA subsurface layer depth d_2 (red). Subsurface PMMA layer thicknesses are t_2 = 15 nm (dotted red line), t_2 = 59 nm (dashed red line) and t_2 = 100 nm (solid red line). (a-c) Green areas indicate the data spaces that correspond to subsurface material. The figure shows that peak height ratios obtained from various harmonics can be used to distinguish whether and infrared absorbing layer is at the surface or below the surface.

5.4 Discussion

We have chosen to study the nano-FTIR peak characteristics of the C=O bond, as it represents a typical molecular vibration. Being able to describe this vibration by a Lorenz oscillator model, as most other molecular vibrational bonds, our findings regarding peak shifts and peak height ratios can be assumed to be valid for most molecular vibrational bonds. To corroborate this assumption, we performed a largely extended study. All results of this study are presented in the Appendix 6.4 (Appendix Figures Figure 6.2 to Figure 6.10). In the following we briefly outline the study and summarize and discuss the main results.

Appendix Figure 6.2 to Figure 6.4 present calculations of the momentum-dependent Fresnel reflection coefficient, nano-FTIR peak shifts and peak height ratios for various C-C-O and C-O-C bonds of surface and subsurface PMMA layers between 1100 cm^{-1} and 1300 cm^{-1}. The corresponding molecular vibrations differ not only regarding the chemical bonding, but also in oscillator strength, and partially overlap spectrally. Analogous to Appendix Figure 6.2 to Figure 6.4, the Appendix Figure 6.5 to Figure 6.6 show results obtained for surface and subsurface polyethylene-oxide (PEO) layers, which exhibit three C-O stretching modes of different oscillator strengths. The calculations are complemented by experimental results in the Appendix Figure 6.7. We also calculated peak shifts and peak height ratios for surface and subsurface layers modelled by a Lorenz oscillator with different high-frequency permittivity (Appendix Figure 6.8). Finally, the nano-FTIR peak shifts and peak height ratios of the C=O bond of PMMA subsurface layers are studied as a function of layer depth d_2 and thickness t_2 (Appendix Figure 6.9) and in dependence of the permittivity of the capping layer (Appendix Figure 6.10).

From the results presented in Appendix 6.4 the following general conclusions can be derived: (1) nano-FTIR peak positions of subsurface layers are shifted to lower frequencies (red-shift) compared to that of surface layers of the same thickness. With increasing depth d_2 of the subsurface layer, the red-shift increases. The amount of the red-shift, however, strongly depends on the oscillator strength and can vary from being negligibly small (<1 cm^{-1}) to several wavenumbers, similar to the C=O bond of PMMA. (2) Most interesting and important, the peak height ratios $C = \varphi_4^{max}/\varphi_3^{max}$ observed for all studied molecular vibrations behave nearly the same as that of the C=O peak, and thus can be considered as a rather robust criterium for distinguishing surface and subsurface layers. (3) With decreasing thickness t_2 of the subsurface layer or increasing permittivity of the capping layer, the peak heights and spectral peak shifts reduce, which in turn reduces the depths d_2 at which a nano-FTIR peak can be practically detected. Generally, and as is the case for any other measurement technique, our results can be applied only for the case that an absorption peak shows sufficient signal-to-noise ratio in the nano-FTIR spectrum and that the peak shifts are large enough to be resolved by typical nano-FTIR instrumentation.

5.5 Conclusions

In summary, we found that the peaks in nano-FTIR phase spectra of subsurface organic layers are spectrally red-shifted compared to nano-FTIR spectra of the corresponding bulk material, and that the red-shift is stronger than the one observed for surface layers when their thickness is reduced.[18] We corroborate our results with a semi-analytical model for calculating nano-FTIR spectra of multi-layered samples, which well describes the observed trends. Our model also reveals that peak shifts in nano-FTIR spectra of multi-layer samples can be traced back to the sample´s momentum-dependent Fresnel reflection coefficient $\beta(\nu,q)$, provided that chemically induced peak shifts can be excluded. We note that such sample- and momentum determined peak shifts are not an exotic feature of near-field spectroscopy, but also occur in far-field spectroscopy, where the probing momentum is determined by the angle of incidence. We finally demonstrated that surface and subsurface layers can be differentiated by analyzing the ratio of peak heights obtained at different demodulation orders n, without the need of theoretical modelling or simulations. Our results will be thus important for the future practical application of nano-FTIR spectroscopy, for example, to distinguish peak shifts caused by sample geometry from peak shifts that are caused by chemical effects such as chemical interaction at material boundaries.

6 Appendix

6.1 Spectral contrast enhancement factors of PEO on Quartz for different normalization procedures

We performed simulations to corroborate the validity of our procedure that is used in chapter 4 for determining the molecular vibrational contrast *C* of a thin PEO layer on quartz. We recall that in Figures Figure **4.5**, Figure **4.6** and Figure **4.8** the pure quartz spectrum was scaled to match the spectrum of PEO on quartz in a spectral region outside the PEO vibrational spectral range (black curve in Figure 6.1a). We then subtracted the quartz spectrum from the PEO on quartz spectrum to obtain Δs_4 and *C*. This procedure is most straight forward, as it does not require demanding fitting of the experimental spectra. However, it neglects the spectral shift of the polaritonic tip-substrate resonance that occurs when the tip-substrate distance is increased[102,103]. We validate the reliability of this procedure by calculating the quartz spectrum when a thin layer is on top of the quartz surface, with a layer thickness corresponding to that of the PEO layer and a permittivity corresponding to that of the PEO layer without the molecular vibrational feature. We assume different values for the PEO permittivity: ϵ_{PEO} = 2.0 (green spectrum in Figure 6.1a), 1.7 (dashed green spectrum) and 1.4 (dotted green spectrum). The higher and lower considered values correspond to the permittivity at 1050 cm^{-1} and at 1300 cm^{-1}, while the third one is their average. That way the spectral shift is considered and can be observed by comparing the black and green spectra in Figure 6.1a. Subtracting the differently normalized quartz spectra (black and green) from the PEO on quartz spectrum (red), we obtain the spectral contrast Δs_4 (not shown) from which we can determine *C*, the latter shown in Figure 6.1b. The variation of *C* (green shaded area in Figure 6.1b) is significantly smaller than the 300% enhancement of the spectral contrast of PEO on quartz compared to the spectral contrast of PEO on gold. For smaller PEO thicknesses the variation of *C* reduces, while for larger PEO thicknesses it increases. This observation can be better appreciated by plotting the ratio $C_{c\text{-}SiO2}(d)/C_{Au}(d)$ in Figure 6.1c. We note that polariton-resonant tip-substrate coupling will be most beneficial for thin layers below 10 nm thickness, where the variation caused by our normalization procedures reduces.

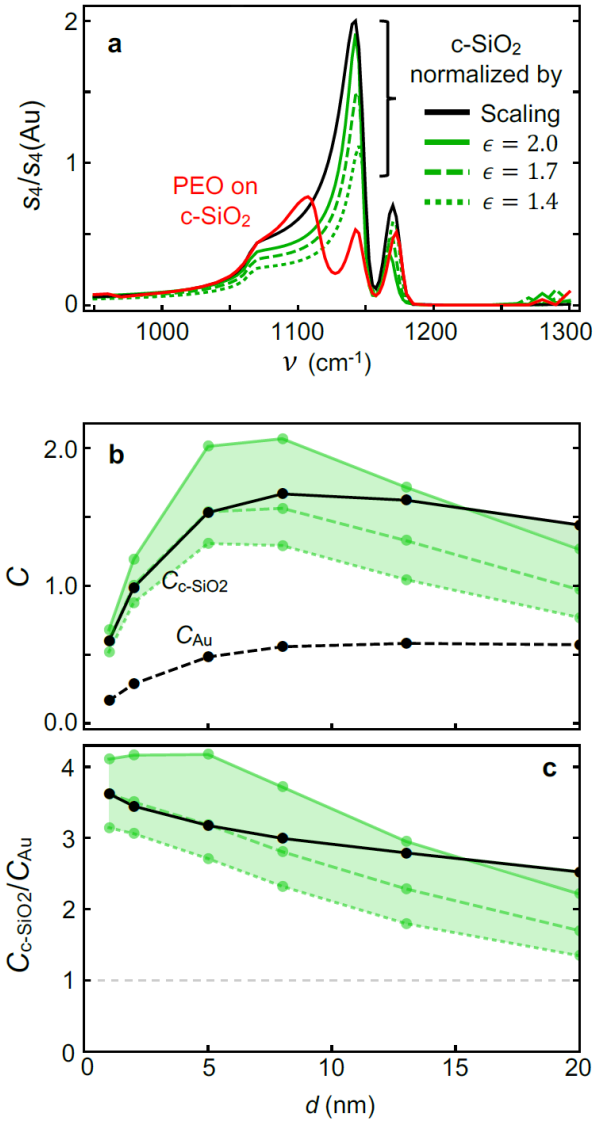

Figure 6.1: Variation of enhancement factor *C* for different normalization procedures. (a) Calculated nano-FTIR amplitude spectra of 13 nm-PEO on c-SiO_2 (red), in comparison with c-SiO_2 spectra normalized in different ways: Scaling as in the main text (black) and by calculating the c-SiO_2 spectrum with a 13 nm-thick dielectric layer of permittivity ϵ_{PEO} = 2.0 (solid green), ϵ_{PEO} = 1.7 (dashed green) and ϵ_{PEO} = 1.4 (dotted green). The latter three curves account for spectral shifts of the phonon resonance due to increased tip-substrate distance. (b) Maximum spectral contrast for differently thick PEO layers on quartz and Au, $C_{c\text{-}SiO2}$ and C_{Au}, obtained for the different normalization procedures of the pure c-SiO_2 spectra according to panel a. (c) Ratios $C_{c\text{-}SiO2}/C_{Au}$.

6.2 Green's function of an electric dipole above a sample

The PDM for layered samples involves using the dyadic Green's function of an electric dipole located above a multi-layered sample.[51] The Green's function $\boldsymbol{G}$ at point $\boldsymbol{r} = (x,y,z)$ relates to the electric field via $\boldsymbol{E}(\boldsymbol{r},\boldsymbol{r_0}) = \boldsymbol{G}(\boldsymbol{r},\boldsymbol{r_0})\boldsymbol{p}$, which can be separated into a direct part $\boldsymbol{G_0}$ (describing the primary electric field produced by the dipole) and a reflected part $\boldsymbol{G_{refl}}$ (describing the electric field that is reflected at the sample surface).[10] For modelling the near-field interaction between a nano-FTIR tip and the sample, only the reflected part of the Greens function is needed.[51] For an arbitrarily oriented dipole $\boldsymbol{p}$ located at $\boldsymbol{r_0} = (x_0,y_0,z_0)$ and in cartesian coordinates in momentum-space ($\boldsymbol{k} = (k_x,k_y,k_z)$ with $|\boldsymbol{k}| = \frac{\omega}{c} = \sqrt{k_x^2+k_y^2+k_z^2}$) the reflected Green's function $\boldsymbol{G_{refl}}$ is given by[10]

$$\boldsymbol{G_{refl}}(\boldsymbol{r},\boldsymbol{r_0}) = \frac{i\omega^2\mu_0\mu_1}{8\pi^2}\iint_{-\infty}^{\infty}\left[\boldsymbol{M^s_{refl}}+\boldsymbol{M^p_{refl}}\right]e^{i[k_x(x-x_0)+k_y(y-y_0)+k_{z1}(z+z_0)]}dk_x dk_y \tag{6.1}$$

$$\boldsymbol{M^s_{refl}} = \frac{r_s(k_x,k_y)}{k_{z1}(k_x^2+k_y^2)}\begin{bmatrix} k_y^2 & -k_xk_y & 0 \\ -k_xk_y & k_x^2 & 0 \\ 0 & 0 & 0 \end{bmatrix} \tag{6.2}$$

$$\boldsymbol{M^p_{refl}} = \frac{-r_p(k_x,k_y)}{k_1^2(k_x^2+k_y^2)}\begin{bmatrix} k_x^2k_{z1} & k_xk_yk_{z1} & k_x(k_x^2+k_y^2) \\ k_xk_yk_{z1} & k_y^2k_{z1} & k_y(k_x^2+k_y^2) \\ -k_x(k_x^2+k_y^2) & -k_y(k_x^2+k_y^2) & -\left(k_x^2+k_y^2\right)^2/k_{z1} \end{bmatrix}. \tag{6.3}$$

Accounting for the geometry of the point dipole model, Equations (6.1) to (6.3) are simplified in the following by using that only the reflected field at the position $\boldsymbol{r} = \boldsymbol{r_0}$ of the point dipole yields additional polarization of the probing tip. At the position of the dipole itself ($\boldsymbol{r} = \boldsymbol{r_0}$) and in cylindrical coordinates in momentum-space ($\boldsymbol{k} = (q,k_\varphi,k_z)$ with $q = \sqrt{k_x^2+k_y^2}$) the reflected Green's function simplifies to

$$\boldsymbol{G_{refl}}(\boldsymbol{r_0},\boldsymbol{r_0}) = \frac{i\omega^2\mu_0\mu_1}{8\pi^2}\int_0^{\infty}dq\,q\int_0^{2\pi}dk_\varphi\,\left[\boldsymbol{M^s_{ref}}+\boldsymbol{M^p_{refl}}\right]e^{i2k_{z1}z_0} \tag{6.4}$$

$$\boldsymbol{M^s_{refl}} = \frac{r_s(q)}{k_{z1}q^2}\begin{bmatrix} q^2\sin^2\varphi & -q^2\cos\varphi\sin\varphi & 0 \\ -q^2\cos\varphi\sin\varphi & q^2\cos^2\varphi & 0 \\ 0 & 0 & 0 \end{bmatrix} \tag{6.5}$$

$$\boldsymbol{M^p_{ref}} = \frac{-r_p(q)}{k_1^2q^2}\begin{bmatrix} q^2\cos^2\varphi\,k_{z1} & q^2\cos\varphi\sin\varphi\,k_{z1} & q^3\cos\varphi \\ q^2\cos\varphi\sin\varphi\,k_{z1} & q^2\sin^2\varphi\,k_{z1} & q^3\sin\varphi \\ -q^3\cos\varphi & -q^3\sin\varphi & -q^4/k_{z1} \end{bmatrix}. \tag{6.6}$$

Owing to the rotational symmetry of the problem, the angular momentum-integral over k_φ can be directly integrated, yielding the expression of the reflected Green's function that is used in the main text as Equations (3.15) to (3.17).

6.3 Reflected electric field of an electric monopole above a sample

As explained in chapters 3.4.3 and 5.2.3, the FDM describes the tip-sample interaction in a simple image charge model: The tip produces an electric field distribution similar to that of a charge Q_0, which induces a mirror charge Q_0' in the sample (i.e. for bulk samples $Q_0' = -\beta Q_0$), which then acts back onto the tip (Equation (3.22)). In order to derive an effective $\bar{\beta}$, such that the image charge of Q_0 in multilayered samples is described by $Q_0' = -\bar{\beta} Q_0$, we analyse and compare the electric field distributions produced by Q_0 and Q_0', the latter corresponding to the field of Q_0 after reflection at the sample surface (method of image charges[57]).

We express in the following (i) the electric field $\boldsymbol{E}$ of the monopole Q_a (in the absence of a sample) in the angular spectrum representation[10] and (ii) the electric field reflected from the multilayered sample, $\boldsymbol{E}_{\mathbf{refl}}$, from which we derive (iii) the effective (momentum-integrated) near-field reflection coefficient $\bar{\beta}$ that is used in chapter 5. Such treatment fully accounts for the evanescent part of the plane wave spectrum necessary for proper description of the near-field tip-sample interaction.

(i) Electric monopole field

The electric field of a point charge $Q_a e^{-i\omega t}$ (located in the origin of a coordinate system) is given at an arbitrary point $\boldsymbol{r} = (x,y,z)$ in space by[133]

$$\boldsymbol{E}(\boldsymbol{r}) = -\nabla\Phi = -\frac{Q_a}{4\pi\epsilon_0}\nabla\frac{e^{i\boldsymbol{k}\cdot\boldsymbol{r}}}{r}, \tag{6.7}$$

where Φ is the electric potential of the point charge, the nabla operator is given by $\nabla = (\frac{\partial}{\partial x}, \frac{\partial}{\partial y}, \frac{\partial}{\partial z})$ and the oscillation frequency ω is related to the electromagnetic wave momentum $k = \omega/c$. We obtain the angular spectrum representation of Equation (6.7) by using the Weyl identity,[10]

$$\frac{e^{i\boldsymbol{k}\cdot\boldsymbol{r}}}{r} = \frac{i}{2\pi}\iint_{-\infty}^{\infty}\frac{e^{ik_x x + ik_y y + ik_z z}}{k_z}\,dk_x dk_y, \tag{6.8}$$

yielding for the electric field of the monopole field

$$\boldsymbol{E}(\boldsymbol{r}) = -\frac{Q_a}{4\pi\epsilon_0}\nabla\frac{i}{2\pi}\iint_{-\infty}^{\infty}\frac{e^{ik_x x + ik_y y + ik_z z}}{k_z}\,dk_x dk_y$$

$$= \frac{Q_a}{8\pi^2\epsilon_0}\iint_{-\infty}^{\infty}\frac{e^{ik_x x+ik_y y+ik_z z}}{k_z}\begin{pmatrix}k_x\\k_y\\k_z\end{pmatrix}dk_x dk_y. \tag{6.9}$$

For simplicity, we restrict ourselves to analyzing the z-component E_z of the electric field along the z-axis ($x = 0$, $y = 0$), which we justify by the elongated shape of the probing tip (providing near fields below the tip apex that are essentially polarized along the z-direction) and the rotational symmetry of the problem:

$$E_z(0,0,z) = \frac{Q_a}{8\pi^2\epsilon_0}\iint_{-\infty}^{\infty}\frac{e^{ik_z z}}{k_z}k_z\,dk_x dk_y. \tag{6.10}$$

The FDM models the nano-FTIR probing tip as a prolate spheroid of length $2L$, which is much shorter than the wavelength of infrared radiation used in our experiments. Thus, we further simplify Equation (6.10) by taking the electrostatic limit (which leads to the condition $k_z = i\sqrt{k_x^2+k_y^2}$):

$$E_z(z) = \frac{Q_a}{8\pi^2\epsilon_0}\iint_{-\infty}^{\infty}e^{-(k_x^2+k_y^2)z}\,dk_x dk_y. \tag{6.11}$$

We obtain our final expression for $E_z(z)$ after coordinate transformation from cartesian coordinates (k_x,k_y,k_z) to cylindrical coordinates ($q = \sqrt{k_x^2+k_y^2}$, k_φ, k_z) and integration over k_φ:

$$E_z(z) = \frac{Q_a}{4\pi\epsilon_0}\int_0^{\infty}qe^{-qz}\,dq. \tag{6.12}$$

As consistency check, we perform the integration over q and reproduce the typical z^{-2} dependence for the electric monopole field:

$$E_z(z) = \frac{Q_a}{4\pi\epsilon_0}\frac{1}{z^2}. \tag{6.13}$$

(ii) Reflected electric monopole field

We now derive the field after reflection from the (multilayer) sample surface, starting from Equation (6.12). The monopole field is purely p-polarized (due to the rotational symmetry of the problem), which allows us to express all reflections at the sample surface by the quasi-electrostatic Fresnel reflection coefficient for p-polarized light $\beta(q)$ which is given in Equation (5.6). As illustrated in Figure 5.6b (red dashed arrow), the electric monopole field extends from the position of the monopole to the sample surface (yielding the term $\exp(-qz_a)$ with $z_a=H+a$), where it is reflected via $\beta(q)$ and extends back to arbitrary z (yielding $\exp(-qz)$). The reflected

electric field of the monopole Q_a at the position z (measured from the sample surface) is thus given by

$$E_{z,\mathrm{refl}}(z) = \frac{Q_a}{4\pi\epsilon_0}\int_0^\infty q e^{-qz_a}\beta(q)e^{-qz}\,dq. \tag{6.14}$$

(iii) Reflection coefficient $E_{z,\mathrm{refl}}(z)/E_z(z)$

In order to obtain the momentum-integrated near-field reflection coefficient for multilayer samples, we calculate the ratio $E_{z,\mathrm{refl}}(z)/E_z(z')$, where $E_z(z')$ is the electric field distribution produced by an effective point charge Q_a and $E_{z,\mathrm{refl}}(z)$ is the electric field distribution produced by Q_a that is reflected at the multi-layered sample surface. We distinguish z and z' in order to remind that the origin of the nominator (z = 0) lies in the sample surface plane (Equation (6.14)), while in the denominator the origin (z' = 0) lies in the monopole Q_a (which is located at a height $z_a = H + a$ above the sample surface plane, Equation (6.12)). By using Equations (6.12) and (6.14) we obtain

$$\frac{E_{z,\mathrm{refl}}(z)}{E_z(z')} = \frac{\int_0^\infty \beta(q) q e^{-qz_a} e^{-qz} dq}{\int_0^\infty q e^{-qz'}\,dq}. \tag{6.15}$$

Note that Equation (6.15) is independent of the momentum q (after integration).

In principle, Equation (6.15) can be evaluated at arbitrary z, however, in order to describe the tip-sample interaction, we make an approach similar to Aizpurua et al.[51] and Fei et al.[66] and evaluate the reflected field at the position of the charge Q_a itself, $E_{z,\mathrm{refl}}(z=z_a)$, which we compare with the (incident) monopole field $E_z(z = 2z_a)$, ensuring that we evaluate the incident and reflected field at the same distance from the respective charges (mirror charge in case of the reflected field). We thus define the effective near-field reflection coefficient (which is valid at the position of Q_a) as

$$\frac{E_{z,\mathrm{refl}}(z = z_a)}{E_z(z' = 2z_a)} = \frac{\int_0^\infty \beta(q) q e^{-2qz_a}\,dq}{\int_0^\infty q e^{-2qz_a}\,dq} =: \bar{\beta} \tag{6.16}$$

We note that the integral in the nominator of Supplementary Equation (6.16) contains a coupling weight function (used in chapter 5 as Equation (5.7)) that is proportional to q, similar to expressions found in the work of Hauer et al.[54] On the other hand, a q^2-dependency is found in similar momentum-integrals contained in the point dipole model for multi-layered samples[51] and the lightning rod model[58,59], as they are derived from a reflected dipole field, rather than a reflected monopole field.

6.4 Generality of subsurface peak shifts and the peak height ratio criterium

6.4.1 Various (partially spectrally overlapping) vibrational modes of PMMA

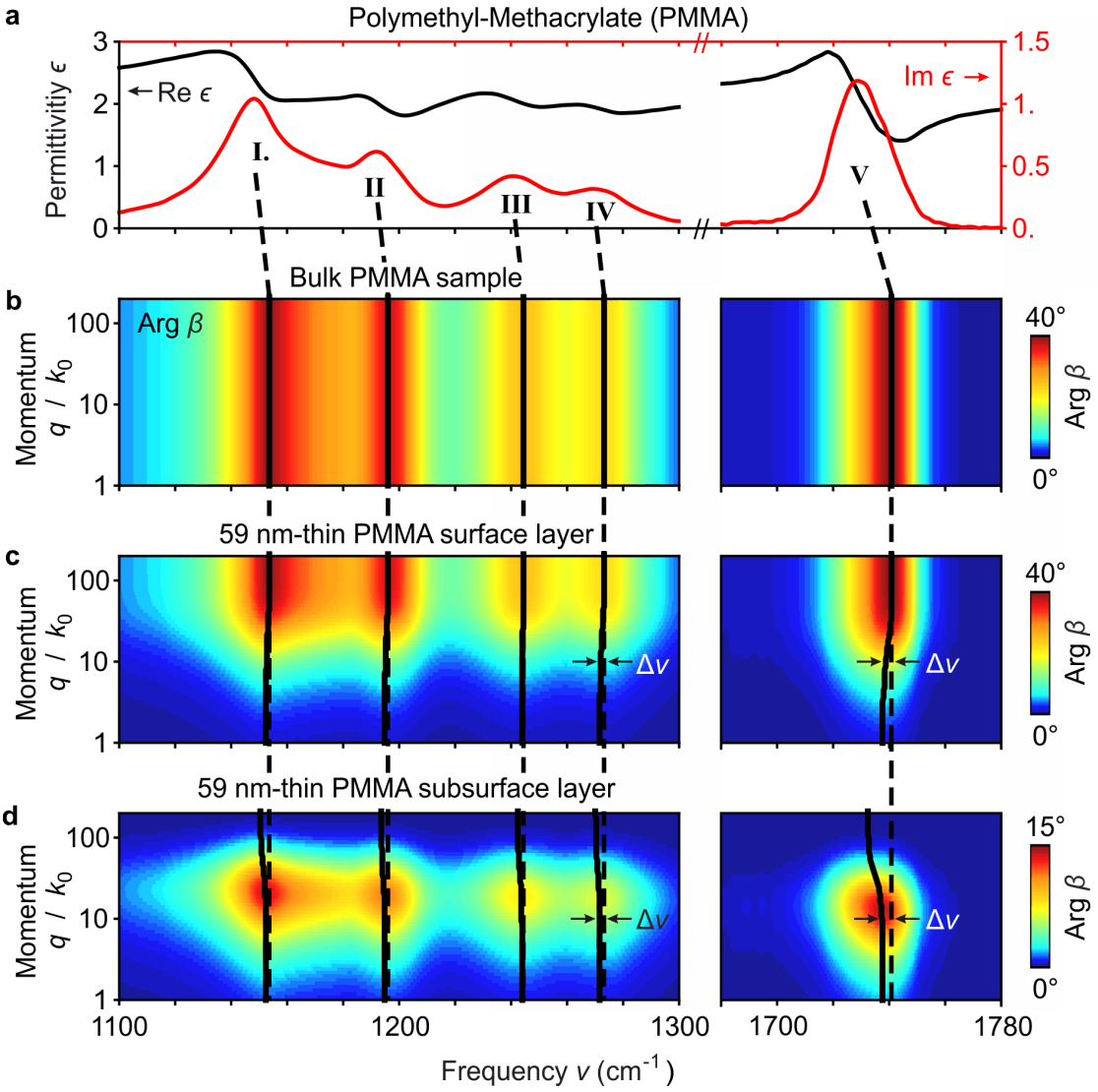

Figure 6.2: Momentum-dependent spectral peak shifts in Fresnel reflection coefficient for various (partially spectrally overlapping) vibrational modes of PMMA. (a) Real (black) and imaginary (red) parts of the dielectric function of PMMA. Peaks in Im[ϵ] correspond to the asymmetric C-O-C (marked I and II), the symmetric C-C-O (marked III and IV) and the C=O (marked V) vibrational stretching modes respectively. (b-d) Phase of the quasi-electrostatic Fresnel reflection coefficient (Arg β) as a function of frequency ν and momentum q for (b) bulk PMMA, (c) a t_1 = 59 nm-thin surface PMMA layer and (d) a t_2 = 59 nm-thin subsurface PMMA layer located at depth d_2 = 20 nm below PS. Both layers in (c,d) are placed on a silicon substrate. The continuous black lines indicate the frequencies where Arg β has its maxima. The dashed vertical lines mark the maxima of bulk PMMA and act as reference frequencies for determining the peak-shifts $\Delta\nu$. The figure shows that: (*1*) all peaks of thin PMMA surface layers shift to lower frequencies (red-shift) with decreasing momenta. (*2*) all peaks of PMMA subsurface layers red-shift with increasing momenta. (*3*) The red-shift is stronger for subsurface layers as compared to surface layers. (*4*) Importantly, the peak shifts occur for weaker and partially spectrally overlapping peaks (I-IV), as well as for the isolated and strong peak (V). Zoom-ins of the panels (c,d) are provided in Figure 6.3.

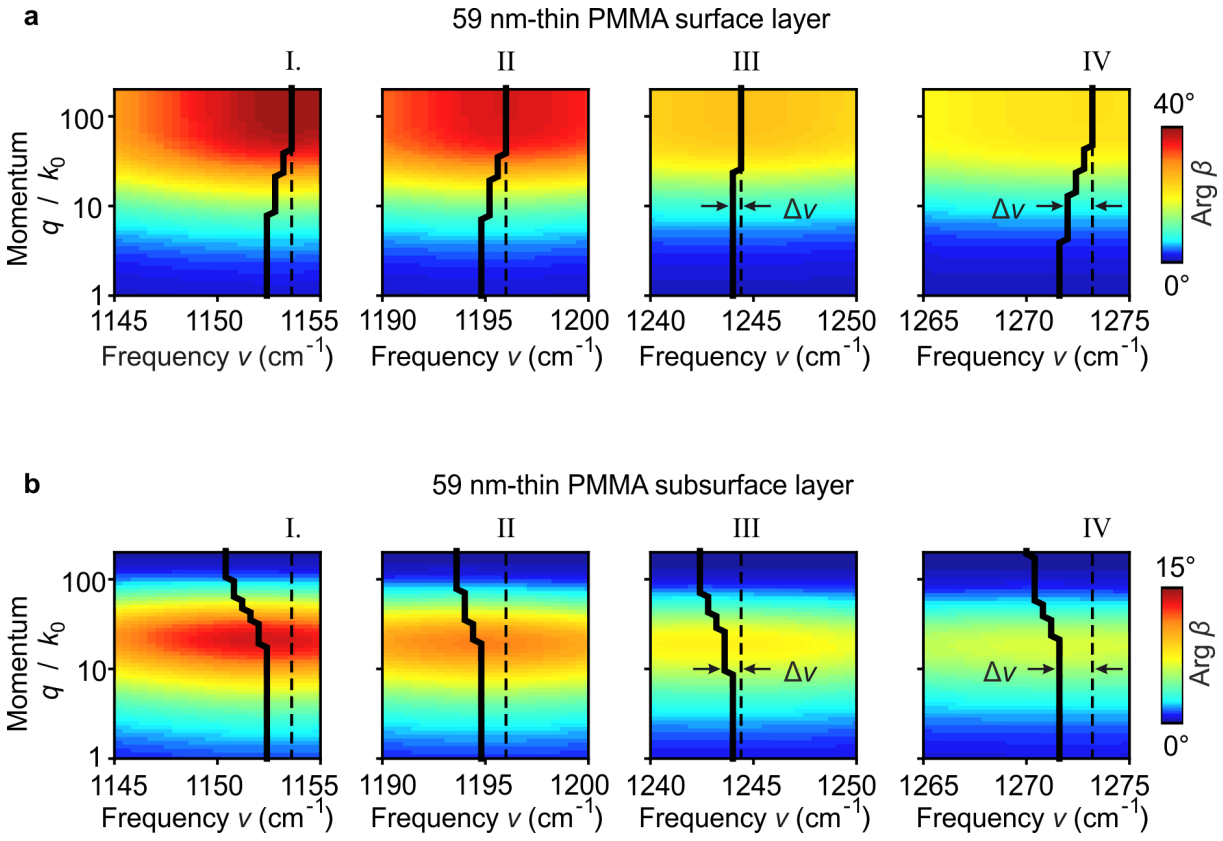

Figure 6.3: Zoom-in to Figure 6.2c,d.

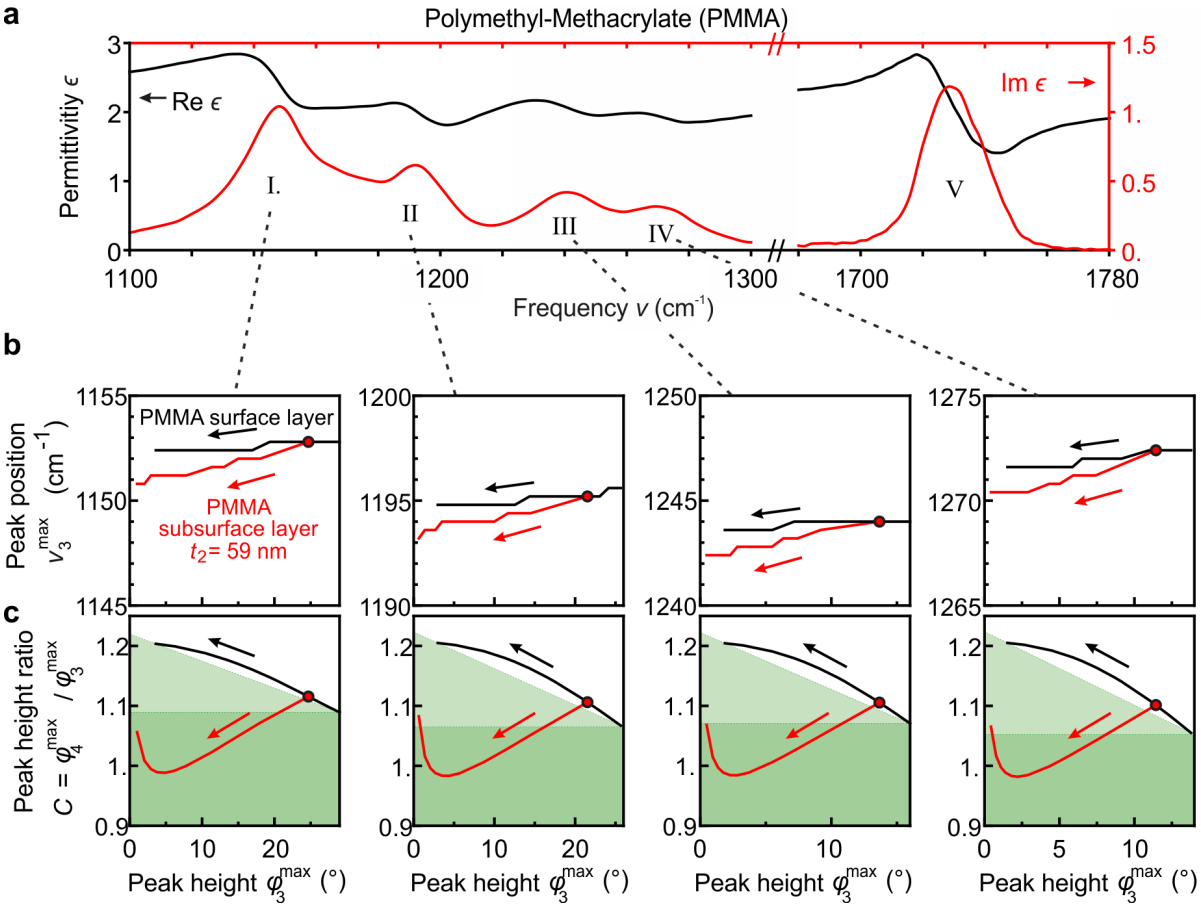

Figure 6.4: Correlation of nano-FTIR peak characteristics for various (partially spectrally overlapping) vibrational modes of PMMA. (a) Real (black) and imaginary (red) parts of the dielectric function of PMMA. Peaks in Im[ϵ] correspond to the asymmetric C-O-C (marked I and II), the symmetric C-C-O (marked III and IV) and the C=O (marked V) vibrational stretching modes respectively. (b) Calculated spectral peak positions ν_3^{max} and (c) peak height ratios C of PMMA surface (black symbols) and PMMA subsurface (red symbols) layers are plotted versus the corresponding peak heights φ_3^{max}, for the vibrational modes I-IV of PMMA. Arrows indicate decreasing PMMA surface layer thickness t_1 (black) and increasing PMMA subsurface layer depth d_2 (red). Subsurface PMMA layer thickness is t_2 = 59 nm. Green areas in (c) indicate the data spaces that correspond to subsurface material. The figure shows for various (partially spectrally overlapping) vibrational modes of PMMA that: (*1*) nano-FTIR peak positions shift to lower frequencies (red-shift) when the thickness t_1 of a surface layer decreases or when the depth d_2 of a subsurface layer increases. (*2*) The red-shift is stronger for subsurface layers as compared to surface layers. (*3*) Most interesting and important, the peak height ratios $C = \varphi_4^{max}/\varphi_3^{max}$ observed for all molecular vibrations of PMMA behave nearly the same as that of the C=O peak (Figure 5.10), and thus can be considered as a rather robust criterium for distinguishing surface and subsurface layers.

6.4.2 Differently strong vibrational modes of PEO

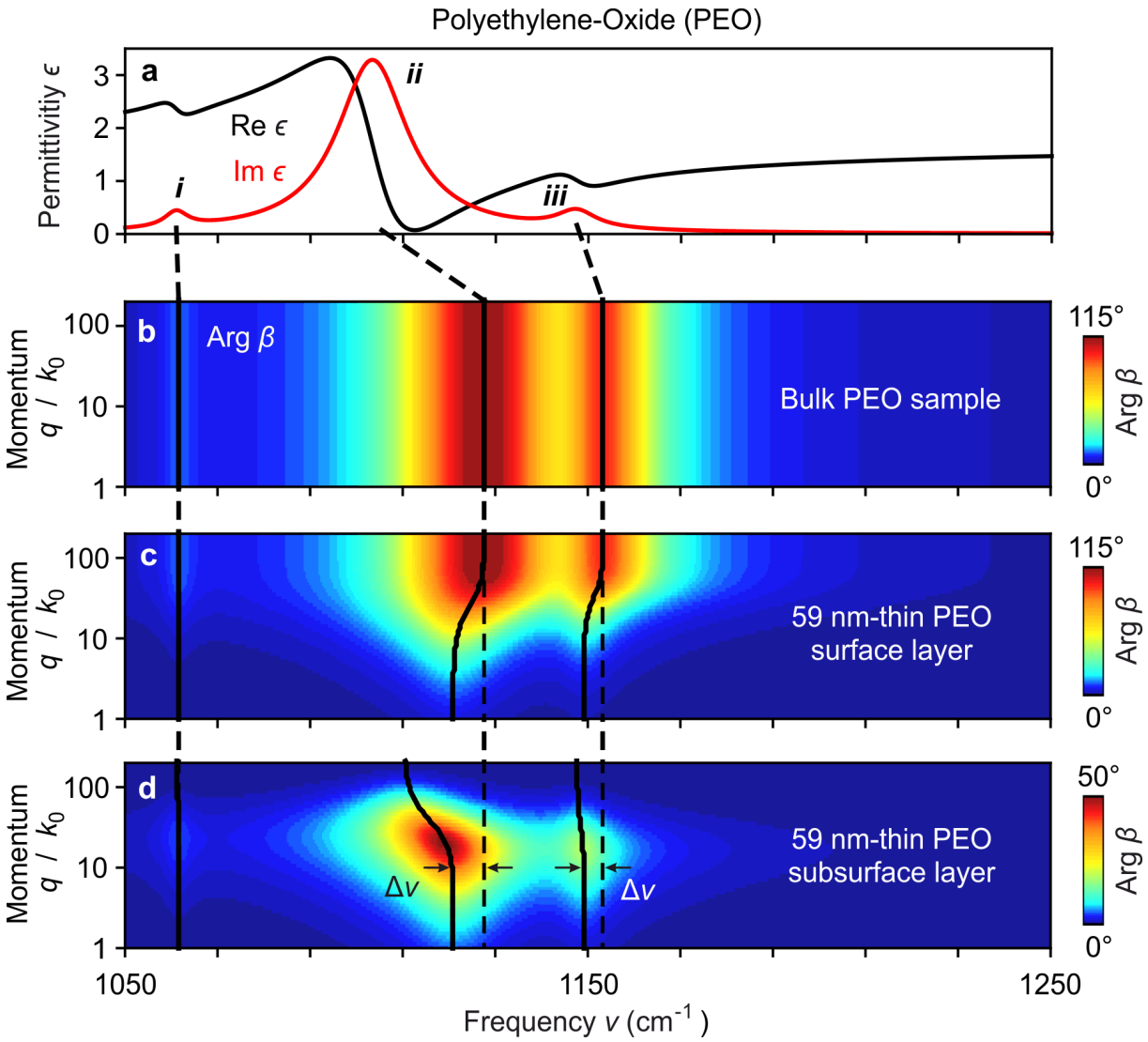

Figure 6.5: Momentum-dependent spectral peak shifts in Fresnel reflection coefficient for differently strong vibrational modes of Polyethylene-oxide (PEO). (a) Real (black) and imaginary (red) parts of the dielectric function of PEO. Peaks in Im[ϵ] (marked *i*-*iii*) correspond to C-O stretching modes. (b-d) Phase of the quasi-electrostatic Fresnel reflection coefficient (Arg β) as a function of frequency ν and momentum q for (b) bulk PEO, (c) a t_1 = 59 nm-thin surface PEO layer and (d) a t_2 = 59 nm-thin subsurface PEO layer located at depth d_2 = 20 nm below PS. Both layers in (c,d) are placed on a silicon substrate. The continuous black lines indicate the frequencies where Arg β has its maxima. The dashed vertical lines mark the maxima of bulk PEO and act as reference frequencies for determining the peak-shifts $\Delta\nu$. The figure shows (for other peaks than of PMMA) that: (*1*) peaks of thin PEO surface layers shift to lower frequencies (red-shift) with decreasing momenta. (*2*) peaks of PEO subsurface layers red-shift with increasing momenta. (*3*) The red-shift is stronger for subsurface layers as compared to surface layers. (*4*) The magnitude of $\Delta\nu$ largely varies from peak to peak and is not directly related to the strength of a vibrational mode; i.e. the bonds *i* and *iii* are similar in Im[ϵ] but different in $\Delta\nu$, on the other hand, the bonds *ii* and *iii* are similar in $\Delta\nu$ but different in Im[ϵ].

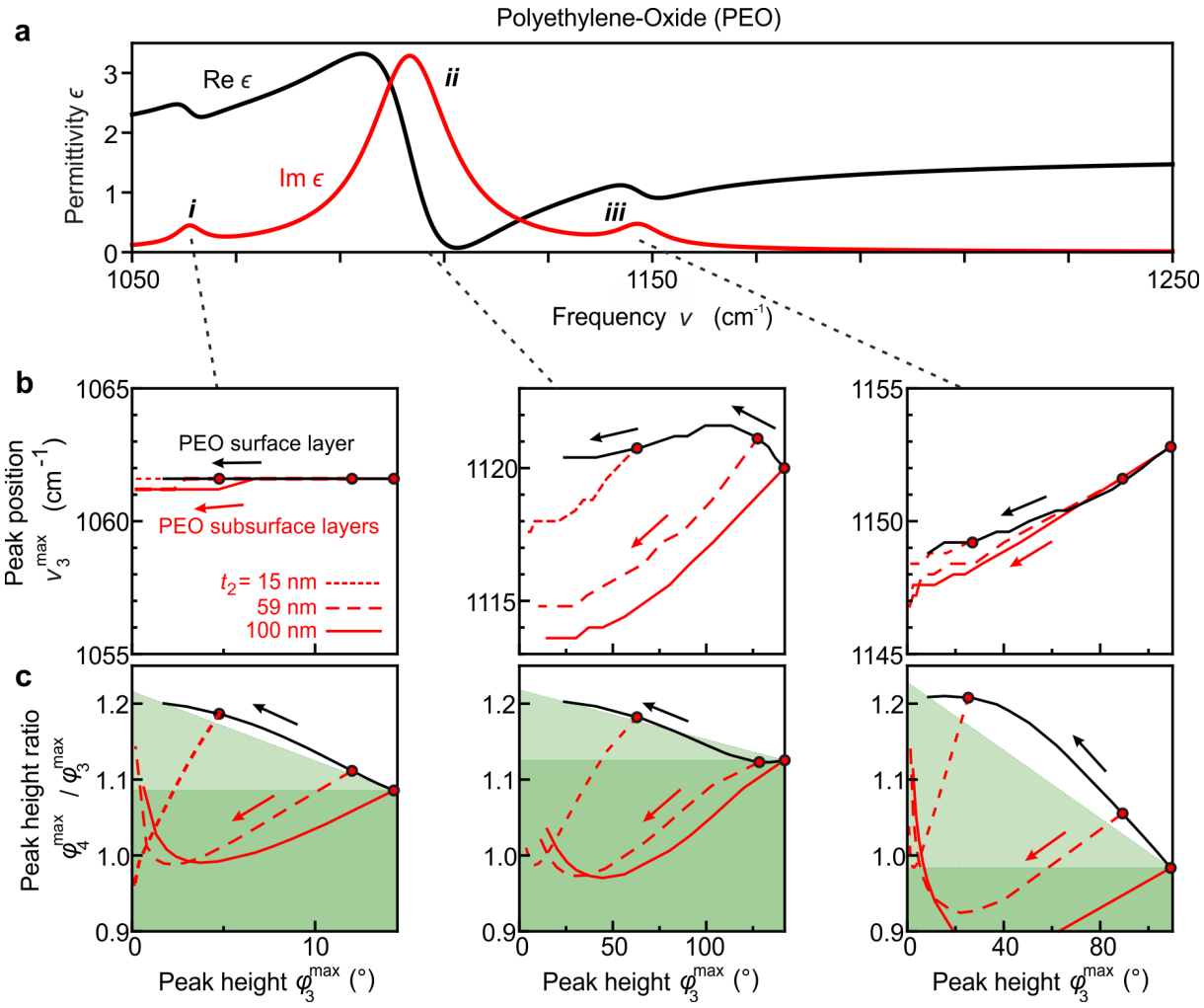

Figure 6.6: Correlation of nano-FTIR peak characteristics for various (differently strong) vibrational modes of PEO. (a) Real (black) and imaginary (red) parts of the dielectric function of PEO. Peaks in Im[ϵ] (marked *i-iii*) correspond to C-O vibrational stretching modes. (b) Calculated spectral peak positions ν_3^{max} and (c) peak height ratios C of PEO surface (black symbols) and PEO subsurface (red symbols) layers are plotted versus the corresponding peak heights φ_3^{max}, for the vibrational modes *i-iii* of PEO. Arrows indicate decreasing PEO surface layer thickness t_1 (black) and increasing PEO subsurface layer depth d_2 (red). Subsurface PEO layer thicknesses are t_2 = 15 nm (dotted red line), t_2 = 59 nm (dashed red line) and t_2 = 100 nm (solid red line). Green areas in (c) indicate the data spaces that correspond to subsurface material. The figure shows for differently strong vibrational modes of PEO that: (*1*) nano-FTIR peak positions shift to lower frequencies (red-shift) when the thickness t_1 of a surface layer decreases or when the depth d_2 of a subsurface layer increases. (*2*) The red-shift is stronger for subsurface layers as compared to surface layers. (*3*) Most interesting and important, the peak height ratios $C = \varphi_4^{max}/\varphi_3^{max}$ observed for all molecular vibrations of PEO behave nearly the same as that of the C=O peak of PMMA (Figure 5.10), and thus can be considered as a rather robust criterium for distinguishing surface and subsurface layers.

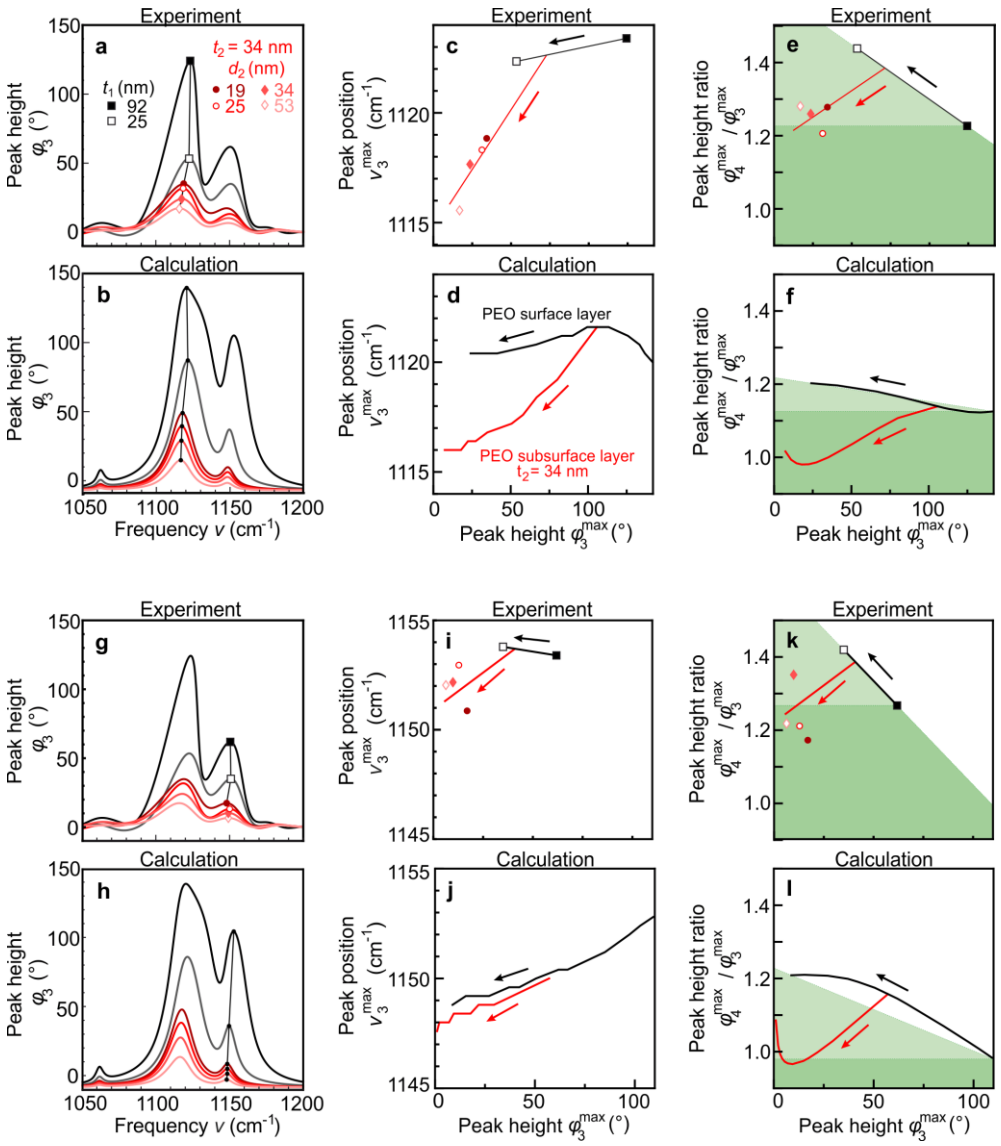

Figure 6.7: Comparison of experimental and calculated nano-FTIR peak characteristics for PEO. (a) Experimental and (b) calculated nano-FTIR phase spectra of PEO surface layers with thickness t_1 = { 25, 92 } nm (black symbols) and PEO subsurface layers with average thickness t_2 = 34 nm and depth d_2 = { 19, 25, 34, 53 } nm (red symbols). (c) Spectral peak positions ν_3^{max} and (e) peak height ratios C for the peak centered at 1115 cm^{-1} of PEO surface (black symbols) and PEO subsurface (red symbols) layers are plotted versus the corresponding peak heights φ_3^{max}. Arrows indicate decreasing PEO surface layer thickness t_1 (black) and increasing PEO subsurface layer depth d_2 (red). (d,f) Calculation results analogous to Figure 5.10c and e. Additionally, results for a large range of PEO surface layer thicknesses t_1 and PEO subsurface layer depths d_2 are shown. (e,f) Green areas indicate the data spaces that correspond to subsurface material. (g-l) Data analogous to panels a-f, for the peak centered at 1150 cm^{-1}. Spectral resolution of the experiments 17 cm^{-1}. The figure shows that (*1*) experimental and calculated nano-FTIR peak positions of subsurface PEO layers shift to lower frequencies (red-shift) compared to that of surface PEO layers of similar thickness. (*2*) The amount of the red-shift varies, depending on which peak is analyzed. (*3*) Most interesting and important, the peak height ratios $C = \varphi_4^{max}/\varphi_3^{max}$ observed for all PEO subsurface layers are smaller than those of PEO surface layers, corroborating their use as a rather robust criterium for distinguishing surface and subsurface layers.

6.4.3 Lorentz oscillators with different high-frequency permittivity

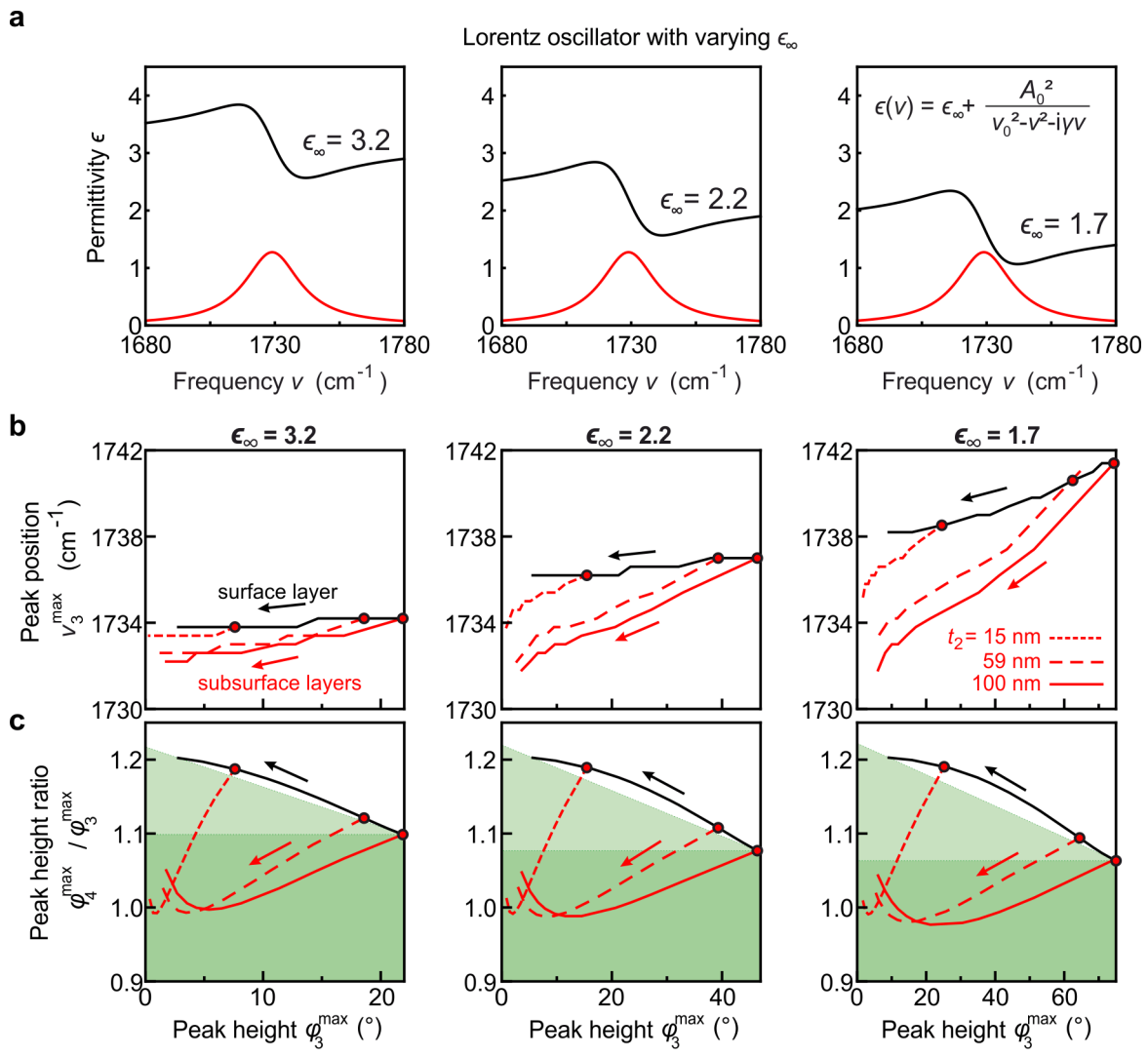

Figure 6.8: Correlation of nano-FTIR peak characteristics for a model Lorentz oscillator with varying high-frequency permittivities. (a) Real (black) and imaginary (red) parts of dielectric functions modelled by Lorentz oscillators with different high-frequency permittivities ϵ_∞ = { 3.2, 2.2, 1.7 } and fixed ν_0=1739 cm^{-1}, γ = 26 cm^{-1}, A_0 = 240 cm^{-1}. (b) Calculated spectral peak positions ν_3^{max} and (c) peak height ratios C of surface (black symbols) and subsurface (red symbols) layers are plotted versus the corresponding peak heights φ_3^{max}, for layers with the permittivities shown in panel a. Arrows indicate decreasing surface layer thickness t_1 (black) and increasing subsurface layer depth d_2 (red). Subsurface layer thicknesses are t_2 = 15 nm (dotted red line), t_2 = 59 nm (dashed red line) and t_2 = 100 nm (solid red line). Green areas in (c) indicate the data spaces that correspond to subsurface material. The figure shows for vibrational modes modelled by Lorentz oscillators with different high-frequency permittivities ϵ_∞ that: (*1*) nano-FTIR peak positions shift to lower frequencies (red-shift) when the thickness t_1 of a surface layer decreases or when the depth d_2 of a subsurface layer increases. (*2*) The red-shift is stronger for subsurface layers as compared to surface layers. (*3*) Most interesting and important, the peak height ratios $C = \varphi_4^{max}/\varphi_3^{max}$ observed for all modelled vibrations behave nearly the same as that of the C=O peak of PMMA (Figure 5.10), and thus can be considered as a rather robust criterium for distinguishing surface and subsurface layers.

6.4.4 Varying subsurface layer thickness

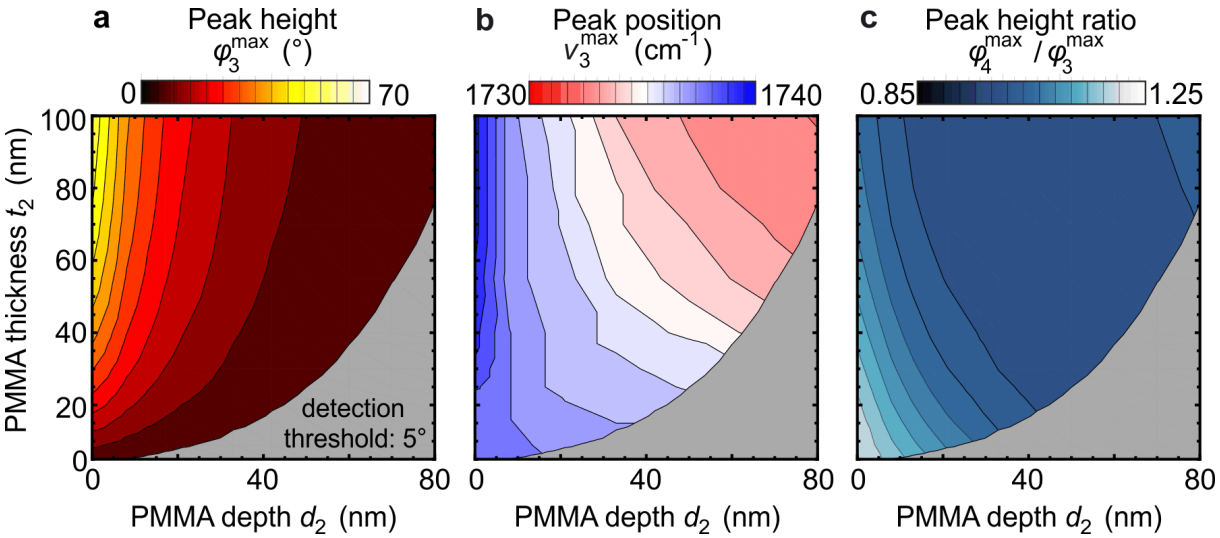

Figure 6.9: Nano-FTIR peak characteristics as function of layer depth and thickness. (a) Peak heights φ_3^{max}, (b) spectral peak positions ν_3^{max} and (c) peak height ratios C of PMMA subsurface layers are plotted as a function of PMMA depth d_2 and PMMA thickness t_2. Gray areas indicate peak heights $\varphi_3^{max} < 5°$, which we consider to be below the detection threshold. The figure shows that (*1*) for each PMMA layer thickness t_2 the nano-FTIR peak positions shift to lower frequencies (red-shift) when the depth d_2 of a subsurface layer increases. (*2*) The red-shift is stronger for PMMA subsurface layers with larger thickness t_2. (*3*) With decreasing thickness t_2 of the subsurface layer the peak heights reduce, which in turn reduces the depths d_2 at which a nano-FTIR peak can be practically detected. (*4*) Most interesting and important, the peak height ratios $C = \varphi_4^{max}/\varphi_3^{max}$ observed for all thicknesses t_2 decreases as the depth d_2 increases, corroborating the robustness as criterium for distinguishing surface and subsurface layers.

6.4.5 Varying capping layer permittivity

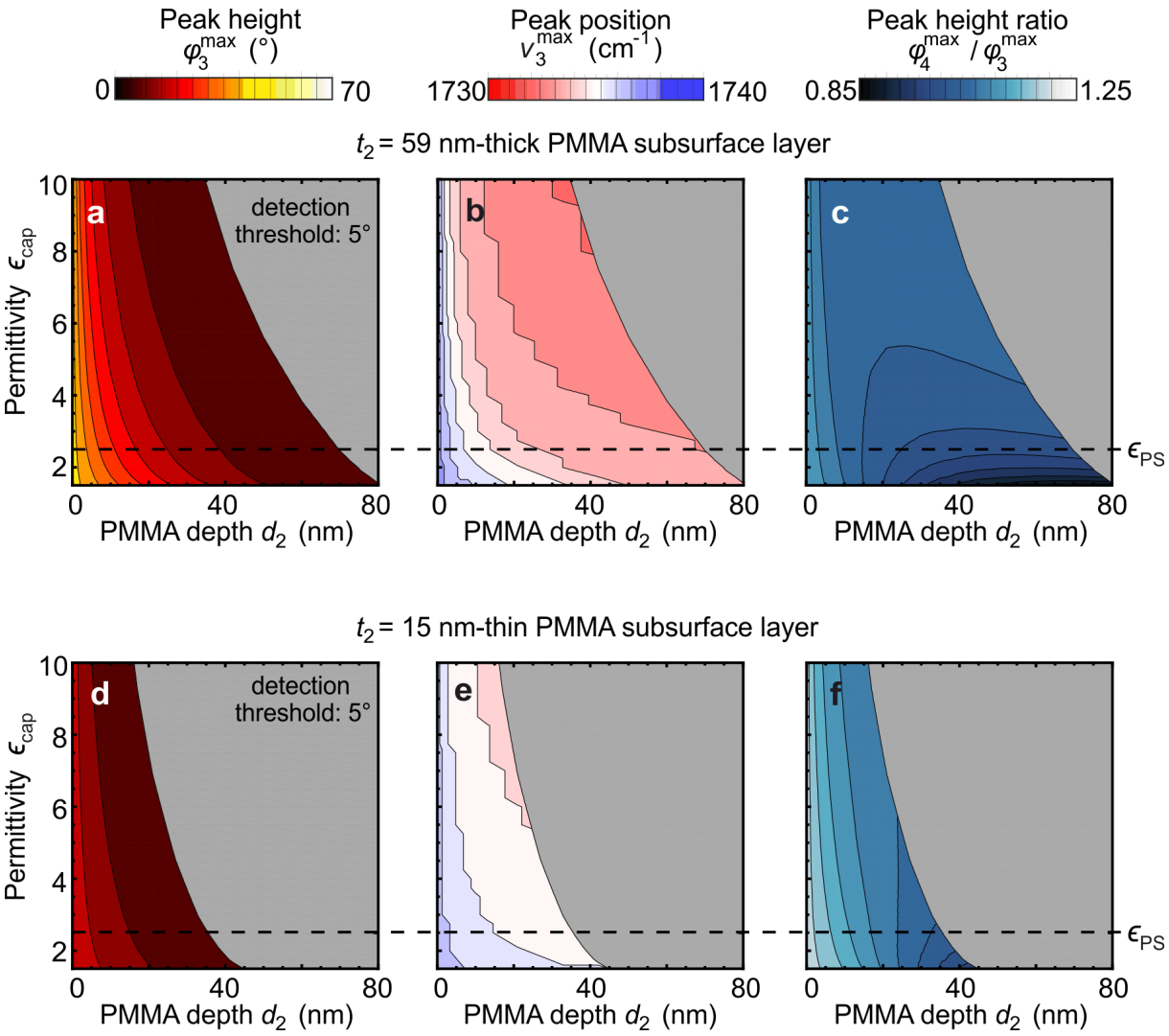

Figure 6.10: Nano-FTIR peak characteristics as function of capping layer permittivity and thickness. (a) Peak heights φ_4^{max}, (b) spectral peak positions ν_4^{max} and (c) peak height ratios C of a t_2 = 59 nm-thick PMMA subsurface layer are plotted as a function of PMMA depth d_2 and capping layer permittivity ϵ_{cap}. (c-f) Calculation results analogous to panels a-c, but for a t_2 = 15 nm-thin PMMA subsurface layer. (a-f) The horizontal dashed line indicates ϵ_{PS} which is used in the manuscript. Gray areas indicate peak heights φ_4^{max} < 5°, which we consider to be below the detection threshold. The figure shows that: (*1*) for each capping layer permittivity ϵ_{cap} and PMMA layer thickness t_2 the nano-FTIR peak positions shift to lower frequencies (red-shift) when the depth d_2 of a subsurface layer increases. (*2*) The red-shift is stronger when capping layer permittivity increases. (*3*) With increasing permittivity of the capping layer the peak heights reduce, which in turn reduces the depths d_2 at which a nano-FTIR peak can be practically detected. (*4*) Most interesting and important, the peak height ratios $C = \varphi_4^{max}/\varphi_3^{max}$ observed for all capping layer permittivities and both thicknesses t_2 decreases as the depth d_2 increases, corroborating the robustness as criterium for distinguishing surface and subsurface layers.

7 References

1. Zayats, A. V. & Richards (Prof.), D. *Nano-optics and Near-field Optical Microscopy*. (Artech House, 2009).

2. Keilmann, F. & Hillenbrand, R. Near-field microscopy by elastic light scattering from a tip. *Phil. Trans. R. Soc. Lond. A* **362**, 787–805 (2004).

3. Zenhausern, F., O'Boyle, M. P. & Wickramasinghe, H. K. Apertureless near-field optical microscope. *Applied Physics Letters* **65**, 1623–1625 (1994).

4. Markus B Raschke & Christoph Lienau. Apertureless near-field optical microscopy: Tip-sample coupling in elastic light scattering. *Applied Physics Letters* **83**, 5089–5091 (2003).

5. Taubner, T., Hillenbrand, R. & Keilmann, F. Performance of visible and mid-infrared scattering-type near-field optical microscopes. *Journal of Microscopy* **210**, 311–314 (2003).

6. Keilmann, F., Huber, A. J. & Hillenbrand, R. Nanoscale Conductivity Contrast by Scattering-Type Near-Field Optical Microscopy in the Visible, Infrared and THz Domains. *Journal of Infrared, Millimeter, and Terahertz Waves, Volume 30, Issue 12, pp.1255-1268* **30**, 1255–1268 (2009).

7. Raschke, M. B. *et al.* Apertureless Near-Field Vibrational Imaging of Block-Copolymer Nanostructures with Ultrahigh Spatial Resolution. *ChemPhysChem* **6**, 2197–2203 (2005).

8. Chen, H.-T., Kersting, R. & Cho, G. C. Terahertz imaging with nanometer resolution. *Appl. Phys. Lett.* **83**, 3009–3011 (2003).

9. Cho, G. C., Chen, H.-T., Kraatz, S., Karpowicz, N. & Kersting, R. Apertureless terahertz near-field microscopy. *Semicond. Sci. Technol.* **20**, S286–S292 (2005).

10. Novotny, L. & Hecht, B. *Principles of Nano-Optics*. (Cambridge, 2006).

11. Behr, N. & Raschke, M. B. Optical Antenna Properties of Scanning Probe Tips: Plasmonic Light Scattering, Tip-Sample Coupling, and Near-Field Enhancement. *J. Phys. Chem. C* **112**, 3766–3773 (2008).

12. Ocelic, N., Huber, A. & Hillenbrand, R. Pseudoheterodyne detection for background-free near-field spectroscopy. *Applied Physics Letters* **89**, 101124 (2006).

13. Ocelic, N. Quantitative near-field phonon-polariton spectroscopy. (Technische Universität München, 2007).

14. Griffiths, P. R. & de Haseth, J. A. *Fourier Transform Infrared Spectroscopy*. (John Wiley & Sons, Inc., 2007).

15. Huth, F. *et al.* Nano-FTIR Absorption Spectroscopy of Molecular Fingerprints at 20nm Spatial Resolution. *Nano Lett.* **12**, 3973–3978 (2012).

16. Amarie, S., Ganz, T. & Keilmann, F. Mid-infrared near-field spectroscopy. *Opt. Express, OE* **17**, 21794–21801 (2009).

17. Huth, F., Schnell, M., Wittborn, J., Ocelic, N. & Hillenbrand, R. Infrared-spectroscopic nanoimaging with a thermal source. *Nat Mater* **10**, 352–356 (2011).

18. Mastel, S., Govyadinov, A. A., de Oliveira, T. V. A. G., Amenabar, I. & Hillenbrand, R. Nanoscale-resolved chemical identification of thin organic films using infrared near-field spectroscopy and standard Fourier transform infrared references. *Appl. Phys. Lett.* **106**, 023113 (2015).

19. Taubner, T., Keilmann, F. & Hillenbrand, R. Nanoscale-resolved subsurface imaging by scattering-type near-field optical microscopy. *Optics Express* **13**, 8893 (2005).

20. Krutokhvostov, R. *et al.* Enhanced resolution in subsurface near-field optical microscopy. *Optics Express* **20**, 593 (2012).

21. Engelhardt, A. P., Hauer, B. & Taubner, T. Visibility of weak contrasts in subsurface scattering near-field microscopy. *Ultramicroscopy* **126**, 40–43 (2013).

22. Mester, L., Govyadinov, A. A., Chen, S., Goikoetxea, M. & Hillenbrand, R. Subsurface chemical nanoidentification by nano-FTIR spectroscopy. *Nature Communications* **11**, 3359 (2020).

23. Govyadinov, A. A. *et al.* Recovery of Permittivity and Depth from Near-Field Data as a Step toward Infrared Nanotomography. *ACS Nano* **8**, 6911–6921 (2014).

24. Lewin, M. *et al.* Imaging of phase change materials below a capping layer using correlative infrared near-field microscopy and electron microscopy. *Appl. Phys. Lett.* **107**, 151902 (2015).

25. Moon, K. *et al.* Subsurface Nanoimaging by Broadband Terahertz Pulse Near-Field Microscopy. *Nano Lett.* **15**, 549–552 (2015).

26. Gozar, A., Litombe, N. E., Hoffman, J. E. & Božović, I. Optical Nanoscopy of High Tc Cuprate Nanoconstriction Devices Patterned by Helium Ion Beams. *Nano Lett.* **17**, 1582–1586 (2017).

27. Mooshammer, F. *et al.* Nanoscale Near-Field Tomography of Surface States on (Bi0.5Sb0.5)2Te3. *Nano Lett.* **18**, 7515–7523 (2018).

28. Jung, L. *et al.* Exploring the detection limits of infrared near-field microscopy regarding small buried structures and pushing them by exploiting superlens-related effects. *Opt. Express, OE* **24**, 4431–4441 (2016).

29. Huber, A. J., Keilmann, F., Wittborn, J., Aizpurua, J. & Hillenbrand, R. Terahertz Near-Field Nanoscopy of Mobile Carriers in Single Semiconductor Nanodevices. *Nano Lett.* **8**, 3766–3770 (2008).

30. Autore, M., Mester, L., Goikoetxea, M. & Hillenbrand, R. Substrate Matters: Surface-Polariton Enhanced Infrared Nanospectroscopy of Molecular Vibrations. *Nano Lett.* **19**, 8066–8073 (2019).

31. Mertz, J. *Introduction to optical microscopy*. (Roberts and Company Publishers, 2016).

32. Born, M. & Wolf, E. *Principles of Optics*. (Cambridge University Press, 1999).

33. Electromagnetic spectrum. *Encyclopaedia Britannica* https://www.britannica.com/science/electromagnetic-spectrum (2019).

34. Schrader, B. *Infrared and Raman spectroscopy*. (VCH Verlagsgesellschaft GmbH, 1995).

35. Mark Fox. *Optical Properties of Solids*. (Oxford University Press, 2010).

36. Abbe, E. Beiträge zur Theorie des Mikroskops und der mikroskopischen Wahrnehmung. *Archiv f. mikrosk. Anatomie* **9**, 413–418 (1873).

37. Guozhong, C. *Nanostructures and Nanomaterials: Synthesis, Properties and Applications*. (World Scientific Publishing, 2004).

38. Mayer, E., Hug, H. J. & Bennewitz, R. *Scanning Probe Microscopy: The Lab on a Tip*. vol. 1+2 (Wiley-VCH, 2012).

39. Ocelic, N. & Hillenbrand, R. Subwavelength-scale tailoring of surface phonon polaritons by focused ion-beam implantation. *Nat Mater* **3**, 606–609 (2004).

40. Huth, F. Nano-FTIR - Nanoscale Infrared Near-field Spectroscopy. (Universidad del Pais Vasco, 2015).

41. Lu, F., Jin, M. & Belkin, M. A. Tip-enhanced infrared nanospectroscopy via molecular expansion force detection. *Nature Photonics* **8**, 307–312 (2014).

42. Dazzi, A. *et al.* AFM–IR: Combining Atomic Force Microscopy and Infrared Spectroscopy for Nanoscale Chemical Characterization. *Appl Spectrosc* **66**, 1365–1384 (2012).

43. Rajapaksa, I., Uenal, K. & Wickramasinghe, H. K. Image force microscopy of molecular resonance: A microscope principle. *Applied Physics Letters* **97**, 073121 (2010).

44. Nowak, D. *et al.* Nanoscale chemical imaging by photoinduced force microscopy. *Sci Adv* **2**, (2016).

45. Greffet, J.-J. & Carminati, R. Image formation in near-field optics. *Progress in Surface Science* **56**, 133–237 (1997).

46. Michelson, A. A. XXXVIII. On the application of interference-methods to spectroscopic measurements.—I. *The London, Edinburgh, and Dublin Philosophical Magazine and Journal of Science* **31**, 338–346 (1891).

47. Keilmann, F. & Hillenbrand, R. *Nano-Optics and Near-Field Optical Microscopy*. (Artech House, 2008).

48. A Cvitkovic, N Ocelic & R Hillenbrand. Analytical model for quantitative prediction of material contrasts in scattering-type near-field optical microscopy. *Optics Express* **15**, 8550–8565 (2007).

49. Taubner, T., Hillenbrand, R. & Keilmann, F. Nanoscale polymer recognition by spectral signature in scattering infrared near-field microscopy. *Applied Physics Letters* **85**, 5064–5066 (2004).

50. Hillenbrand, R., Taubner, T. & Keilmann, F. Phonon-enhanced light–matter interaction at the nanometre scale. *Nature* **418**, 159–162 (2002).

51. Aizpurua, J., Taubner, T., Javier Garcia de Abajo, F., Brehm, M. & Hillenbrand, R. Substrate-enhanced infrared near-field spectroscopy. *Optics Express* **16**, 1529–1545 (2008).

52. Govyadinov, A. A., Amenabar, I., Huth, F., Carney, P. S. & Hillenbrand, R. Quantitative Measurement of Local Infrared Absorption and Dielectric Function with Tip-Enhanced Near-Field Microscopy. *J. Phys. Chem. Lett.* **4**, 1526–1531 (2013).

53. Lewin, M. *et al.* Sb2Te3 Growth Study Reveals That Formation of Nanoscale Charge Carrier Domains Is an Intrinsic Feature Relevant for Electronic Applications. *ACS Appl. Nano Mater.* **1**, 6834–6842 (2018).

54. Hauer, B., Engelhardt, A. P. & Taubner, T. Quasi-analytical model for scattering infrared near-field microscopy on layered systems. *Optics Express* **20**, 13173 (2012).

55. Caldwell, J. D. *et al.* Low-loss, infrared and terahertz nanophotonics using surface phonon polaritons. *Nanophotonics* **4**, 44–68 (2015).

56. Huber, A. j., Ocelic, N. & Hillenbrand, R. Local excitation and interference of surface phonon polaritons studied by near-field infrared microscopy. *Journal of Microscopy* **229**, 389–395 (2008).

57. Jackson, J. D. *Classical Electrodynamics*. (John Wiley & Sons, Inc., 2001).

58. McLeod, A. S. *et al.* Model for quantitative tip-enhanced spectroscopy and the extraction of nanoscale-resolved optical constants. *Phys. Rev. B* **90**, 085136 (2014).

59. Jiang, B.-Y., Zhang, L. M., Castro Neto, A. H., Basov, D. N. & Fogler, M. M. Generalized spectral method for near-field optical microscopy. *Journal of Applied Physics* **119**, 054305 (2016).

60. Brehm, M. Infrarot-Mikrospektroskopie mit einem Nahfeldmikroskop. (Technische Universität München, 2006).

61. Wang, B. & Woo, C. H. Atomic force microscopy-induced electric field in ferroelectric thin films. *Journal of Applied Physics* **94**, 4053–4059 (2003).

62. Hauer, B. Nano-optical mapping of permittivity contrasts and electronic properties at the surface and beneath. (RWTH Aachen University, 2015).

63. Chen, S. *et al.* On the anomalous optical conductivity dispersion of electrically conducting polymers: ultra-wide spectral range ellipsometry combined with a Drude–Lorentz model. *Journal of Materials Chemistry C* **7**, 4350–4362 (2019).

64. Liu, Y. *et al.* Negative group velocity of surface plasmons on thin metallic films. in *Plasmonics: Metallic Nanostructures and their Optical Properties IV* vol. 6323 63231M (International Society for Optics and Photonics, 2006).

65. Chen, X. *et al.* Modern Scattering-Type Scanning Near-Field Optical Microscopy for Advanced Material Research. *Advanced Materials* **31**, 1804774 (2019).

66. Fei, Z. *et al.* Infrared Nanoscopy of Dirac Plasmons at the Graphene–SiO2 Interface. *Nano Lett.* **11**, 4701–4705 (2011).

67. Amenabar Altuna, I. Infrared nanospectroscopy and hyperspectral nanoimaging of organic matter. (Universidad del Pais Vasco, 2017).

68. Li, M., Cushing, S. K. & Wu, N. Plasmon-Enhanced Optical Sensors: A Review. *Analyst* **140**, 386–406 (2015).

69. Zhang, L. M. *et al.* Near-field spectroscopy of silicon dioxide thin films. *Phys. Rev. B* **85**, 075419 (2012).

70. Luo, W. *et al.* High sensitivity variable-temperature infrared nanoscopy of conducting oxide interfaces. *Nature Communications* **10**, 2774 (2019).

71. Maissen, C., Chen, S., Nikulina, E., Govyadinov, A. & Hillenbrand, R. Probes for Ultrasensitive THz Nanoscopy. *ACS Photonics* **6**, 1279–1288 (2019).

72. Knoll, B. & Keilmann, F. Enhanced dielectric contrast in scattering-type scanning near-field optical microscopy. *Optics Communications* **182**, 321–328 (2000).

73. Amarie, S. *et al.* Nano-FTIR chemical mapping of minerals in biological materials. *Beilstein J Nanotechnol* **3**, 312–323 (2012).

74. Binnig, G., Quate, C. F. & Gerber, Ch. Atomic Force Microscope. *Phys. Rev. Lett.* **56**, 930–933 (1986).

75. Eaton, P. & West, P. *Atomic Force Microscopy*. (Oxford University Press, 2010).

76. Berlin, A. A., Kablov, V. F., Pimerzin, A. A. & Zlotsky, S. S. *Key Elements in POLYMERS for ENGINEERS and CHEMISTS: From Data to Applications*. (Apple Academic Press, 2014).

77. Bechtel, H. A., Muller, E. A., Olmon, R. L., Martin, M. C. & Raschke, M. B. Ultrabroadband infrared nanospectroscopic imaging. *PNAS* **111**, 7191–7196 (2014).

78. Westermeier, C. *et al.* Sub-micron phase coexistence in small-molecule organic thin films revealed by infrared nano-imaging. *Nat Commun* **5**, 1–6 (2014).

79. Qazilbash, M. M. *et al.* Mott Transition in VO2 Revealed by Infrared Spectroscopy and Nano-Imaging. *Science* **318**, 1750–1753 (2007).

80. Stiegler, J. M. *et al.* Nanoscale Free-Carrier Profiling of Individual Semiconductor Nanowires by Infrared Near-Field Nanoscopy. *Nano Lett.* **10**, 1387–1392 (2010).

81. Lucas, I. T. *et al.* IR Near-Field Spectroscopy and Imaging of Single LixFePO4 Microcrystals. *Nano Lett.* **15**, 1–7 (2015).

82. Ritchie, E. T. *et al.* Mapping Free-Carriers in Multijunction Silicon Nanowires Using Infrared Near-Field Optical Microscopy. *Nano Lett.* **17**, 6591–6597 (2017).

83. Sterl, F. *et al.* Nanoscale Hydrogenography on Single Magnesium Nanoparticles. *Nano Lett.* **18**, 4293–4302 (2018).

84. Amenabar, I. *et al.* Structural analysis and mapping of individual protein complexes by infrared nanospectroscopy. *Nat Commun* **4**, 1–9 (2013).

85. Xu, X. G., Rang, M., Craig, I. M. & Raschke, M. B. Pushing the Sample-Size Limit of Infrared Vibrational Nanospectroscopy: From Monolayer toward Single Molecule Sensitivity. *J. Phys. Chem. Lett.* **3**, 1836–1841 (2012).

86. Berweger, S. *et al.* Nano-Chemical Infrared Imaging of Membrane Proteins in Lipid Bilayers. *J. Am. Chem. Soc.* **135**, 18292–18295 (2013).

87. Cvitkovic, A., Ocelic, N., Aizpurua, J., Guckenberger, R. & Hillenbrand, R. Infrared Imaging of Single Nanoparticles via Strong Field Enhancement in a Scanning Nanogap. *Phys. Rev. Lett.* (2006) doi:10.1103/PhysRevLett.97.060801.

88. Brehm, M., Taubner, T., Hillenbrand, R. & Keilmann, F. Infrared spectroscopic mapping of single nanoparticles and viruses at nanoscale resolution. *Nano Letters* **6**, 1307–1310 (2006).

89. Cvitkovic, A., Ocelic, N. & Hillenbrand, R. Material-Specific Infrared Recognition of Single Sub-10 nm Particles by Substrate-Enhanced Scattering-Type Near-Field Microscopy. *Nano Lett.* **7**, 3177–3181 (2007).

90. Steidtner, J. & Pettinger, B. Tip-Enhanced Raman Spectroscopy and Microscopy on Single Dye Molecules with 15 nm Resolution. *Phys. Rev. Lett.* **100**, 236101 (2008).

91. Hoffmann, J. M., Hauer, B. & Taubner, T. Antenna-enhanced infrared near-field nanospectroscopy of a polymer. *Applied Physics Letters* **101**, 193105 (2012).

92. Muller, E. A. *et al.* Nanoimaging and Control of Molecular Vibrations through Electromagnetically Induced Scattering Reaching the Strong Coupling Regime. *ACS Photonics* **5**, 3594–3600 (2018).

93. O'Callahan, B. T., Hentschel, M., Raschke, M. B., El-Khoury, P. Z. & Lea, A. S. Ultrasensitive Tip- and Antenna-Enhanced Infrared Nanoscopy of Protein Complexes. *J. Phys. Chem. C* **123**, 17505–17509 (2019).

94. Hu, H. *et al.* Far-field nanoscale infrared spectroscopy of vibrational fingerprints of molecules with graphene plasmons. *Nature Communications* **7**, 12334 (2016).

95. Bass, M. *et al. Handbook of Optics: Optical Properties of Materials, Nonlinear Optics, Quantum Optics*. vol. 3rd (McGraw-Hill Education, 2009).

96. Amarie, S. & Keilmann, F. Broadband-infrared assessment of phonon resonance in scattering-type near-field microscopy. *Phys. Rev. B* **83**, 045404 (2011).

97. Li, P. *et al.* Reversible optical switching of highly confined phonon–polaritons with an ultrathin phase-change material. *Nature Materials* **15**, 870–875 (2016).

98. Kuzmenko, A. B. Kramers–Kronig constrained variational analysis of optical spectra. *Review of Scientific Instruments* **76**, 083108 (2005).

99. Neubrech, F. *et al.* Resonant Plasmonic and Vibrational Coupling in a Tailored Nanoantenna for Infrared Detection. *Phys. Rev. Lett.* **101**, 157403 (2008).

100. Neubrech, F., Huck, C., Weber, K., Pucci, A. & Giessen, H. Surface-Enhanced Infrared Spectroscopy Using Resonant Nanoantennas. *Chem. Rev.* **117**, 5110–5145 (2017).

101. Autore, M. *et al.* Boron nitride nanoresonators for phonon-enhanced molecular vibrational spectroscopy at the strong coupling limit. *Light: Science & Applications* **7**, 17172–17172 (2018).

102. Taubner, T., Keilmann, F. & Hillenbrand, R. Nanomechanical Resonance Tuning and Phase Effects in Optical Near-Field Interaction. *Nano Lett.* **4**, 1669–1672 (2004).

103. Wang, H., Wang, L., Jakob, D. S. & Xu, X. G. Tomographic and multimodal scattering-type scanning near-field optical microscopy with peak force tapping mode. *Nature Communications* **9**, 2005 (2018).

104. Huber, A., Ocelic, N., Kazantsev, D. & Hillenbrand, R. Near-field imaging of mid-infrared surface phonon polariton propagation. *Appl. Phys. Lett.* **87**, 081103 (2005).

105. Sumikura, H. *et al.* Highly Confined and Switchable Mid-Infrared Surface Phonon Polariton Resonances of Planar Circular Cavities with a Phase Change Material. *Nano Lett.* **19**, 2549–2554 (2019).

106. Dubrovkin, A. M., Qiang, B., Krishnamoorthy, H. N. S., Zheludev, N. I. & Wang, Q. J. Ultra-confined surface phonon polaritons in molecular layers of van der Waals dielectrics. *Nature Communications* **9**, 1762 (2018).

107. Law, S., Yu, L., Rosenberg, A. & Wasserman, D. All-Semiconductor Plasmonic Nanoantennas for Infrared Sensing. *Nano Lett.* **13**, 4569–4574 (2013).

108. Wagner, M. *et al.* Ultrafast Dynamics of Surface Plasmons in InAs by Time-Resolved Infrared Nanospectroscopy. *Nano Lett.* **14**, 4529–4534 (2014).

109. Barho, F. B. *et al.* Highly doped semiconductor plasmonic nanoantenna arrays for polarization selective broadband surface-enhanced infrared absorption spectroscopy of vanillin. *Nanophotonics* **7**, 507–516 (2017).

110. Zhou, Y. *et al.* Tunable Low Loss 1D Surface Plasmons in InAs Nanowires. *Advanced Materials* **30**, 1802551 (2018).

111. Dai, S. *et al.* Tunable Phonon Polaritons in Atomically Thin van der Waals Crystals of Boron Nitride. *Science* **343**, 1125–1129 (2014).

112. Li, P. *et al.* Optical Nanoimaging of Hyperbolic Surface Polaritons at the Edges of van der Waals Materials. *Nano Lett.* **17**, 228–235 (2017).

113. Chen, J. *et al.* Optical nano-imaging of gate-tunable graphene plasmons. *Nature* **487**, 77–81 (2012).

114. Fei, Z. *et al.* Gate-tuning of graphene plasmons revealed by infrared nano-imaging. *Nature* **487**, 82–85 (2012).

115. Huber, A. J., Deutsch, B., Novotny, L. & Hillenbrand, R. Focusing of surface phonon polaritons. *Appl. Phys. Lett.* **92**, 203104 (2008).

116. Alonso-González, P. *et al.* Controlling graphene plasmons with resonant metal antennas and spatial conductivity patterns. *Science* **344**, 1369–1373 (2014).

117. Dai, S. *et al.* Subdiffractional focusing and guiding of polaritonic rays in a natural hyperbolic material. *Nature Communications* **6**, 6963 (2015).

118. Li, P. *et al.* Hyperbolic phonon-polaritons in boron nitride for near-field optical imaging and focusing. *Nature Communications* **6**, 7507 (2015).

119. Kästner, B. *et al.* Infrared Nanospectroscopy of Phospholipid and Surfactin Monolayer Domains. *ACS Omega* **3**, 4141–4147 (2018).

120. Caldwell, J. D. *et al.* Low-Loss, Extreme Subdiffraction Photon Confinement via Silicon Carbide Localized Surface Phonon Polariton Resonators. *Nano Lett.* **13**, 3690–3697 (2013).

121. Wang, T. *et al.* Phonon-Polaritonic Bowtie Nanoantennas: Controlling Infrared Thermal Radiation at the Nanoscale. *ACS Photonics* **4**, 1753–1760 (2017).

122. Alfaro-Mozaz, F. J. *et al.* Nanoimaging of resonating hyperbolic polaritons in linear boron nitride antennas. *Nature Communications* **8**, 15624 (2017).

123. Ho, K. *et al.* Nanoscale Subsurface Morphologies in Block Copolymer Thin Films Revealed by Combined Near-Field Infrared Microscopy and Mechanical Mapping. *ACS Appl. Polym. Mater.* **1**, 933–938 (2019).

124. Pollard, B., Muller, E. A., Hinrichs, K. & Raschke, M. B. Vibrational nano-spectroscopic imaging correlating structure with intermolecular coupling and dynamics. *Nature Communications* **5**, 3587 (2014).

125. Pacansky, J., England, C. & Waltman, R. J. Complex refractive indexes for polymers over the infrared spectral region: Specular reflection IR spectra of polymers. *Journal of Polymer Science Part B: Polymer Physics* **25**, 901–933 (1987).

126. Arnulf Röseler. *Infrared Spectroscopic Ellipsometry*. (Akademie-Verlag, 1990).

127. Orlov, A. S., Kiselev, S. A., Kiseleva, E. A., Budeeva, A. V. & Mashukov, V. I. Determination of styrene-butadiene rubber composition by attenuated total internal reflection infrared spectroscopy. *JApSp* **80**, 47–53 (2013).

128. Schmidt, U., Hild, S., Ibach, W. & Hollricher, O. Characterization of Thin Polymer Films on the Nanometer Scale with Confocal Raman AFM. *Macromolecular Symposia* **230**, 133–143 (2005).

129. James, J., Thomas, G. V., P, P. K., Kalarikkal, N. & Thomas, S. Thermoplastic–elastomer composition based on an interpenetrating polymeric network of styrene butadiene rubber–poly(methyl methacrylate) as an efficient vibrational damper. *New J. Chem.* **42**, 1939–1951 (2018).

130. Ennis, D., Betz, H. & Ade, H. Direct spincasting of polystyrene thin films onto poly(methyl methacrylate). *J. Polym. Sci. B Polym. Phys.* **44**, 3234–3244 (2006).

131. Olmos, D., Martín, E. V. & González-Benito, J. New molecular-scale information on polystyrene dynamics in PS and PS–BaTiO3 composites from FTIR spectroscopy. *Phys. Chem. Chem. Phys.* **16**, 24339–24349 (2014).

132. Amma, S., Luo, J., Pantano, C. G. & Kim, S. H. Specular reflectance (SR) and attenuated total reflectance (ATR) infrared (IR) spectroscopy of transparent flat glass surfaces: A case study for soda lime float glass. *Journal of Non-Crystalline Solids* **428**, 189–196 (2015).

133. Nolting. *Grundkurs theoretische Physik. Bd.3: Elektrodynamik*. vol. 3.

8 Own publications

This thesis is based on the following publications:

- Autore, M., Mester, L., Goikoetxea, M. & Hillenbrand, R. Substrate Matters: Surface-Polariton Enhanced Infrared Nanospectroscopy of Molecular Vibrations. *Nano Lett.* **19**, 8066–8073 (2019).

- Mester, L., Govyadinov, A. A., Chen, S., Goikoetxea, M. & Hillenbrand, R. Subsurface chemical nanoidentification by nano-FTIR spectroscopy. *Nature Comm.* **11**, 3359 (2020).

9 Acknowledgements

I want to express my gratitude to my supervisor Prof. Rainer Hillenbrand, group leader of the nano-optics group at CIC nanoGUNE, for giving me the opportunity to join his group, always being open for discussions and for his patience.

I thank Prof. Txema Pitarke, director of CIC nanoGUNE, for giving me the opportunity to perform outstanding nanoscience research in the Basque Country at CIC nanoGUNE.

I am thankful to all present and past members of the nano-optics group at CIC nanoGUNE, for a great atmosphere, interesting discussions, and mutual support. Special thanks to Monika Goikoetxea, for always offering her help and support particularly related to the chemistry of polymers. Many thanks also to Carlos Crespo (for taking good care of our laboratories and helping out all group members wherever possible, starting already on day one with helping through the Spanish bureaucracy), to Stefan Mastel and Iban Amenabar (for always being ready to discuss details on the instrumentation of our laboratories), to Divya Virmani (for the 16 o'clock coffee breaks) and to Carlos Maciel and Irene Dolado (particularly for their help in translating, but also for the scientific collaboration).

I also want to thank all collaborators and all members of the SPM2.0 network, for many scientific discussions and contributions to many interesting projects.

I thank all employees of neaspec GmbH for their continuous technical support during the time of my PhD thesis.

I further thank everyone involved in our interdisciplinary Tuesday, Thursday or Friday PhD-reunions.

Special thanks go to my family and friends for their continuous support and a good time throughout the whole thesis.

This work has received funding from the European Union's Horizon 2020 research and innovation program under the Marie Sklodowska-Curie grant agreement No. 721874 (SPM2.0). I further acknowledge the financial support of my co-authors from the Spanish Ministry of Science, Innovation and Universities (national project RTI2018-094830-B-100 and the project MDM-2016-0618 of the Marie de Maeztu Units of Excellence Program) and the Basque Government (grant No. IT1164-19).

10 Documentation